Never Breaking Quasi-Periodic Solutions of Weakly Nonlinear Gas Dynamics

by

Michael G. Shefter

M.S. in Applied Mathematics and Mechanics,
Moscow State University, Moscow (1992)

Submitted to the Department of Mathematics
in partial fulfillment of the requirements for the degree of

Doctor of Philosophy

at the

MASSACHUSETTS INSTITUTE OF TECHNOLOGY

September 1997

Author ....
Department of Mathematics
June 20, 1997

Certified by ....
Rodolfo R. Rosales
Professor of Applied Mathematics
Thesis Supervisor

Accepted by ....
Hung Cheng
Chairman, Applied Mathematics Committee

Accepted by ....
Richard Melrose
Chairman, Departmental Committee on Graduate Students

Never Breaking Quasi-Periodic Solutions of Weakly Nonlinear Gas Dynamics

by

Michael G. Shefter

Submitted to the Department of Mathematics
on June 20, 1997, in partial fulfillment of the
requirements for the degree of
Doctor of Philosophy

Abstract

We study new never–breaking weakly nonlinear solutions for the 1–D equations of Gas Dynamics in a bounded domain with reflecting boundary conditions. Then the Euler equations can be reduced to a Burgers equation with periodic boundary conditions and an added linear integral dispersive term. The balance of nonlinearity and dispersion leads to the formation of time periodic or quasiperiodic solutions.

In addition to (previously known) periodic traveling waves, we found a new family of solutions by direct numerical simulation. These are attracting, never–breaking (they produce no shocks) and quasiperiodic in time with two periods. Furthermore, we also discovered a large set of neutrally stable quasiperiodic solutions with a similar doubly periodic in time structure. In the phase space of Fourier coefficients these quasiperiodic solutions fill a 3-D volume bounded by a 2-D "surface" formed by the attractors. At the "axis" of this volume are the periodic traveling waves.

We developed a semi–conservative numerical algorithm with shock tracking (as needed for the long–time numerical integration of the model equation this work required). The scheme features very good resolution of the singularities arising in the solutions (shocks and corners) and extremely small production of numerical noise.

We found that the traveling waves are linearly neutrally stable to doubly periodic in time perturbations. The linear stability analysis in this case can be formulated as an eigenvalue problem. The spectrum can then be found by a combination of WKB and numerical techniques. It is natural to expect that the linear neutrally stable modes will give rise to nearby solutions with an extra mode of oscillation. We compared the Linear theory predictions with the neutrally stable solutions obtained in the numerical experiments and found that only smallest frequency in the spectrum appears to give rise to physically realizable solutions.

Thesis Supervisor: Rodolfo R. Rosales
Title: Professor of Applied Mathematics

Acknowledgments

I am very grateful to my scientific advisor, Professor Ruben Rosales, for his generous support and guidance during my years at MIT. His scientific views exerted a great influence on me and his expertise was a valuable resource throughout my research.

I am thankful to Professors David Benney and Michael Brenner, who accepted to be part of my thesis committee and to the faculty of the Applied Mathematics Department at MIT for the excellent quality of courses and seminars. I have learned a good deal from them.

I would like to acknowledge financial support from MIT Department of Mathematics. The research in this thesis was partially sponsored by the National Science Foundation (grant NSF DMS-9311438) and NASA (grant NASA NAG1-1519).

These five years at MIT would not have been half as enjoyable without my fellow graduate students and postdocs Alec, Carlos, Dan, Dave, Ernest, Giuseppe, Mats, Miklos, Radica, Shinya, Siqian, Tom, Tony, just to mention a few. Some of them have become good friends of mine. A special note of appreciation goes to Dimitriy and Guillermo, with whom I shared my learning experience and ups and downs of studying at MIT. Their friendship is extremely valuable to me.

My parents have always stood beside me during all these years. I thank them and Anna, Julia, Olga and Vadim for their patience and understanding. To all them I owe much more than I can express in words.

Contents

List of Figures

Chapter 1

Introduction.

The problem of existence of non–breaking (no shocks formed) for all times solutions for the Euler equations has long been an open question. New, analytical and numerical, results obtained recently ([5], [26]) for the full Gas Dynamics equations, show that the set of non–breaking solutions is large and highly nontrivial. For example, Celentano [5] showed that there is a large class of periodic standing waves bifurcating from the equilibrium solutions. Vaynblat [26] showed that there are many other never breaking solutions for the full Gas Dynamics equations, with much more complicated structure. It is the purpose of this thesis to show numerical and analytical evidence for the existence of a large class of new never breaking solutions (valid in the weakly nonlinear regime) that appear to be quasiperiodic in time. Furthermore, a special subset of this class seems to be globally attracting, namely: the long time evolution asymptotes to members of this class. We study the structure of these solutions, both individually and as a class.

The plan of this thesis is as follows. In Chapter 2 we make a brief survey of the main results relevant to the weakly nonlinear regime and derive the model equation. In Section 2.1 we consider the 1–D Euler equations for a gas inside a rigid closed pipe, in the nonlinear acoustics (weakly nonlinear) regime. We show that the problem can be reduced to the single leading order asymptotic integro–differential equation

$$\frac{\partial}{\partial t}u(x,t) + \frac{\partial}{\partial x}\left(\frac{1}{2}u^2(x,t)\right) + \int_0^{2\pi} K(x-y)\; u(y,t)\, dy = 0\,, \tag{1.1}$$

where $u(x,t)$ is the acoustic wave amplitude and the kernel $K(x)$ in the integral convolution term is the derivative of the entropy. It turns out that $K(x)$ must be odd and 2π–periodic. Furthermore, periodic boundary conditions in x for $u(x,t)$ apply. Notice that K is independent of time: this is because in the weakly nonlinear limit entropy is preserved up to third order[1] — thus its time dependence can safely be neglected in the framework of nonlinear acoustics.

This equation has been studied before by Gabov in [9]; Majda, Rosales and Schonbeck in [19] and Pego in [20]. It presents two counteracting mechanisms, namely: nonlinear steepening and linear dispersion (the latter by the integral term — as shown in Appendix B). The balance between them can lead to the formation of stable never–breaking structures. In particular, the **traveling waves** for this equation are known[2] and form a one–parameter family of analytic solutions (see Section 2.2). In addition to being periodic in space they are, obviously, also periodic in time. The traveling waves exist only in a finite range of amplitudes (or, equivalently, energies). If the wave amplitude is chosen as a parameter, then the solutions are bounded by the trivial ($u \equiv 0$) solution from below and by a maximum amplitude wave from above. This maximum amplitude solution is in fact not analytic, for the wave profile has a corner in it. This phenomenon of corner formation at maximum amplitude is very similar to the one observed for Stokes waves (see [27]). The boundedness of the solution set in energy space is related to the **weakness** of the dispersion, with a strength that decays rapidly with the wavenumber[3]. Dispersion, therefore, cannot compensate for the nonlinear steepening associated with large amplitude waves.

Motivated by the existence of these traveling wave solutions and the results in the recent work in [5] and [26], the aim of this thesis is to explore the general behavior of the solutions to equation (1.1). In particular, some questions of interest are:

1. Are there other never–breaking solutions to the equation, in addition to the traveling waves?
2. If so, what is the structure of these solutions? Are they stable? What is their basin of attraction?
3. What is the long time behavior of the solutions of (1.1) for general initial data?

The last question here is related to the two prior ones because it seems natural to expect that the long time behavior of the solutions (after any shocks form and decay) should be given by solutions in this never–breaking class. The argument here being as follows: we will show that the energy of the solutions to equation (1.1) is monotone non-increasing — see Appendix C. Thus, as $t \to \infty$, the energy must approach a limit. If this limit is nonzero, then it must correspond to nontrivial behaviour that keeps the energy constant, i.e. a never–breaking solution.

A purely analytical study of these and related questions is very difficult, if not impossible. Thus we resorted to numerical simulation, aiming to find never–breaking solutions (and study their

---

[1] Even if shocks occur.

[2] For simple kernels K.

[3] For the kernel in (1.2), for example, only one component in the Fourier expansion giving the dispersion relation is nontrivial: see equation (B.2) in Appendix B.

properties) as a result of long–time integration. Obviously, in such a study it is crucial to develop a numerical scheme with as little numerical dissipation as possible, else the numerical dissipation will drive the energy of the solution to zero and any non–trivial behaviour will be missed. Furthermore, the long time evolution calculations that we performed reveal rather subtle properties, which can be completely destroyed by accumulated numerical errors.

Equation (1.1) is hyperbolic and can produce both strong (shocks) and weak (corners) singularities, even when the initial conditions are smooth. Poor resolution of these singularities is the usual largest source of error and numerical dissipation. An algorithm able to deal with such difficulties is required. In Chapter 3 we describe a numerical scheme for the time integration of (1.1), which allows us to resolve shocks and corner singularities with fairly high accuracy — and thus yields results with very little numerical dissipation. The schemes best suited to deal with shocks and corners are the upstream conservative shock capturing methods. These schemes, however, are designed to deal with local equations only — thus, the nonlocal integral dispersive term in (1.1) would be very difficult to implement with them. To resolve this problem, while preserving the nice properties of upstream schemes near singularities at the same time, we resorted to a **time splitting** idea. We used an upstream method for the local (inviscid Burgers) part of the equation (specifically, a second order Godunov type scheme). For the convolution term we used an ordinary second order Runge-Kutta scheme in time, calculating the integral with a trapezoidal rule.[4]

Upstream schemes are not only effective at "shock capturing", but are remarkably free of (spurious) high-frequency oscillations near them. However, shocks still remain a significant source of numerical errors (excessive for our purposes). These follow because the "numerical" shocks are "spread" over several grid points, forming staircase–like structures. Such spreading is equivalent to introducing extra numerical dissipation into the system, which is one thing we cannot afford in our problem. Thus, to improve the resolution near shocks and avoid this problem, we used a shock tracking technique (see Section 3.2.6) on a moving grid. We also selected a UNO type scheme for the reconstruction step, because it had the best properties in terms of corner resolution.

In Chapter 4 we present a numerical study of equation (1.1), for the case of the single mode integral operator kernel

$$K(x) = \sin(x)\,. \tag{1.2}$$

First, in Section 4.1, we introduce a form of the method of Poincaré sections — of frequent use in studies of dynamical systems — adequate for our purposes. For the system described by (1.1) and (1.2), the Fourier coefficients of the solution turn out to be a useful and natural coordinate

---

[4] For simple kernels like the one we used — see (1.2), the calculation of the convolution can be reduced to two single integrals over u (first sine and cosine Fourier modes).

set in phase space. Poincaré sections are especially effective with orbits in phase space lying on two–dimensional surfaces — whose images become one–dimensional on a section and are thus easy to visualize. The never–breaking solutions for (1.1) and (1.2) that we observe in our numerical experiments appear to do just this, filling two–dimensional tori in (infinite–dimensional) phase space.

The traveling waves (only case where exact analytical expressions are known to us) are specially simple, as their trajectories are one–dimensional curves that reduce to a discrete number of points on a Poincaré section. In particular we show that, with our implementation, they yield a single point. Since in physical space many of the never–breaking solutions appear to be quite close in appearance to a traveling wave, this gives us a reliable way to distinguish them.

Next, in Section 4.2, we the describe general properties of the solutions arising in the long–time[5] simulations. It turns out that, besides traveling waves, equation (1.1) possesses a large class of other never–breaking solutions. The solutions observable in the direct numerical simulations are **global attractors** for the system in (1.1) - (1.2). That is, they appear as the limiting solutions for almost all initial conditions we used. Surprisingly, none of the traveling waves found analytically before — except for the one with maximum energy and a corner in its profile — are found among the attractors. Using Poincaré sections (and projections of the trajectory on lower dimensional spaces) these solutions can be identified as quasiperiodic in time, with two frequencies. Another striking property of these solutions is that they cyclically produce corner type singularities — which appear and disappear on the wave shape — but without ever producing shocks. In fact, these solutions can be thought of as: roughly traveling waves, but with an oscillating shape, where the shape cycle has a period slower than the main period associated with the translation motion of the wave.

In addition to the attracting solutions, we discovered a large family of neutrally stable solutions (presented in Section 4.3), which are also quasiperiodic in time with two periods (but are smooth, with no corners). These cannot be obtained by direct numerical simulation, since they are not attracting, so we had to develop a special continuation process that we briefly explain next (for details see Section 4.3).

It is noteworthy that the attractors form a closed surface (easily visible as a football shaped object[6] by doing projections of the Poincaré sections) "enclosing" the set of all never-breaking solutions — in particular, the traveling waves, that make the "central axis" of this surface. The attractors thus make other never–breaking solutions generally unattainable, shielding the solution trajectories from getting "inside" — at least as long as the evolution is exactly inviscid. In order to "penetrate" the surface, we added a small amount of numerical viscosity. Then it turns out that, after converging to the attracting surface, the solutions start drifting inside, making the other never–

---

[5] Carried past the point where all the shocks disappear

[6] See Figure 4-17.

breaking solutions accessible. We call this slow drift process **adiabatic transition**. If allowed to continue for a sufficiently long time, the second temporal frequency of oscillation (associated with the shape oscillations the waves have) becomes degenerated (with zero amplitude) and periodic in time traveling waves result. Thus, adiabatic transition gives a continuous path from the attracting quasiperiodic solutions with corners to the traveling waves.

As explained above, both in physical space and in the Poincaré sections, the solutions obtained in the numerical simulations appear to have two temporal frequencies (quasiperiodicity). These waves also appear to be, roughly, traveling waves with a superimposed "shape" oscillation. We also can see (numerically) that the traveling waves are neutrally stable to small perturbations. All this motivated us to perform linear stability analysis for the traveling waves, and then to see if the "shape" oscillations can be associated with excitation of a linearized mode near a traveling wave. This we do in Chapter 5. In particular, we look there for perturbations of the steady–state traveling waves $u = V_s(x - st)$ of the form

$$u(x,t) = V_s(x - st) + w(x - st, \omega t)\,, \tag{1.3}$$

quasiperiodic with two frequencies in time. That is, here $w(x - st, \omega t)$ is assumed small and 2π–periodic in both its arguments, with ω the shape oscillation wavefrequency. Since V is also 2π–periodic, s is both the wave speed and the main wavefrequency.

In the moving frame search for periodic in time perturbations of a stationary function on a periodic in space domain can be recast in the form of a linear eigenvalue problem[7]. We show in Section 5.2 that spectrum in this problem is discrete and purely imaginary, yielding neutral stability of the corresponding perturbations. This result fully agrees with the numerical evidence. Perturbations corresponding to the lowest frequency in the spectrum only are observable in the experiments.

---

[7] different for each value of "first" frequency s

Chapter 2

Asymptotic Equations and Periodic Solutions.

2.1 Weakly Nonlinear Equations.

In this section we derive and motivate the main equation (1.1) that will be the object of study in this thesis. Consider the problem of gas motion inside a rigid pipe with circular cross-section of constant radius and closed ends. We consider situations where the motion is essentially one-dimensional and inviscid everywhere inside the pipe (except for thin boundary layers at the walls and near the ends, whose influence we neglect throughout this chapter.) For the bulk of the gas we use the Euler equations of Gas Dynamics, which can be written in the following form (see [7], for example)

$$\begin{aligned} \rho_t + (\rho v)_x &= 0\,, \\ (\rho v)_t + (\rho v^2 + p)_x &= 0\,, \\ (\rho e + \tfrac{1}{2}\rho v^2)_t + (\rho e v + \tfrac{1}{2}\rho v^3 + p v)_x &= 0\,, \end{aligned} \tag{2.1}$$

where ρ is the density, v is the flow velocity, $e = e(\rho\,, S)$ is the internal energy per unit mass, $p = p(\rho\,, S)$ is the pressure, $T = T(\rho\,, S)$ is the absolute temperature and S is the entropy. Clearly $p > 0$, $\rho > 0$ and $T > 0$. We assume standard constitutive relations for the gas, so that the thermodynamic identity

$$TdS = de + p\,d\rho^{-1} \tag{2.2}$$

must apply. That is

$$e_\rho = p/\rho^2 \qquad \text{and} \qquad e_S = T\,, \tag{2.3}$$

which implies (in particular) $p_S = \rho^2 T_\rho$. Furthermore, we must have

$$c^2 = p_\rho > 0\,, \tag{2.4}$$

where $c = \sqrt{p_\rho} > 0$ is the speed of sound.

The boundary conditions at the closed ends of the tube are given by

$$v|_{x=0} = v|_{x=L} = 0\,. \tag{2.5}$$

We choose the length of the tube L and some "typical" values for the density ρ^*, pressure p^* and temperature T^* (to be specified further below in Remark 2.1.3) to nondimensionalize all the variables as follows:

$$\begin{array}{llllllll} x \to \frac{L}{\pi}x\,, & p \to p^* p\,, & \rho \to \rho^*\rho\,, & v \to v^* v\,, \\ t \to \frac{L}{\pi v^*}t\,, & e \to e^* e\,, & T \to T^* T\,, & S \to S^* S + S_0\,, \end{array} \tag{2.6}$$

where $v^* = \sqrt{\frac{p^*}{\rho^*}}$, $e^* = (v^*)^2$, $S^* = \frac{p^*}{T^*\rho^*} = \frac{e^*}{T^*}$ and S_0 is chosen to be (roughly) the mean value of S — see below, Remarks 2.1.1 and 2.1.3. One can easily check that all the prior equations ((2.1), (2.2), (2.3) and (2.4)) take exactly the same form in these non dimensional variables, while in (2.5) we need only replace the tube length L by π. From now on we work with these non dimensional variables.

It is convenient to replace the above problem of gas motion inside a tube with closed ends by an *equivalent* problem with periodic boundary conditions. Given a solution of the original problem above, it is easy to see that it can be extended[1] to a solution of the equations defined for all x, periodic of period 2π (in dimensional variables period $2L$), with v *odd* and with ρ and p (thus also S, T and e) *even*. Conversely, given a solution with these properties, it is easy to see that it must

---

[1] This is done simply by appropriately "reflecting" the solution repeatedly across the boundaries.

satisfy the boundary conditions (2.5). Thus, we replace these conditions by the equivalent ones

$$\begin{aligned} v(x+2\pi,t) &= v(x,t)\,, & v(x,t) &= -v(-x,t)\,, \\ \rho(x+2\pi,t) &= \rho(x,t)\,, & \rho(x,t) &= \rho(-x,t)\,, \\ p(x+2\pi,t) &= p(x,t)\,, & p(x,t) &= p(-x,t)\,, \\ e(x+2\pi,t) &= e(x,t)\,, & e(x,t) &= e(-x,t)\,, \\ S(x+2\pi,t) &= S(x,t)\,, & S(x,t) &= S(-x,t)\,, \end{aligned} \tag{2.7}$$

for arbitrary x and t. Of course, any two of the last four rows here implies the other two.

Remark 2.1.1 *It will turn out that, for the leading order approximation in the asymptotic expansion below, only the* $\pi-$*periodic components of* S *will matter (see Remark 2.1.4).*

Remark 2.1.2 *The equilibrium state is given by* ρ *and* S *constant, with* $v \equiv 0$*. In fact, we can take* ρ^*, p^*, T^* *and* S_0 *above so that* $\rho \equiv 1$ *and* $S \equiv 0$ *at equilibrium, with both partial derivatives of* $p = p(\rho, S)$ *equal to unity. In particular, the sound speed* $c \equiv 1$.

Remark 2.1.3 *We can now specify further the values used in the nondimensionalization above. It is clear from the equations that the mean value of* ρ *must be constant. Thus we choose* ρ^* *so that the mean value of* ρ *is normalized to* 1*. Furthermore, we will consider only small perturbations of the equilibrium state and in this case the mean of* S *changes only at third order*[2]*, even when shocks are present. Thus, we choose* S_0 *so that the mean of* S *vanishes. Finally, we choose* p^* *and* T^* *(equivalently* p^* *and* S^**) so that, in the non-dimensional variables,* $\rho = 1$ *and* $S = 0$ *correspond to a sound speed* $c = 1$ *and* $p_S = 1$.

We now focus on small perturbations of the equilibrium state. Then we can write an asymptotic expansion for the solution (following Majda and Rosales, [18]) of the form

$$\rho = 1 + \epsilon[\sigma_1(x-t,\tau) + \sigma_3(x+t,\tau) + \sigma_2(x,\tau)] + \ldots, \tag{2.8}$$

$$v = \epsilon[\sigma_1(x-t,\tau) - \sigma_3(x+t,\tau)] + \ldots, \tag{2.9}$$

$$S = - \epsilon\sigma_2(x,\tau) + \ldots, \tag{2.10}$$

where $0 < \epsilon \ll 1$ is the expansion parameter and $\tau = \epsilon t$ is the *slow* time over which nonlinear effects operate in this regime. Here σ_1 is the right-moving acoustic wave amplitude, σ_2 is the entropy wave amplitude and σ_3 is the left-moving acoustic wave amplitude.

---

[2] That is, at $O(\epsilon^2)$, where ϵ is the small amplitude parameter. In fact, the rate of change is only $O(\epsilon^3)$, but we will be following the time evolution over long times, of $O(\epsilon^{-1})$ — so that changes can built up to $O(\epsilon^2)$.

From (2.7) and Remark 2.1.3, the functions σ_i above are all 2π−periodic in the appropriate arguments (the phases $x-t$, $x+t$ and x, respectively) and have vanishing means. That is

$$\overline{\sigma}_i = \int_0^{2\pi} \sigma_i(\xi,\tau)\,d\xi = 0 \qquad \text{for} \quad i = 1,2,3\,. \tag{2.11}$$

In the linear approximation all three waves σ_1, σ_2 and σ_3 are mutually independent. In the weakly nonlinear case[3] as above, however, they become coupled. Then they must satisfy certain conditions in order for the approximation to be valid for times t of order $O(\epsilon^{-1})$. These conditions (as shown in [18]) take the form of the following equations[4] for the $\sigma_i(\xi,\tau)$

$$\dot{\sigma}_1 \quad + \beta_1\sigma_1\sigma_1' + \beta_2\int_0^{2\pi}\sigma_2'\left(\tfrac{\xi+\eta}{2}\right)\sigma_3(\eta,\tau)\,d\eta \quad = 0\,, \tag{2.12}$$

$$\dot{\sigma}_2 \qquad\qquad\qquad\qquad\qquad\qquad = 0\,, \tag{2.13}$$

$$\dot{\sigma}_3 \quad - \beta_1\sigma_3\sigma_3' - \beta_2\int_0^{2\pi}\sigma_2'\left(\tfrac{\xi+\eta}{2}\right)\sigma_1(\eta,\tau)\,d\eta \quad = 0\,, \tag{2.14}$$

where β_1 and β_2 are positive constants that depend on the constitutive equations and the nondimensionalization, primes denote differentiation with respect to the phases and dots stand for derivatives with respect to the slow time τ. These equations are to be solved within the class of the 2π−periodic functions of the phases, with vanishing mean values, as pointed out earlier.

We emphasize here that σ_2 does not depend on τ in this approximation. It is thus just given by the initial perturbation to the constant entropy — as follows from (2.10).

So far we have only implemented the periodicity requirements in (2.7) for (2.8)–(2.10), but not the symmetries (ρ must be *even*, etc.) It is easy to see that these are precisely equivalent to the following identity relating σ_1 to σ_3

$$\sigma_1(-\xi,\tau) = \sigma_3(\xi,\tau)\,. \tag{2.15}$$

In addition, we also need σ_2 to be an **even** function of x.

Introduce now the *common* function

$$u(x,t) = \beta_1\sigma_1(x,t) = \beta_1\sigma_3(-x,t)\,, \tag{2.16}$$

---

[3] When ϵ is small, but not infinitesimal.

[4] We have used the fact that the mean values of the σ_i vanish, to simplify the equations in [18].

and the function

$$K(x) = \beta_2 \sigma_2'(\frac{1}{2}x) . \tag{2.17}$$

We note that $K(x)$ is a $4\pi-$periodic *odd* function of its argument, which is given by the initial conditions and is thus "known". We also point out that here we have switched notation, using x instead of ξ to denote the phase arguments in the σ_i's and t instead of τ. Since the original space and time variables x and t of (2.1)–(2.10) will no longer be used in this work (except for Appendix C), this should not cause any confusion.

Then, the whole system (2.12)–(2.14) collapses into the single equation

$$\frac{\partial}{\partial t}u(x,t) + \frac{\partial}{\partial x}\left(\frac{1}{2}u^2(x,t)\right) + \int_0^{2\pi} K(x-y)u(y,t)\,dy = 0 , \tag{2.18}$$

which will be the main object of interest throughout this and the following chapters. The solution $u(x,t)$ must be taken $2\pi-$periodic in x and of vanishing mean (for all times t). We note that the equation is consistent with these requirements, as K has zero mean. This further justifies all the manipulations and assumptions concerning means we did in the context of the nondimensionalization of the equations. In particular, this allowed considerable simplification of the equations in [18] when writing (2.12)–(2.14), by dropping all the terms associated with the vanishing mean values of the σ_i's.

Remark 2.1.4 *Since $K(x)$ is $4\pi-$periodic and odd, it can be written as a Fourier series with general term proportional to* $\sin(\frac{1}{2}nx)$. *On the other hand, since $u(x,t)$ is only $2\pi-$periodic, it is clear that only those terms for which n is even will contribute to the convolution in equation (2.18) for u above. Thus, we might as well drop the component of K which is not $2\pi-$periodic and* **assume that K in (2.18) above is $2\pi-$periodic,** *with Fourier sine expansion*

$$K(x) = \sum_{k=0}^{\infty} P_k \sin(kx). \tag{2.19}$$

We will limit our consideration to the simplest possible kernel

$$K(x) = \sin(x). \tag{2.20}$$

Remark 2.1.5 *Equation (2.18) above can also be used for solutions with shocks. It is already written in the proper conservation form. In terms of the full Gas Dynamics problem, a shock in (2.18) corresponds to a weak shock bouncing back and forth inside the tube.*

In conclusion, we have reduced the full system of equations for the problem of one-dimensional weakly nonlinear motion of an inviscid compressible gas inside a rigid tube with closed ends to the single equation (2.18). The kernel $K(x)$ of the integral term in (2.18) is an odd function and can be expanded into a sine Fourier series, as above in (2.19).

2.2 Traveling wave solutions.

In this section we review the traveling wave solutions for equation (2.18) (which can be written in explicit form) and point out some interesting features they possess. Gabov (in [9]) and Pego (in [20]) showed that equation (2.18) — with the single–mode kernel (2.20) — possesses a one-parameter (except for phase shifts) family of traveling wave solutions

$$u(x - st) = s + b\sqrt{1 - \delta \sin(x - st + \phi_0)}\,. \tag{2.21}$$

Here $s = s(\delta)$ is the wave propagation speed, $b = b(\delta)$ and δ together determine the wave amplitude and shape, and ϕ_0 is an arbitrary phase shift. The parameter δ is, obviously, restricted to the range[5] $0 \leq |\delta| \leq 1$ and we have

$$\begin{aligned} s(\delta) &= -\frac{b}{2\pi} \int_0^{2\pi} \sqrt{1 + \delta \cos y}\, dy\,, \\ b(\delta) &= \frac{2}{\delta} \int_0^{2\pi} \cos y \sqrt{1 + \delta \cos y}\, dy\,. \end{aligned} \tag{2.22}$$

The first equation here guarantees that u above has mean zero; then the second guarantees that equation (2.18) is satisfied. It is easy to see that these formulas give $b(\delta) > 0$ and $s < 0$ for **all** δ. The amplitude of the wave is given by

$$A = \frac{1}{2} b(\delta) \left(\sqrt{1 + |\delta|} - \sqrt{1 - |\delta|} \right) .$$

These parameters as functions of δ are plotted in Figure 2-1.

Remark 2.2.1 *The traveling waves in (2.21) range from the trivial solution $u \equiv 0$ when $\delta = 0$ to a limiting maximum amplitude one for $\delta = \pm 1$. When $|\delta| < 1$ the traveling waves are smooth (in fact analytic) functions of the argument $\xi = x - st + \phi_0$. When δ reaches the critical values $\delta = \pm 1$, the solution loses smoothness and forms a corner singularity (see Figure 2-1). Our numerical calculations show that the presence of corners is typical for the solutions of (2.18), that is: after a transient period dominated by shocks, the solutions evolve into a state without shocks, but with*

---

[5] A sign change in δ is equivalent to a phase shift of π in the wave.

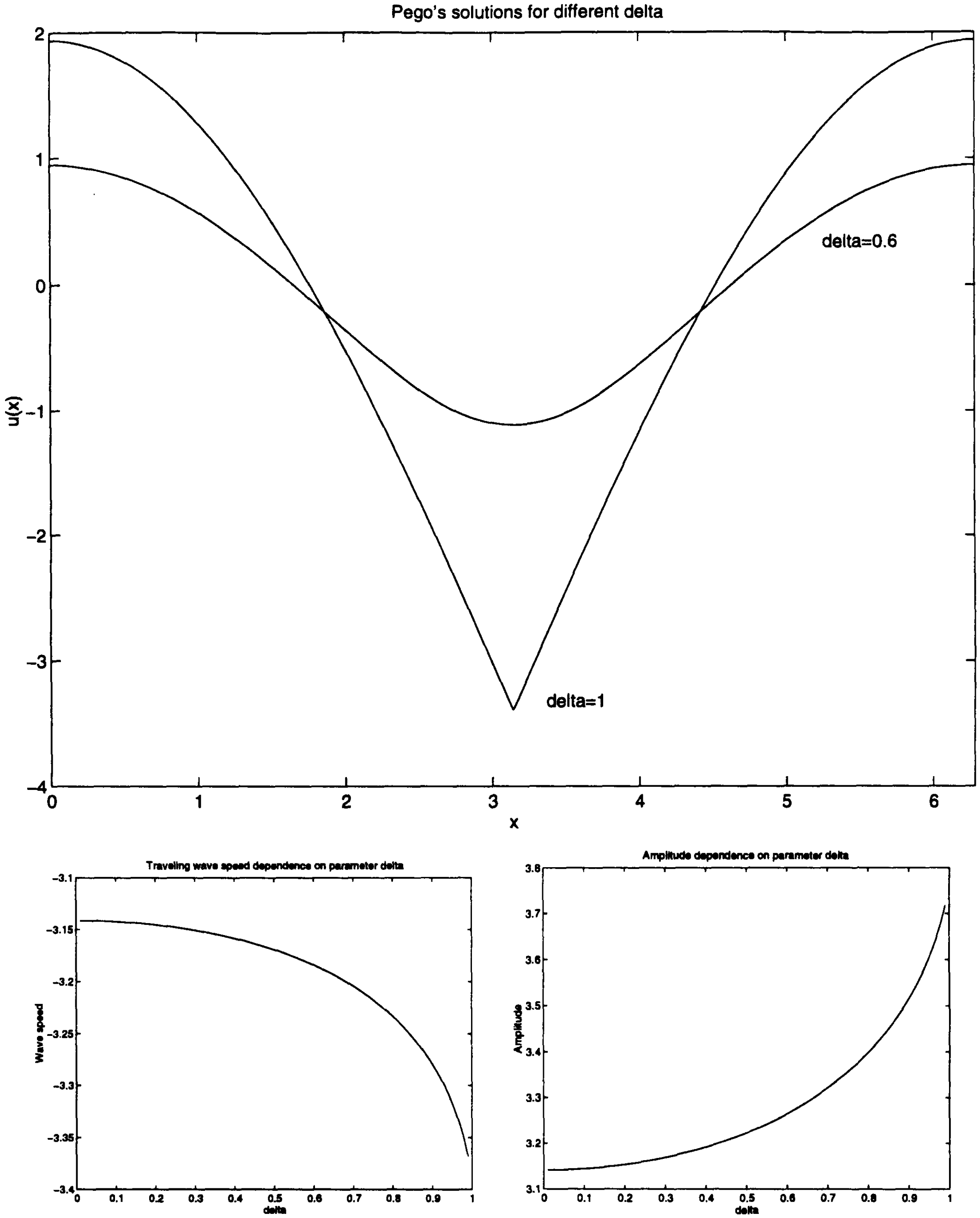

Figure 2-1: The top figure shows two typical traveling wave profiles for $\delta = 0.6$ and 1. The first one is smooth and the second corresponds to the $\delta = 1$ *maximum* amplitude wave with a corner. The two lower figures show graphs of the wave velocity s and the wave amplitude A in terms of the wave parameter δ.

corner singularities.

Remark 2.2.2 *The traveling wave solutions above are also periodic in time, with period* $(2\pi/|s|)$*. The solutions of the form (2.21) are the* **only** *traveling waves for equation (2.18) — with the kernel (2.20) — and they simply do not exist beyond the range* $|\delta| \leq 1$*. It is interesting to note that our numerical experiments suggest that these are also the only (stable) time periodic solutions of equation (2.18).*

It can be shown (see Appendix A) that equation (2.18) preserves the L_2 norm (same as the acoustic energy, see Appendix C)

$$E(t) = \frac{1}{4\pi} \int_0^{2\pi} u^2(x,t)\, dx, \tag{2.23}$$

as long as the solution remains smooth. It can also be shown (see Appendix A, equation (A.10)) that $E(t)$ decays if the solution develops shocks, with the decay rate proportional to the strength of the discontinuities. This property allows us to interpret $E(t)$ above as either the energy or as a negative "generalized entropy" for the equation[6]. From now on we refer to $E(t)$ as simply the energy. It is clear that the traveling waves above in (2.21) span only a **bounded interval** of energy values $0 \leq E \leq E_{max}$. The maximum energy corresponds to $\delta = \pm 1$.

As mentioned above in Remark 2.2.1, the solutions of equation (2.18) can have corners (in fact, they are typical), as illustrated by the corners in (2.21) for $\delta = \pm 1$. Furthermore, the solutions will also have shocks — at least for some period of time after the initial data start evolving. These features impose certain special requirements on any numerical scheme one may wish to use for the for the simulation of (2.18). Such a scheme must be able to accurately handle singularities both of the strong (shock) and weak (corner) type. The details of the numerical scheme we used will be discussed in Chapter 3) of this thesis.

---

[6] In fact, this second interpretation is also physically accurate: see equation (C.9) in Appendix C, showing that the acoustic energy can be related to the physical entropy.

Chapter 3

Numerical Algorithm.

3.1 Choice of Numerical Scheme: Splitting Idea

Most results described in Chapter 4 of this thesis are obtained by performing the long-time numerical integration of model equation

$$\frac{\partial}{\partial t}u(x,t) + \frac{\partial}{\partial x}\left(\frac{1}{2}u^2(x,t)\right) + \int_0^{2\pi} K(x-y)u(y,t)\,dy = 0\,. \tag{3.1}$$

derived in Chapter 2.

The purpose of this Chapter is to give a description of the algorithm we used in the experiments. In our simulations we discovered that shocks and weak discontinuities alike are almost always present during evolution of solutions for (3.1), even when solutions are initially smooth. Moreover, some of the analytic solutions of (3.1) are not smooth, being such for all times (see Chapter 2).

Most numerical schemes need additional care near singularities. Truncation error estimates may fail there, for they usually are based on the assumption, that higher order derivatives of the solution are smooth. Also, characterstics play a very important role in hyperbolic equations such as (3.1), defining local *directions of propagation* of information. If numerical scheme does not take these directions into account, then information from physically irrelevant domains may be used by the scheme, causing spurious oscillations and other instabilities in the neighborhood of singularities.

As we just mentioned, both strong and weak discontinuities are quite typical for solutions of equation (3.1). The mechanism of formation of strong discontinuities is entirely similar to that for the non-viscid Burgers equation

$$u_t + \left(\frac{u^2}{2}\right)_x = 0\,. \tag{3.2}$$

Nonlinear steepening is caused by uu_x term in equation (3.1) and leads to wave breaking. As opposed to the Burgers equation, who does not support non-breaking solutions, (3.1) has linear convolution term $K * u$ with weakly dispersive nature (see Appendix B for details). It acts against wave breaking caused by the nonlinear term. If these two forces "balance" each other, persistent never-breaking solutions, often with weak (or, "corner", because of their shape) singularities may arise[1].

These observations motivated the choice of a numerical scheme as capable of dealing with both strong and weak ("corner") singularities. Typical numerical experiments in the context of our problem involve long time integration of (2.18) with initial conditions of various "arbitrary" shape. In these simulations characteristic time scales are generally observed to be of order of $10^2 - 10^3$ acoustical periods.

Ordinary finite difference or spectral methods are very efficient on smooth solutions. However, they typically break down when encountering singularities as described above. These methods produce high-frequency spurious oscillations near singularities which then diffuse into the interior of the space domain and eventually contaminate the solution. Upon long integration time involved in the experiments it often becomes virtually impossible to determine whether the observed numerical solution is "physical" (what we would get, had the scheme been "exact") or it just reflects accumulated numerical errors.

We have developed a numerical scheme which we believe provides a good resolution for both strong and weak discontinuities. To begin with the construction, we split the spatial operator in (2.18) into two parts:

$$u_t = \mathbf{A}[u] + \mathbf{B}[u], \tag{3.3}$$

where

$$\mathbf{A}[u] = -\frac{\partial}{\partial x}(u^2), \qquad \mathbf{B}[u] = -K * u\,. \tag{3.4}$$

Next, we discretize the time variable t into equal time steps $[t_{n-1}, t_n]$ and approximate (3.3) by the following semi-continuous equation

$$\frac{u^{n+1} - u^n}{\Delta t} = \mathbf{A}[u^n] + \mathbf{B}[u^n]\,. \tag{3.5}$$

Here, $u^n = \tilde{u}(x, n\Delta t)$ is the numerical approximation for a solution at the $n-$th time step and $u^0 = \tilde{u}(x, 0) = u(x, 0)$ is the initial condition. This is an *explicit* scheme, since both spatial operators on the right-hand side of (3.5) use function u evaluated *only* at the "previous" time step.

---

[1] For example, in the periodic "traveling wave" solution (2.21) when $\delta = 1$ (see Figure 2-1).

Now, we break each time step into three "intermediate" sub-steps (fractional step approach):

$$
\begin{aligned}
u^{\star n} &= u^n + \tilde{\mathbf{B}}[u^n]\frac{\Delta t}{2}\,, && (3.6)\\
u'^n &= u^{\star n} + \tilde{\mathbf{A}}[u^{\star n}]\Delta t\,, && (3.7)\\
u^{n+1} &= u'^n + \tilde{\mathbf{B}}[u'^n]\frac{\Delta t}{2}\,. && (3.8)
\end{aligned}
$$

Here, $\tilde{\mathbf{A}}$ and $\tilde{\mathbf{B}}$ are the **discrete analogs** of operators $\mathbf{A}$ and $\mathbf{B}$ in equation (3.3). To accommodate for different behavior these two operators demonstrate we will use different discretization schemes for $\mathbf{A}$ and $\mathbf{B}$ (see Sections 3.2 and 3.3 for detailed description of their construction). We will aim at the construction of a **second order** scheme. Strang ([23, 22]) showed that second order of approximation in both $\tilde{A}$ and $\tilde{B}$ is sufficient to achieve second order for the overall scheme.

Each "intermediate" equation in (3.6)-(3.8) involves only **one** spatial operator and therefore can be treated with a separate algorithm.

It is worthwhile to mention, that the splitting idea in fact does not introduce any extra computational effort into the algorithm, since every two successive time steps can be combined by unifying the last sub-step (3.8) of a "previous" step with the first sub-step (3.6) of a "next" time step in the following fashion

$$u^{\star(n+1)} = u^{n+1} + \tilde{\mathbf{B}}[u^{n+1}]\frac{\Delta t}{2} = u'^n + \tilde{\mathbf{B}}[u'^n]\Delta t + O((\Delta t)^3)\,. \qquad (3.9)$$

$$u'^{(n+1)} = u^{\star(n+1)} + \tilde{\mathbf{A}}[u^{\star(n+1)}]\Delta t \qquad (3.10)$$

This operation introduces only higher-order errors to the method whom we neglect in our consideration. This way, the overall scheme will effectively include only two sub-steps per time step. In other words, only one evaluation of $\tilde{A}$ and $\tilde{B}$ is required at each time step[2].

3.2 Upstream Scheme Construction

The nonlinear operator $\mathbf{A}$ in (3.1), (3.3) can and often does cause the continuity breakdown. It is appropriate therefore to handle it with the scheme specially built for treatment of discontinuous solutions. A broad class of so-called upstream schemes is available for this purpose. Schemes of this family are known for their excellent performance on strong discontinuities, with no generation of spurious oscillations, typical for finite differences. In addition, an extra feature of shock tracking is

---

[2] **With the exception of initial and final time steps.**

easily implementable for them. Shock tracking allows grid points to move along with shocks, which greatly reduces the amount of "numerical viscosity" associated with a scheme. The algorithm we will be using belongs to this class of upstream schemes.

One of the first upstream scheme was introduced by Godunov in [11]. Godunov's idea had been developed later in the works by van Leer [24, 25] and also by Harten and Hyman [13]. All upstream schemes are designed for differential equations written in the so-called "conservative" form

$$u_t(x,t) + f(u(x,t))_x = 0\,. \tag{3.11}$$

The "flux" function $f(u)$ is determined by an equation and in our case is simply

$$f(u) = \frac{u^2}{2}\,. \tag{3.12}$$

To begin, let us for simplicity use **fixed** and **homogeneous** spatial stencils. The whole construction will be adjusted to the case of moving (or inhomogeneous) stencil later in Section 3.2.6 without any difficulties.

3.2.1 Some definitions

First, we introduce a **mesh**, namely, a set of **computational nodes** $\xi_{j+\frac{1}{2}}$. Line segment between $\xi_{j-\frac{1}{2}}$ and $\xi_{j+\frac{1}{2}}$ will be called the ***j*-th computational cell**. Instead of sampling at mesh points (as usually done, for example, in finite difference methods) we will be using the cell averaged values, assuming that these values are constant within each cell. In particular, we define the **cell averages** $\bar{u}_j(t_n)$ as

$$\bar{u}_j(t_n) = \frac{1}{\Delta x} \int\limits_{\xi_{j-\frac{1}{2}}}^{\xi_{j+\frac{1}{2}}} u(x,t_n)dx, \tag{3.13}$$

with $\Delta x = \xi_{j+\frac{1}{2}} - \xi_{j-\frac{1}{2}}$.

Consider now an "elementary" region in the time-space domain, enclosed by the four straight lines $t = t_n$, $t = t_{n+1}$, $x = \xi_{j-\frac{1}{2}}$ and $x = \xi_{j+\frac{1}{2}}$. We can define the **average flux** across cell interface as

$$f_{j-\frac{1}{2}} = \frac{1}{\Delta t} \int\limits_{t_n}^{t_{n+1}} f(u(\xi_{j-\frac{1}{2}},t))dt \tag{3.14}$$

Upon integration over an elementary domain, we can rewrite (3.11) in the integral form

$$\bar{u}_j(t_{n+1}) = \bar{u}_j(t_n) - \lambda(f_{j+\frac{1}{2}} - f_{j-\frac{1}{2}}), \tag{3.15}$$

where the mesh ratio $\frac{\Delta t}{\Delta x}$ is denoted by λ.

The integral form of (3.15) translates into a **numerical scheme** if cell average values introduced by $u_j^n = \bar{u}_j(x, t_n)$ replace the originally continuous function u in (3.15):

$$u_j^{n+1} = u_j^n - \lambda(\hat{f}_{j+\frac{1}{2}} - \hat{f}_{j-\frac{1}{2}}) \tag{3.16}$$

For each n set of u_j^n's represents an approximation at the $n-$th time level. Equation (3.16) expresses therefore transition from $n-$th to $(n+1)-$st time level. Note that original fluxes get replaced by **numerical fluxes** $\hat{f}_{j+\frac{1}{2}}$ whose computation comprises the central part of upstream scheme construction.

In his original paper [11] Godunov introduced a first-order conservative scheme for one-dimensional Gas Dynamics equations based on piecewise-constant approximation idea such as described above. He proposed to compute numerical fluxes $f_{j-\frac{1}{2}}$[3] across cell boundaries using classical result known as the solution of Riemann problem ([7], for example). Method based on this calculation received the name **Riemann solver**. Godunov's method was later extended by van Leer [24, 25] who introduced **piecewise-polynomial** approximations in place of **piecewise-constant** ones. van Leer's modification made it possible to construct higher-order conservative schemes. In this Chapter, we will restrict ourselves to second-order schemes, based on **piecewise-linear** approximations. Even though characteristics are not parallel to each other, they still remain straight lines (at least, in the case of a scalar equation), which makes the first-order method easily upgradable. More detailed discussion of Riemann solver modifications will be given in Section 3.2.5.

We will give now a general description of second-order conservative scheme we used in our numerical experiments. A piecewise-linear approximation used in this scheme can be characterized by a set of cell average values and a set of slopes. As clearly follows from (3.13), slopes do not affect cell averages and are only needed for the higher order of accuracy in flux calculation. Thus, we will not carry the slopes along with cell averages but instead recalculate them on each time step. We call this procedure the **slope reconstruction** and will discuss it later in Section 3.2.4.

In short, the upstream scheme can be put into the following "program".

---

[3] We drop hats for numerical fluxes now and will omit them throughout the rest of this Chapter.

1. START with the set of cell averages.
2. SLOPE RECONSTRUCTION. Slopes are found by interpolating over cell averages.
3. FLUX COMPUTATION. Riemann's problem is solved on every cell interface with the second order of accuracy.
4. SOLUTION UPDATE. Cell averages are recomputed for the next time step by (3.16).

As we show in Section 3.2.6, the extension of this algorithm for nonuniform or moving grids is rather straightforward. Grid points are then allowed to move with shocks, subject to a few regularity constraints. In fact, only one extra step will have to be added to the program sketched above. Namely, before fluxes are computed, we need to track all the shocks by evaluating the velocities of corresponding moving nodes. The flux computation procedure itself also has to be slightly changed. These modifications will be discussed in detail in Section 3.2.6.

3.2.2 Riemann Problem

The classic Riemann problem was originally formulated for the Euler equations of Gas Dynamics with single spatial coordinate. Two quiescent gases at different states are initially contained in a pipe and separated by a thin membrane. The membrane is then quickly removed and the subsequent motion of the gases is studied. It is well known (see [7], e.g.) that the resulting solution has **self-similar** structure with only a few possible configurations of elements (such as rarefaction waves, shocks and contacts) arising from the original discontinuity. We will be using a simplified version of Riemann problem, applied to the scalar in-viscid Burgers equation

$$u_t + \left(\frac{u^2}{2}\right)_x = 0 . \tag{3.17}$$

The initial condition is represented by the following formulas:

$$u(x, t = 0^-) = u_j^n, \qquad x < \xi_{j+\frac{1}{2}}, \tag{3.18}$$

$$u(x, t = 0^-) = u_{j+1}^n, \qquad x > \xi_{j+\frac{1}{2}} . \tag{3.19}$$

In this "scalar" version, only two self-similar configurations are possible, namely, a *single rarefaction wave* and a *single shock.* The entropy condition in this situation reduces to $u_j^n \geq u_{shock} \geq u_{j+1}^n$, therefore, a shock will form only when $u_j^n \geq u_{j+1}^n$. A single expansion fan solves this problem in the opposite case.

$$u(x,t) = \begin{cases} u_j^n & \text{if } x < \frac{1}{2}(u_j^n + u_{j+1}^n)t \\ u_{j+1}^n & \text{if } x > \frac{1}{2}(u_j^n + u_{j+1}^n)t \end{cases}, \qquad \text{when } u_j^n > u_{j+1}^n\,, \tag{3.20}$$

$$u(x,t) = \begin{cases} u_j^n & \text{if } x < u_j^n t \\ \frac{x}{t} & \text{if } u_j^n t < x < u_{j+1}^n t\,, \\ u_{j+1}^n & \text{if } x > u_{j+1}^n t \end{cases} \qquad \text{when } u_j < u_{j+1}\,, \tag{3.21}$$

Shock speed s is computed according to standard jump condition for the Burgers equation.

$$-s[u] + \left[\frac{u^2}{2}\right] = 0\,, \tag{3.22}$$

and can be expressed in terms of the "left" and "right" values of speed u

$$s = \frac{u_l + u_r}{2}\,. \tag{3.23}$$

In this spirit, we compute solutions in the neighborhood of each cell interface and combine the pieces into a "global" solution. One has, however, to impose a restriction on the time step. Self-similar fragments of solution remain valid only as long as they do not intersect with each other. We will require, therefore, that different elements originating from separate cell interfaces never "overlap" with each other during every single time step, or, in other words, inside time strips $t^n < t < t^{n+1}$. This restriction is called the **CFL condition** (see, for example, [7, 17]) and can be expressed in terms of the maximum value of $|u|$ and cell width Δx[4]

$$\Delta t \leq \frac{\Delta x}{|u|_{\max}}\,. \tag{3.24}$$

Solution to the Riemann problem in the form we just described is correct *up to the first order of accuracy* inside whole strip $t^n < t < t^{n+1}$. In particular, we will be using this solution along every cell interface. Clearly, numerical flux is determined by the solution on the interface and can also be computed with the same order of accuracy. To achieve higher accuracy, we will use the generalized version. It will be given a discussion in Section 3.2.6.

---

[4] For nonuniform grids we use the *minimum* value of Δx.

3.2.3 Flux Calculation

Calculation of numerical fluxes is the main part of upstream scheme construction. As an "output" of the Riemann problem, an approximate solution inside time strip $t_n < t < t_{n+1}$ is obtained. Characteristics emanating from each cell $\xi_{j-\frac{1}{2}} < x < \xi_{j+\frac{1}{2}}$, $t = t_n$ form sets of straight lines parallel to each other. Because of the CFL condition only those characteristics emanating from two adjoining to an interface cells can intersect the interface and influence solution along it. In all, there are only three possibilities to consider:

- Characteristics in both adjoining cells are directed away from interface.

  In this case no information is carried across cell interface and the corresponding flux is set identically equal to zero.

- Characteristics in first set are directed towards interface, and in the second set away from it.

  Only one value of u is carried across an interface, it completely determines the flux.

- Characteristics in both adjoining cells are directed towards an interface. Clearly, in this case characteristics emanating from different cells cross forming a shock. Depending which side of the interface a shock is passing, we choose which family of characteristics actually determines flux across the interface. Obviously, these are those characteristics who cross an interface before they entering the shock.

In the first-order schemes flux is constant along the whole interface and is equal to $\frac{u_*^2}{2}$ where u_* is the value (also constant) on the interface.

3.2.4 Slope Reconstruction

Piecewise–constant approximation are capable of supporting only *first-order* schemes. In order to construct schemes of better accuracy, it is necessary to employ approximating functions of more complicated form. In particular, for *second-order* upstream schemes, piecewise–linear functions have to be used. As we argued in Section 3.2.1 we will be using the slope reconstruction procedure rather than "transition" formulas similar to (3.16). Slopes will be computed in the regions where solution is assumed to be reasonably smooth, so that *interpolation formulas* are valid. Cell averages are assumed to be known prior to the beginning of the reconstruction. In our scheme, we implemented two different slope reconstruction procedures proposed originally by van Leer in [24] and Harten and Osher in [14]. We compared the performance of the two algorithms and present and discuss the results of numerical experiments with both methods in Section 3.2.4.

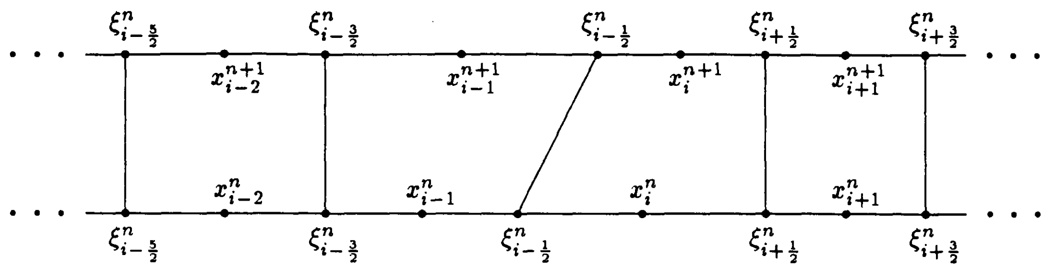

Figure 3-1: Adjustable mesh. $\xi^n_{i+\frac{1}{2}}$'s are the computational nodes. Intervals between them are computational cells. x^n_i are in the middle of cells. Underlying fixed grid (boxes) is not shown.

Reconstruction with van Leer limiters

To generate the slopes, we use the generalized (for the case of non-uniform meshes) centered differences. If one denotes the middle point of j-th cell on the n-th time step by x^n_j (see Figure 3.2.4), the slopes can then be computed according to the following formula

$$s_j = \frac{w_l/(x^n_i - x^n_{i-1}) + w_r/(x^n_{i+1} - x^n_i)}{1/(x^n_i - x^n_{i-1}) + 1/(x^n_{i+1} - x^n_i)}, \tag{3.25}$$

where w_l and w_r stand for the left and right divided differences correspondingly:

$$w_l = \frac{u_i - u_{i-1}}{x^n_i - x^n_{i-1}}, \qquad w_r = \frac{u_{i+1} - u_i}{x^n_{i+1} - x^n_i}. \tag{3.26}$$

One can check that (3.25) approximates smooth functions with the second order of accuracy and it degenerates into an ordinary *centered difference* scheme when mesh is homogeneous.

B. van Leer [24, 25] considered schemes with TVD ("Total Variation Diminishing") properties. He proved that reconstructed slopes must satisfy certain ***monotonicity*** requirements in order to be TVD. In particular TVD yields the absence of spurious oscillations. He called these restrictions the **slope limiters** since in the essence they restrict the range of slopes. We implemented both **weak** and **strong** slope limiters. In its weak form the monotonicity constraint requires that approximating function in each cell takes values strictly within the range spanned by the averages of two neighboring cells. Strong monotonicity prohibits an approximating function in each cell $(\xi_{j-\frac{1}{2}}, \xi_{j+\frac{1}{2}})$ to exceed the average of cell value u^n_j and the *larger* of two neighboring values. It also does not allow the slope to fall below the average of u^n_j and the *smaller* of two neighboring values.

In the first sweep of the reconstruction procedure we determine the slopes according to (3.25).

In the second sweep we check the monotonicity constraints and correct the slopes. In the case of weak monotonicity constraint van Leer limiters take the following form

$$(s_i)_{weak} = \begin{cases} \min\{|s_i|, \dfrac{2(u_{i+\mathrm{sign}(s_i)} - u_i)}{d_i}, \dfrac{2(u_i - u_{i-\mathrm{sign}(s_i)})}{d_i}\} * \mathrm{sign}(s_i), & \\ \qquad \text{if} \quad \mathrm{sign}\ (u_i - u_{i-1}) = \mathrm{sign}\ (u_{i+1} - u_i) = \mathrm{sign}\ s_i\ , & \\ 0, \qquad \text{otherwise.} & \end{cases} \tag{3.27}$$

Strong monotonicity takes the form of

$$(s_i)_{strong} = \begin{cases} \min\{|s_i|, \dfrac{u_{i+\mathrm{sign}(s_i)} - u_i}{d_i}, \dfrac{u_i - u_{i-\mathrm{sign}(s_i)}}{d_i}\} * \mathrm{sign}(s_i), & \\ \qquad \text{if} \quad \mathrm{sign}\ (u_i - u_{i-1}) = \mathrm{sign}\ (u_{i+1} - u_i) = \mathrm{sign}\ s_i & \\ 0, \qquad \text{otherwise.} & \end{cases} \tag{3.28}$$

Strong monotonicity condition limits the slope range twice as strong as weak monotonicity, as easy to see from (3.27) and (3.28). Both strong and weak van Leer's limiters imply zero slope when u_j^n is simultaneously either greater or smaller than u_{j-1}^n and u_{j+1}^n. In particular, they impose zero slope at the local extremum points. Solutions of (2.18) often have weak (corner type) discontinuities at the local extrema. Therefore, van Leer slope limiters lead to effective "shaving off" the corners and production of extra numerical noise at these locations. The numerical experiments we need to conduct require large computational times and uniformly high accuracy, including vicinities of singularities. Thus, it may be profitable to sacrifice the TVD properties in order to achieve better resolution near singularities.

Reconstruction with UNO algorithm

As an alternative approach to the van Leer's schemes we used the so-called UNO reconstruction algorithm originally proposed by Collela and Woodward in [6] and Harten and Osher in [14].

Following Collela and Woodward, we start with piecewise–parabolic interpolant $Q(x; W)$ approximating a piecewise–smooth function $W(x)$ uniformly with the third order and its derivative with the second order of accuracy:

$$Q(x_i^n; W) = W(x_i^n) = W_i\,,$$

$$Q(x; W) = W(x) + O((\Delta x)^3)\,, \tag{3.29}$$

$$\tfrac{d}{dx}Q(x_i^n \pm 0; W) = \tfrac{d}{dx}W(x) + O((\Delta x)^2)\,.$$

The interpolant $Q(x;W)$ is composed of quadratic polynomials pieced together at cell middle points x_i^n (see Figure 3.2.4)

$$Q(x;W) = q_{i+\frac{1}{2}}(x;W), \qquad x_i^n \le x \le x_{i+1}^n \,. \tag{3.30}$$

An equation of parabola $q_{i+\frac{1}{2}}(x;W)$ can be written in the following form

$$\begin{aligned} q_{i+\frac{1}{2}}(x;W) =& W_i + d_{i+\frac{1}{2}}W/\Delta x \cdot (x - x_i^n) + \\ & \frac{1}{2}D_{i+\frac{1}{2}}W \cdot (x - x_i^n)(x - x_{i+1}^n)/\Delta x^2 \,, \end{aligned} \tag{3.31}$$

where

$$d_{i+\frac{1}{2}}W = W_{i+1} - W_i \tag{3.32}$$

and coefficient $D_{i+\frac{1}{2}}W$ is related to the curvature of $q(x;W)$

$$D_{i+\frac{1}{2}}W = q''_{i+\frac{1}{2}}(x;W)(\Delta x)^2 \,. \tag{3.33}$$

We select $D_{i+\frac{1}{2}}W$ from two possible values. It is feasible to construct a parabola through points (x_i^n, W_i), (x_{i+1}^n, W_{i+1}) using either of (x_{i-1}^n, W_{i-1}) and (x_{i+2}^n, W_{i+2}). Parabola with the "least oscillatory" behavior[5] is then selected as an answer. This switch is accomplished by the min-mod function:

$$D_{i+\frac{1}{2}}W = m(D_iW, D_{i+1}W) \,, \tag{3.34}$$

where D_kW is the curvature of parabola through points x_{k-1}^n, x_k^n and x_{k+1}^n. Function $m(x,y)$ returns the value with the least absolute value, when both arguments are of the same sign and zero otherwise.

$$m(x,y) = \begin{cases} s \cdot \min(|x|,|y|) & \text{if } \operatorname{sign}(x) = \operatorname{sign}(y) = s \\ 0 & \text{otherwise} \,. \end{cases} \tag{3.35}$$

The UNO algorithm constructs the slopes in two steps. Firstly, a **piecewise–parabolic inter-**

---

[5] That is, deviating the least from the straight line connecting points (x_i^n, W_i) and (x_{i+1}^n, W_{i+1}).

polant is build to approximate the *piecewise-constant* function $u_n(x)$, composed of the cell averages

$$u_n(x) = u_i^n, \qquad \text{when } \xi^n_{i-\frac{1}{2}} < x \leq \xi^n_{i+\frac{1}{2}}) \tag{3.36}$$

in the way described above. Secondly, slope in each cell $(\xi^n_{i-\frac{1}{2}}, \xi^n_{i+\frac{1}{2}})$ is computed as the slope for the interpolant, applying the same min-mod switch (3.35) to two slopes of parabolas pieced together at the cell middle point x_i^n

$$S_j = \Delta x \cdot m(\frac{d}{dx}Q(x_j^n - 0, u^n), \frac{d}{dx}Q(x_j^n + 0, u^n)) \, . \tag{3.37}$$

This completes the slope reconstruction process.

Comparison of Reconstruction Methods

Since we are tracking shocks no matter which reconstruction algorithm is used, dissipation at the "corners" becomes the major source of numerical errors. We show the results of test runs on Figure 3-2. Standard hat function

$$f(x) = \begin{cases} x, & \text{if } 0 \leq x < \pi \\ 2\pi - x, & \text{if } \pi \leq x \leq 2\pi \end{cases} \tag{3.38}$$

was used as an initial condition and the in-viscid Burgers equation as a model to test reconstruction algorithms. The exact solution is well-known. We placed it on Figure 3-2 for comparison. Clearly, none of the reconstruction algorithms delivers perfect resolution of the corner type singularities for the scalar Burgers equation. As expected, TVD (van Leer's type) scheme smears corners at the extremum more significantly as compared with the UNO-type scheme. The latter smears a typical corner singularity over only 2-3 points as compared to 5-7 offset points in the case of the weak van Leer limiters and 10-12 points in the case of a strongly monotone scheme. Accordingly, we opted to use the UNO algorithm for the slope reconstruction in all of our experiments.

3.2.5 Flux Correction

After the slopes are found, the next step is to compute the numerical fluxes. Since we need to calculate fluxes with **second order** of accuracy rather than first, the Riemann solver in the form described in Section 3.2.2 needs to be slightly modified.

Characteristics will not be piecewise parallel to each other when one replaces a piecewise–constant approximation by a piecewise–linear one. They will remain, however straight lines when a scalar

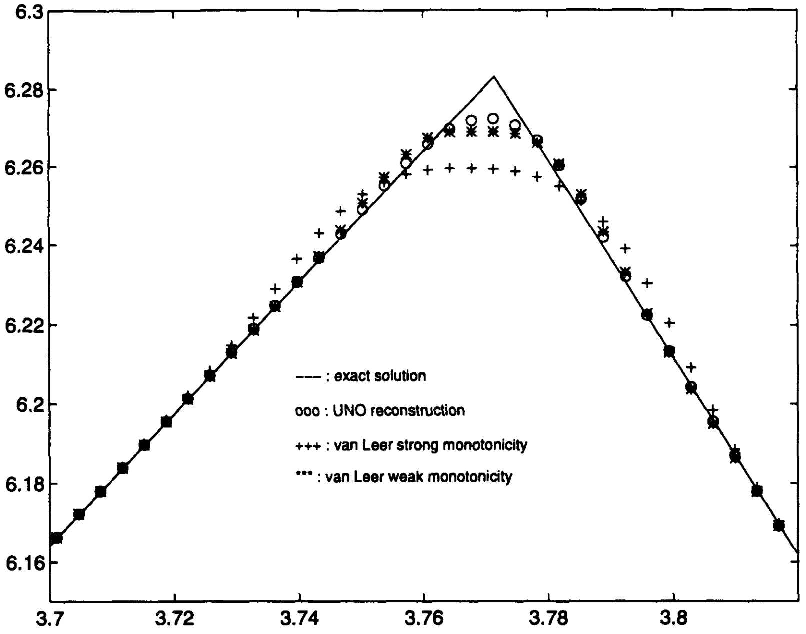

Figure 3-2: Performance of schemes with UNO and van Leer slope reconstruction. Non-viscid Burgers equation. Evolution of a "hat" function.

conservation law (3.11) is considered. Slopes calculated in Section 3.2.4 determine where compression or rarefaction waves or shocks will form inside time strip $t_n < t < t_{n+1}$. The new initial value problems formulated at each cell interface are not in the form the classical Riemann problems any longer. Fortunately, it is easy to extend the Riemann problem solution for this case. It is certainly not true that flux across a cell boundary is constant in this case, but since we are interested only in the *second-order approximation* to the flux rather than the exact answer, we can use an average flux across interface in the "midpoint rule" manner. Errors introduced this way can be neglected in our consideration

$$
\begin{aligned}
f_{j-\frac{1}{2}}\Delta t &= \int_{t_n}^{t_{n+1}} f(u(\xi_{j-\frac{1}{2}}(t),t))\,dt \\
&\approx f(u(\xi_{j-\frac{1}{2}}(t_n+\frac{\Delta t}{2}),t_n+\frac{\Delta t}{2})\Delta t + O(\Delta t^3).
\end{aligned}
\tag{3.39}
$$

We have introduced the **node trajectory** $\xi_{j-\frac{1}{2}}(t)$ as a function of time t on a moving grid. To agree with notation already in use, $\xi_{j-\frac{1}{2}}(t_n) = \xi^n_{j-\frac{1}{2}}$. In order to compute fluxes we determine only a *single value* of u at the middle point of an interface and use (3.39). We use the idea of "tracking back" the characteristics in this calculation. Again, similarly to the case of characteristics parallel to each other, we check only two neighboring cells for the influx of information. We search for characteristics emanating from either of the adjacent cells and crossing interface precisely in the middle point. Once these characteristics are found, the solution of Riemann problem of Section 3.2.2 is used for the values carried by these characteristics. This method provides *second order* of accuracy to the scheme everywhere except locations of strong compression waves or shocks.

3.2.6 Adjustable Grid

Conservative schemes work very well when functions they approximate do not vary too much. However, they lose accuracy considerably if solutions vary by **finite quantities** inside a single cell. Typically these variations occur when a shock or very strong compression wave moves through the grid. When shock passes through a cell upstream method with fixed mesh can not distinguish between the two sides of a shock and takes an average across it. Because of this averaging scheme becomes locally **zeroth-order** with shock spreading over several cells, forming a "staircase" structure. In order to avoid such effects we use **adjustable grid**. The idea is to make grid points sensitive to shocks and allow them to move when shocks pass. This way integration (or, in other words, averaging) across shocks becomes completely eliminated.

Moving and Fixed Meshes

We will require certain additional notation and restrictions to work with moving grids. Following Harten and Hyman [13] and also Vaynblat [26] we introduce two meshes in the space domain: an **underlying fixed mesh** and a **moving grid** consisting of nodes $\xi_{j+\frac{1}{2}}$ as described in Section 3.2.1. Points y_j on the fixed grid will be distributed uniformly on the interval $[0, 2\pi]$ and placed at $0, \frac{2\pi}{N}, \frac{4\pi}{N}, ..., \frac{2(N-1)\pi}{N}, 2\pi$, where N is the overall grid resolution. We will call intervals between y_j's the **boxes**. Nodes on a moving grid will be denoted by $\xi^n_{j+\frac{1}{2}}$ as before, with an additional subscript n reflecting the ability to change position from one time step to another. Intervals between them will still be called the **cells**.

Integral Relation Modification

Conservation law in the integral form (3.16) easily generalizes for the case of moving grid. Rectangular "elementary region"

$$\xi_{j-\frac{1}{2}} < x < \xi_{j+\frac{1}{2}}, \; t_n < t < t_{n+1} \tag{3.40}$$

transforms into a trapezoidal region such as the one shown on Figure 3-3.

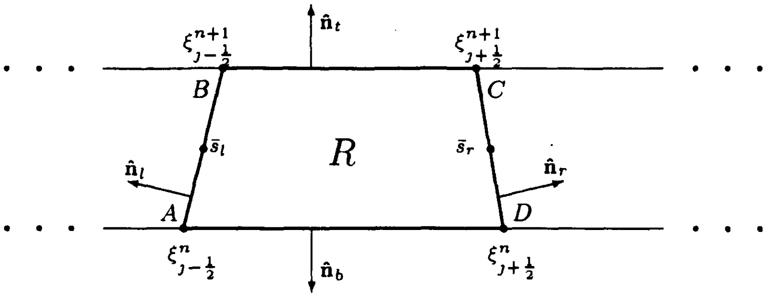

Figure 3-3: Elementary trapezoidal region for moving grid.

One can treat differential equation (3.11) as a *divergence relation* for vector field $\mathbf{F} = (u, f(u))$ and use Gauss divergence theorem to obtain the modified version of (3.15) (see Figure 3-3)

$$\iint\limits_{R} \nabla \cdot \mathbf{F} \, dA = \int\limits_{ABCDA} \mathbf{F} \cdot \hat{\mathbf{n}} \, ds \,. \tag{3.41}$$

Here $\hat{\mathbf{n}}$ is the outer normal unit vector. Integration over top and bottom parts of the contour gives average values of u in jth cell computed at $n-$th and $(n+1)-$st time levels

$$\bar{u}_j(t_n) = \frac{1}{(\xi^n_{j+\frac{1}{2}} - \xi^n_{j-\frac{1}{2}})} \int\limits_{\xi^n_{j-\frac{1}{2}}}^{\xi^n_{j+\frac{1}{2}}} u(x, t_n) \, dx \,, \tag{3.42}$$

$$\bar{u}_j(t_{n+1}) = \frac{1}{(\xi^{n+1}_{j+\frac{1}{2}} - \xi^{n+1}_{j-\frac{1}{2}})} \int\limits_{\xi^{n+1}_{j-\frac{1}{2}}}^{\xi^{n+1}_{j+\frac{1}{2}}} u(x, t_{n+1}) \, dx \,. \tag{3.43}$$

Special cases when trapezoid degenerates into a triangle require special attention and will be addressed later in this Section.

Unit normal vector to AB and CD is computed according to

$$\hat{\mathbf{n}} = \frac{(-k, \; 1)}{\sqrt{1+k^2}} \,, \tag{3.44}$$

where k is the slope of either of AB and CD on $x - t$ plane. Therefore, corrected flux across a slanted boundary can be computed according to the following formula (analogous formula is valid for the other side of the trapezoid, CD)

$$f^*_{j-\frac{1}{2}} = \int\limits_{A}^{B} \frac{-ku(s) + f(u(s))}{\sqrt{1+k^2}} \, ds \,, \tag{3.45}$$

where s is the parameter along the boundary. Total length of the boundary is, as easy to see, equal to $\sqrt{1+k^2}\Delta t$. To compute the integral in (3.45) we use the "midpoint" rule the same way we did in the case of a fixed grid. Therefore, modified flux can be found approximately as

$$f^*_{j-\frac{1}{2}} \approx \frac{-ku(\bar{s}_l) + f(u(\bar{s}_l))}{\sqrt{1+k^2}}(\sqrt{1+k^2}\Delta t) = (-ku(\bar{s}_l) + f(u(\bar{s}_l)))\Delta t\,, \tag{3.46}$$

where we have denoted by $\bar{s}_l$ the middle point of AB (see Figure 3-3). Error, introduced by the "midpoint" rule is $O(\Delta t)^3$. Analogously,

$$f^*_{j+\frac{1}{2}} \approx \frac{-ku(\bar{s}_r) + f(u(\bar{s}_r))}{\sqrt{1+k^2}}(\sqrt{1+k^2}\Delta t) = (-ku(\bar{s}_r) + f(u(\bar{s}_r)))\Delta t\,, \tag{3.47}$$

where $\bar{s}_r$ stands for the middle point of CD on Figure 3-3.

Now the modification of numerical scheme (3.16) for moving meshes is complete:

$$u_j^{n+1} = \frac{\xi^n_{j+\frac{1}{2}} - \xi^n_{j-\frac{1}{2}}}{\xi^{n+1}_{j+\frac{1}{2}} - \xi^{n+1}_{j-\frac{1}{2}}}\, u_j^n - \frac{\Delta t}{\xi^{n+1}_{j+\frac{1}{2}} - \xi^{n+1}_{j-\frac{1}{2}}}(f^*_{j+\frac{1}{2}} - f^*_{j-\frac{1}{2}})\,. \tag{3.48}$$

Regularity Conditions

As nodes $\xi^n_{j+\frac{1}{2}}$ move on the computational grid, they may cross boundaries of their boxes and start interacting with each other. It leads to the increase of concentration of moving grid points inside some of the boxes, while other boxes contain no nodes at all. Under such circumstances resolution of a scheme becomes **nonuniform** and overall accuracy decreases. Additional problems arise when two moving towards each other shocks collide. Clearly, conflicts between two or more moving nodes can occur. To resolve interaction conflicts and preserve the uniformity of a scheme, we will formulate certain rules regulating motion of nodes on fixed grid, which we call the *regularity conditions*. They must hold for all times:

1. At each time step scheme must remain **conservative**;
2. Each box may contain only **one** node;
3. Each moving node must remain in its own box;
4. Only nodes **immediately adjacent** to shocks are allowed to move;
5. Nodes not currently in motion must stay exactly in the **middle** of their boxes;
6. Speed of the moving nodes depends entirely on the speed of a corresponding shock.

Shock Tracking

Shock tracking is a very effective tool to reduce numerical viscosity at discontinuities. Since only relatively large jumps in the solution must be treated as shocks, we should "teach" the scheme to distinguish between shocks and ordinary points. Since tracking is computationally expensive, we allow only a small fraction of nodes (roughly equal to the number of shocks in the domain) to move. The selection is done by imposing a certain constant threshold, limiting maximum gradient the scheme can handle without tracking the corresponding nodes. The choice of a threshold is determined by the two main criteria. If a threshold is too large, the scheme will not see small shocks and average across them, smearing discontinuity to several neighboring cells. Conversely, if threshold is too small, the algorithm will track too many fake shocks thus making computations unnecessarily complicated. As soon as shock has been captured, corresponding cell interface $\xi^n_{j+\frac{1}{2}}$ is set to move in such a way that its trajectory should coincide with the trajectory of passing shock. Shock position $L(t)$ can be determined from the Rankine-Hugoniot jump condition (in the form of a differential equation) (3.23)

$$S_{i+\frac{1}{2}}(t) = \frac{dL_{i+\frac{1}{2}}}{dt} = \frac{1}{2}(v_l(t, L_{i+\frac{1}{2}}(t)) + v_r(t, L_{i+\frac{1}{2}}(t)))\,, \tag{3.49}$$

with the initial condition on the "base" $t = t_n$

$$L_{i+\frac{1}{2}}(t_n) = \xi^n_{i+\frac{1}{2}}\,, \tag{3.50}$$

where $L_{i+\frac{1}{2}}(t)$ is the shock position at time t, v_l and v_r are the values carried by the "left" and "right" characteristics crossing the shock path at time t. Assuming that velocity profile is piecewise-linear, with mean values u_l and u_r, slopes s_l and s_r and cell size $2d_l$ and $2d_r$ it is easy to find the values of v_l and v_r. Suppose that these values are carried by characteristics emanating from x_l^* and x_r^* correspondingly (see Figure 3-4)

$$v_l(t) = u_l + s_l(x_l^*(t) + d_l)\,, \tag{3.51}$$

$$v_r(t) = u_r + s_r(x_r^*(t) - d_r)\,. \tag{3.52}$$

We made base points x_l^* and x_r^* time dependent to reflect the property of corresponding characteristics to intersect at time t.

At the same time calculation of distances covered by each of these characteristics in time t returns

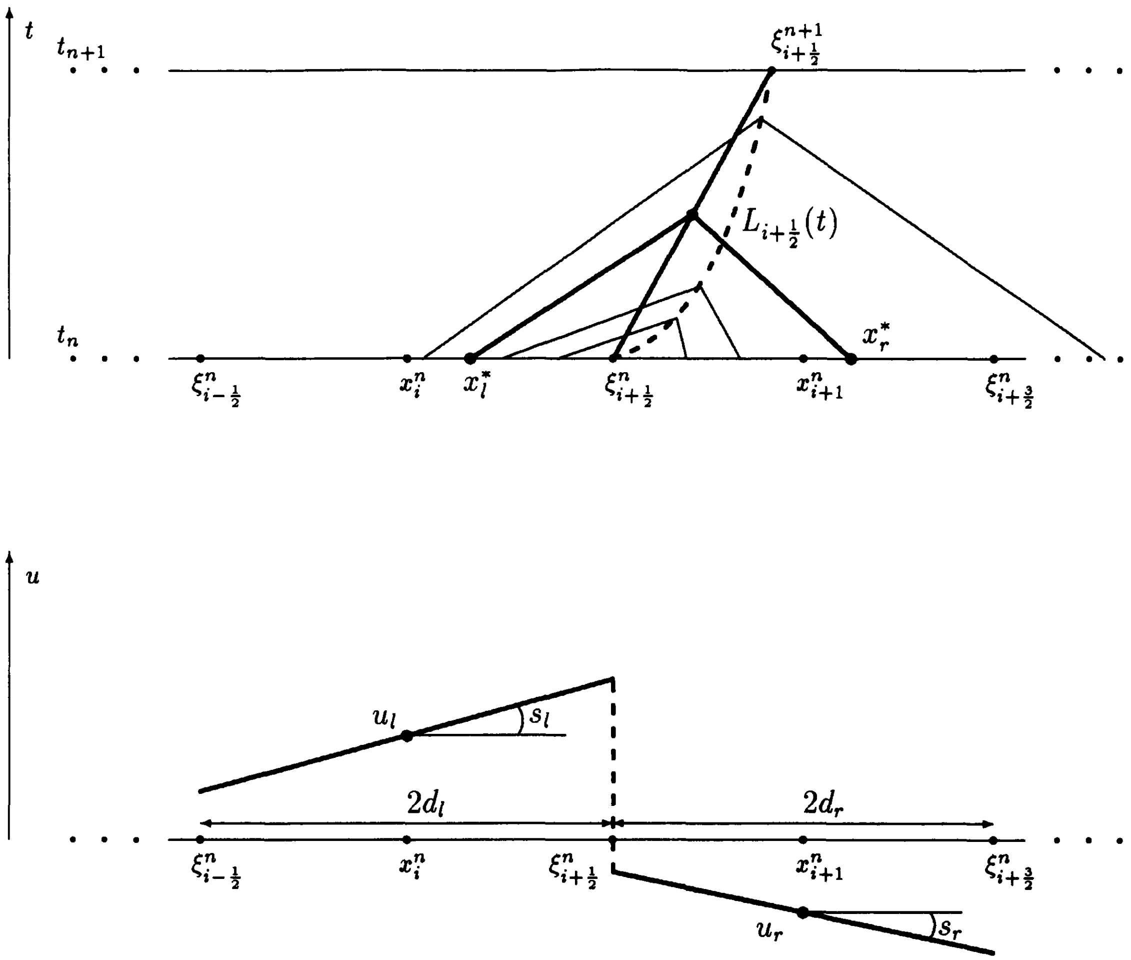

Figure 3-4: Moving node speed computation. Shock path is approximated by the parabola. Flux is computed at the middle point of the nodal trajectory. Piecewise-linear approximation.

$$L_{i+\frac{1}{2}}(t) - x_l^* = t \cdot v_l(t)\,, \tag{3.53}$$

$$L_{i+\frac{1}{2}}(t) - x_r^* = t \cdot v_r(t)\,. \tag{3.54}$$

Substituting (3.51)-(3.52) into (3.53)-(3.54) we can solve for base points x_l^* and x_r^*:

$$x_l^* = \frac{L_{i+\frac{1}{2}} - tu_l - ts_l d_l}{1 + s_l t}\,, \tag{3.55}$$

$$x_r^* = \frac{L_{i+\frac{1}{2}} - tu_r + ts_r d_r}{1 + s_r t}\,, \tag{3.56}$$

and reduce (3.49) to a single ODE

$$\frac{dL_{i+\frac{1}{2}}}{dt} = \frac{1}{2}\left(u_l + s_l \frac{L_{i+\frac{1}{2}} - tu_l + d_l}{1 + s_l t} + u_r + s_r \frac{L_{i+\frac{1}{2}} - tu_r - d_r}{1 + s_r t} \right) . \tag{3.57}$$

Since we are interested in the solution to (3.49) for $t_n < t < t_{n+1}$ only and second order of accuracy suffices for our purposes, we expand (3.57) for small $t - t_n$ and solve it approximately. Shock path can be fitted by a parabola (see Figure 3-4)

$$L_{i+\frac{1}{2}}(t) = \xi^n_{i+\frac{1}{2}} + at + \frac{bt^2}{2} + O(t - t_n)^3 , \tag{3.58}$$

where constants a and b can be found by expanding equation (3.57) near $t = t_n$ and retaining terms proportional to $(t - t_n)$ and $(t - t_n)^2$ only:

$$a = \frac{1}{2}(u_l + u_r + s_l d_l - s_r d_r) , \tag{3.59}$$

$$b = \frac{1}{2}(s_l a + s_r a - s_l u_l - s_r u_r) . \tag{3.60}$$

These constants determine the final position of a shock at $t = t_{n+1}$ up to the second order of accuracy. The correct set of characteristics can then be chosen to find the correct flux across slanted interface.

Note. Instead of explicitly using parabolic shock paths we replace them by **straight lines** connecting initial and final shock positions (see Figure 3-4). Input for the corresponding Riemann problem is taken from the values at the middle points of these straight lines rather than at the middle points of parabolas themselves. Error introduced by this simplification is of order of $(\Delta\xi)^2$ locally[6]. However, according to Vaynblat ([26]), it is not possible to achieve higher accuracy near shocks on a moving grid with piecewise-linear slope reconstruction anyway without better resolving near shocks[7]. So, this error can be neglected.

Relaying Algorithm

To satisfy regularity requirements formulated in Section 3.2.6 we implement the relay-type algorithm. Each moving node $\xi^n_{i+\frac{1}{2}}$ is allowed to move inside its own (fixed) box $y_i < x < y_{i+1}$ without any additional restrictions as long as no other nodes are present in the same box. The CFL condition prohibits all the nodes from moving farther than to one of the two adjacent boxes during each time step. Once node $\xi_{i+\frac{1}{2}}$ enters the neighboring box, the relay switch turns on and checks for other nodes in this box. If more than one node are present in one box at $t = t_{n+1}$, we call this situation a conflict and let the algorithm resolve it. Regularization is performed box-wise. Below we consider

---

[6] Global error is only of the first order.

[7] It is still considerably better than local zeroth order near shocks for fixed grids.

all possible conflicts on a moving grid.

Case 0. There is only one node in a box, it does not move during current time step and it is in the middle of the box.

Do nothing. This is a regular node.

Case 1. Moving node enters a box containing no other nodes.

No adjustments are necessary. The node remains at its final position.

Case 2. Moving node enters a box with another fixed node in the middle.

A stationary node is removed, a moving node remains at its final position.

Case 3. One moving node enters a box with another one moving inside the box.

Here we clearly get two-shock interaction conflict. Two conflicting nodes are replaced by an "averaged" one. The position of the average node L_* is determined by the relative strengths of the two interacting shocks $L_l(t_{n+1})$ and $L_r(t_{n+1})$.

$$L_* = L_l(t_{n+1}) + D_r \frac{L_r(t_{n+1}) - L_l(t_{n+1})}{D_l + D_r}, \tag{3.61}$$

where D_l and D_r are the strengths of left and right shocks L_l and L_r correspondingly.

Case 4. Moving node enters a box with another node inside the box and third node entering this box from the other side.

This is a three-node interaction conflict. This situation is treated much similarly to the previous case. All three nodes get replaced by a single node with average position L_* computed as following

$$\begin{aligned} L_* = \; & L_l(t_{n+1}) + \\ & \frac{D_c(L_c(t_{n+1}) - L_l(t_{n+1})) + D_r(L_r(t_{n+1}) - L_c(t_{n+1}))}{D_l + D_c + D_r} \end{aligned} \tag{3.62}$$

Case 5. No nodes are found in a box at $t = t_{n+1}$.

Moving node has just traveled to an adjacent box. New node must be created at the middle of the box.

Case 6. There is only one node in a box, it does not move during current time step and it is placed not in the middle of the box.

To keep mesh as uniform as possible this node get placed at the middle of the box.

Solution Update on a Moving Grid

As we mentioned before, "elementary" trapezoidal regions, such as, for example, shown on Figure 3-3 can degenerate into triangular regions or, conversely, may extend to include neighboring regions. After the completion of regularization process discussed in the previous Section, exactly one node is placed in each box. During regularization, we need also to keep track of line connectors between nodes on the n−th and $(n+1)$−st time levels. Using these connectors, we form elementary regions in such a way that they include exactly one cell on the top (at the "next" time level t_{n+1}). Then we update the solution for the next time level. Again, we reduce the general problem to considering only several possible cases.

Case 0. Two neighboring nodes remain in their corresponding boxes (see Figure 3-5). Even though both nodes can be moving during current time step, they do not cross boundaries of the boxes and do not create interaction conflicts. This is the regular case. The "elementary" region is a trapezoidal or a rectangle (when neither node is moving).

Case 1. Two neighboring nodes travel to the right/left box simultaneously (see Figures 3-6 and 3-7). Both nodes correspond to shocks moving in the same direction. Elementary region is a slanted trapezoidal in this case.

Case 2. A node moves out of the box, a new node is generated in the middle of this box (see Figures 3-8 and 3-9). Two nodes on the $(n+1)$−st time level have the same origin. Elementary region transforms into a triangle.

Case 3. Two nodes merge at the $(n+1)$−st time level (see Figures 3-10 and 3-11). Since the top part of elementary region degenerates into a point and does not contain any cells at the $(n+1)$−st time level, we will need to include an *additional* cell in order to create a valid elementary region[8].

Case 4. Three nodes merge into a single node (see Figure 3-12). Typical setup when such conflict occurs is when two shocks moving in opposite direction collide with each other. One needs to use three cells at the "previous" time level t_n in order to create a valid elementary region.

---

[8] Had we removed degenerate regions from the scheme we would have committed a "conservation crime" – violation of conservation properties.

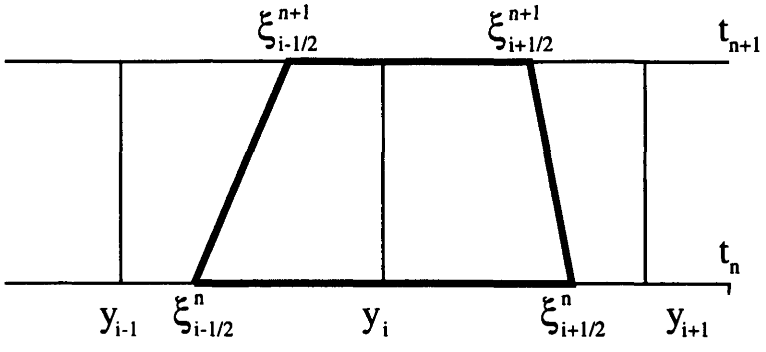

Figure 3-5: Grid regularization. Regular case.

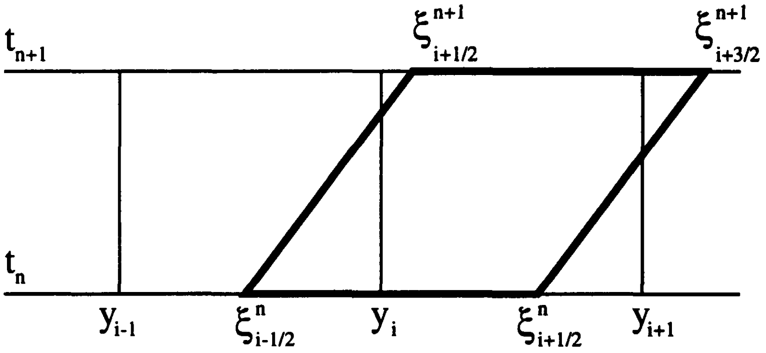

Figure 3-6: Grid regularization. Both nodes move to neighboring right boxes simultaneously. No regularization required.

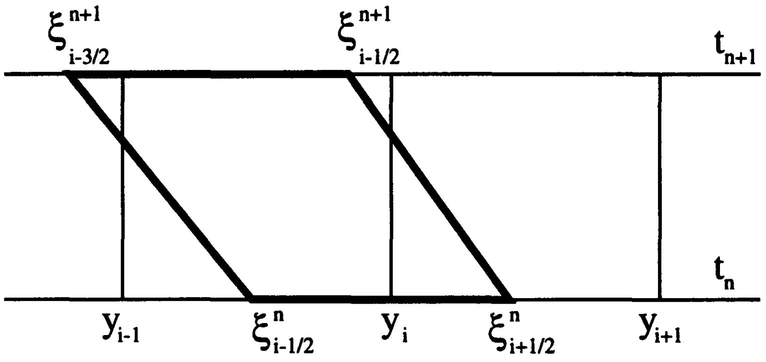

Figure 3-7: Grid regularization. Both nodes move to neighboring left boxes simultaneously. No regularization required.

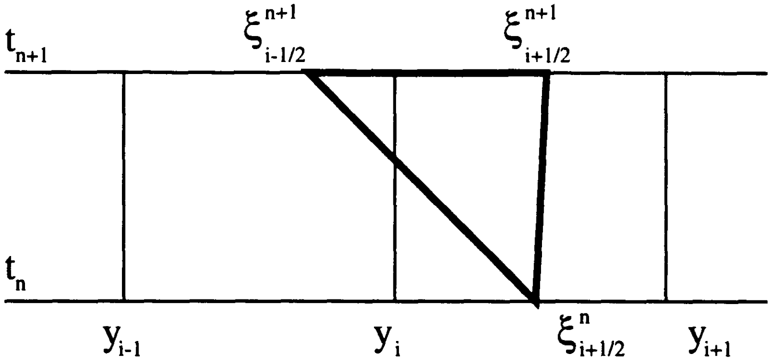

Figure 3-8: Grid regularization. Node moves to neighboring left box, new node generated. Triangular elementary region.

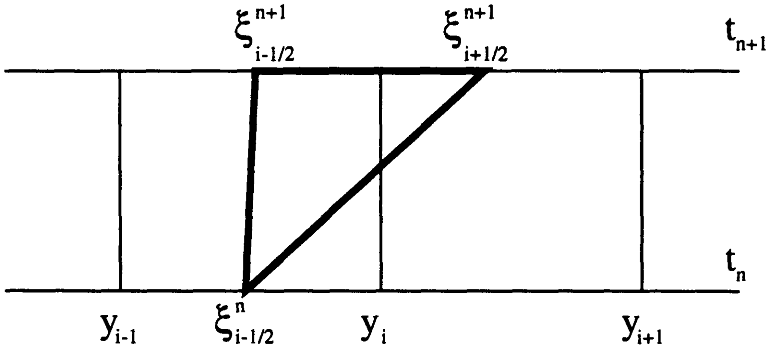

Figure 3-9: Grid regularization. Node moves to neighboring right box, new node generated. Triangular elementary region.

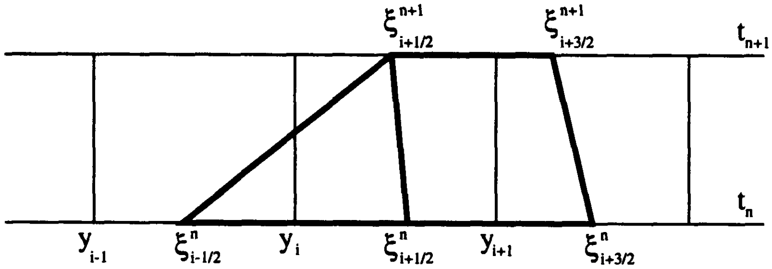

Figure 3-10: Grid regularization. Two node collision with left node crossing the box border

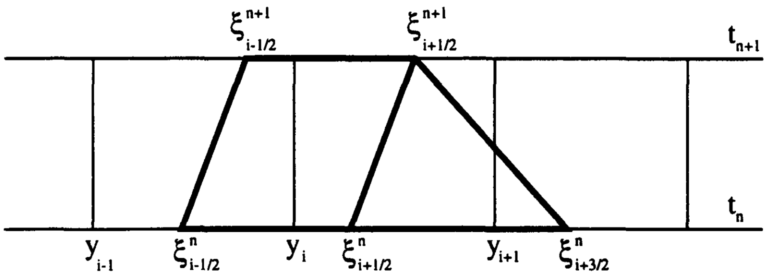

Figure 3-11: Grid regularization. Two node collision with right node crossing the box border

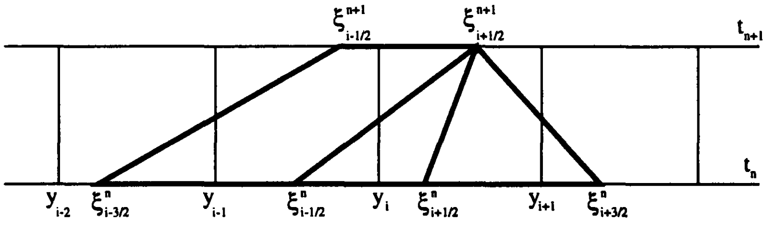

Figure 3-12: Grid regularization. Three node collision.

3.3 Convolution Term Treatment

To complete the description of "splitting" algorithm discussed in Section 3.1 we need to implement an algorithm for time integration of the following equation

$$u_t + \int_0^{2\pi} K(x-y)u(y)dy = 0\,. \tag{3.63}$$

In order to preserve second order of accuracy for the overall scheme, an algorithm for integrating (3.63) must also be of the second order. We use a simple explicit scheme based on second-order Runge-Kutta method (see [8, 21] for reference).

In the case of a "single mode" kernel (2.20) space integral in (3.63) becomes particularly simple.

$$\begin{aligned} u_t &= -\int_0^{2\pi} \sin(x-y)u(y)dy = \\ &- \sin x \int_0^{2\pi} \cos(y)u(y)dy + \cos x \int_0^{2\pi} \sin(y)u(y)dy\,. \end{aligned} \tag{3.64}$$

Integrals in the last expression can be easily computed using the rectangle rule.

Integration of (3.63) is done in two sweeps. In the first sweep we find auxiliary values of u at $t = t_n + \Delta t/2$:

$$u_j^* = u_j^n + \frac{\Delta t}{2}(I_1 \sin(x_j^n) + I_2 \cos(x_j^n)), \tag{3.65}$$

where

$$I_1 = -\sum_{j=1}^{N} u_j^n \cos(x_j^n)(\xi_{j+\frac{1}{2}}^n - \xi_{j-\frac{1}{2}}^n)\,, \tag{3.66}$$

$$I_2 = \sum_{j=1}^{N} u_j^n \sin(x_j^n)(\xi_{j+\frac{1}{2}}^n - \xi_{j-\frac{1}{2}}^n)\,, \tag{3.67}$$

$$x_j^n = \frac{1}{2}(\xi_{j-\frac{1}{2}}^n + \xi_{j+\frac{1}{2}}^n)\,. \tag{3.68}$$

(see Figure 3.2.4). In the second sweep we compute values of u on the $(n+1)$–st time level

$$u_j^{n+1} = u_j^n + \frac{\Delta t}{2}(I_1^* \sin(x_j^n) + I_2^* \cos(x_j^n))\,, \tag{3.69}$$

where I_1^* and I_2^* are computed as in (3.66) using u_j^* in place of u_j^n.

Remark 3.3.1 *Spectral method could be another possible choice for integration of (3.63). In general, with "multi-mode" kernel (2.19) it becomes superior to our scheme. In that case computation of the space integral in (3.63) will require* $O(N^2)$ *operations where* N *is the number of grid points and will become rather costly numerically. The spectral method, however, will need only* $O(N\log(N))$ *operations. We do not use the spectral with "single sine" kernel since it*

1) is restricted for $N = 2^m$*;*

2) is nontrivial to implement on a moving grid;

3) provides low accuracy for discontinuous solutions.

Chapter 4

Long-Time Integration Experiments.

4.1 Poincaré Sections.

In this section we introduce some tools that will be useful in the analysis of the numerical calculations results. Specifically: we introduce special versions of the Poincaré map technique, adapted to our infinite dimensional situation. In particular, in Remark 4.1.2 we point out a special property that characterizes traveling waves.

4.1.1 Some definitions.

Equation (2.18) describes a time evolution in the space of 2π–periodic functions $u(x,t)$. We can use the Fourier components of the solution as a set of convenient coordinates

$$u(x,t) = \sum_{k=-\infty}^{\infty} F_k(t)e^{ikx}, \tag{4.1}$$

where $F^*_{-k} = F_k$ and F_0 is absent[1], since u is real valued and has zero mean. Then the time evolution of u can be represented by an infinite system of ordinary differential equations for the set of Fourier modes $F_k(t)$. The nonlinearity in (2.18) introduces mode coupling into the system while the linear

---

[1] The time evolution keeps F_0 constant. It is thus consistent to take it identically zero.

integral term (with the kernel (2.20)) affects only the equations for the first modes $k = \pm 1$:

$$\frac{d}{dt}F_k(t) = -\frac{ik}{2}\sum_{m+n=k} F_m(t)F_n(t) \quad \text{for} \quad k = \pm 2, \pm 3, \dots, \tag{4.2}$$

$$\frac{d}{dt}F_1(t) = i\pi F_1(t) - \frac{i}{2}\sum_{m+n=1} F_m(t)F_n(t), \tag{4.3}$$

$$\frac{d}{dt}F_{-1}(t) = -i\pi F_{-1}(t) + \frac{i}{2}\sum_{m+n=-1} F_m(t)F_n(t). \tag{4.4}$$

Fourier space thus becomes a natural representation for the *phase space* of the system defined by (2.18). The set of equations above gives another perspective on equation (2.18), from the *Dynamical Systems* point of view, rather than the *Nonlinear Waves* one. We can formally consider these equations as an infinite–dimensional nonlinear system with phase space coordinates $F_k(t)$, $k = \pm 1, \pm 2, \dots, \infty$. In fact, equation (2.18) has a Hamiltonian structure — as long as its solutions do not produce strong discontinuities (See Subsection A.2 in the Appendix, where we show this.[2])

Remark 4.1.1 *We stress here that we* **do not use** *the form of the equations above in (4.1)-(4.4) for our* **numerical calculations.** *This form is introduced for purely theoretical purposes in the interpretation and analysis of the numerical results, as explained in this section.*

One of the most useful techniques for analyzing low-dimensional trajectories (such as, for example, periodic and two-frequency quasiperiodic orbits) in multi-dimensional spaces is the use of **Poincaré sections**. We will adapt this method to identify and analyze low-dimensional solutions of (2.18) — equivalently, of (4.2)-(4.4) — obtained numerically.

By analogy with finite-dimensional dynamical systems (e.g., see [12]) we introduce the **Poincaré map induced by the $\mathbf{k^{th}}$ Fourier mode**. As in the finite-dimensional case, this Poincaré map is defined for each trajectory by its **first return to the hyperplane** $\text{Im}(F_k) = 0$. Since the trajectories may cross this plane from the side of positive values of $\text{Im}(F_k)$ to the side of negative ones, as well as the reverse, we further restrict the intersections to those which correspond to the **direction of increasing** $\text{Im}(F_k)$. That is

$$\text{Im}(F_k) = 0 \qquad \text{and} \qquad \text{Im}\left(\frac{d}{dt}F_k\right) > 0. \tag{4.5}$$

This corresponds to looking at the solution after the point $F_k(t)$ has gone exactly once around the origin in the complex plane.[3]

---

[2] We also show there that the real and imaginary parts of the F_k's are a canonical conjugate set of variables: see equation (A.6).

[3] We note that, in the numerical calculations, the modes actually do "orbit" around the origin (in each of their corresponding planes) and never get too close to it. Thus, this is a useful definition.

Continuing with the finite-dimensional case analogy, we also introduce the **$\mathbf{n^{th}}$ iterate of the Poincaré map** as the n^{th} return of the trajectory to the hyperplane defined by (4.5). Finally, we define the **Poincaré section induced by the $\mathbf{k^{th}}$ Fourier mode** (or simply the **Poincaré section**) as the **set of all the iterates of a point by the Poincaré map**. This way, each trajectory corresponds to the infinite sequence of points in a Poincaré section. Each point on the section corresponds to a single return of the trajectory to the hyperplane, as in (4.5).

To facilitate the visualization of an (infinite dimensional) Poincaré section, we introduce the set of **projections of a Poincaré map**. The m^{th} projection is given by the image of the Poincaré section induced by the k^{th} mode on the m^{th} complex plane given by

$$F_m = 0 \qquad \text{for:} \quad m \neq k\,. \tag{4.6}$$

That is: **the m^{th} projection of a trajectory by the k^{th} Poincaré map,** is the set of positions F_m takes on its complex plane, recorded at the moments when F_k returns to the k^{th} hyperplane, as in (4.5).

4.1.2 Traveling waves on a Poincaré Section.

In the previous subsection we introduced the Poincaré map and Poincaré section induced by a Fourier mode, and the projections induced by the other modes. Here we **illustrate these notions with the example of a solution periodic in time.** To be more specific: the traveling waves,[4] introduced in (2.21) of Section 2.2. We will choose $F_1(t)$ as the base mode giving the Poincaré map (that is, F_1 is the variable that sets the "clock", with $k = 1$ in (4.5)). This particular choice of the base mode is the one we will use for most of the examples throughout the rest of this chapter.

Because of the traveling wave character of these solutions and the fact that u in equation (2.21) is an **even** function of the variable $x - st + \phi_0 - \frac{\pi}{2}$, it is clear that their Fourier series (as in (4.1)) has the form

$$u(x,t) = \sum_{k=-\infty}^{\infty} \left(a_k e^{-ik(st-\phi_0+\frac{\pi}{2})}\right) e^{ikx}\,, \tag{4.7}$$

where the **coefficients a_k are real**. Thus the Fourier modes $F_k(t) = a_k e^{-ik(st-\phi_0+\frac{\pi}{2})}$ are "synchronized". That is, the k^{th} mode travels around the origin in its complex plane (tracing a circle) at a constant velocity which is k times that of the first mode. Furthermore, when the first mode is real valued,[5] all the others are real too. Thus each **traveling wave (2.21) is represented by a single point**

---

[4] **Actually, the only examples of time periodic solutions of equation (2.18) known to us.**

[5] **That is: $st - \phi_0 + \frac{\pi}{2}$ is a multiple of π.**

on the Poincaré section induced by the first Fourier mode. Moreover, such a point lies on the real axis in each projection plane of the Poincaré section.

Remark 4.1.2 *More generally, it is clear that the Poincaré section (as induced by* any *of the Fourier modes) of any time periodic solution will consist of a finite number of points.*[6] *Furthermore, the argument above shows that the Poincaré section of any traveling wave solution (which is automatically periodic in time) by the first mode must be a single point, whether or not the solution has any additional symmetry (like being even). This last* property makes it easy to detect small deviations from the traveling wave structure, *while just looking at graphs of the $u(x,t)$ profiles can be confusing.*

4.2 Numerical Experiments.

In this section we report some of the results of our numerical experiments. For our numerical computations we used a second order fractional step approach (Strang splitting, [23]) described in Chapter 3.

The existence of non–breaking solutions for equations like (2.18) — in the form of traveling waves — has been established both numerically and analytically (see [9], [19] and [20]). However, this prior work leaves open the question: **Are the traveling waves the only possible never–breaking solutions of (2.18), or are there others?** The fact that equation (2.18) is (in some sense) a Hamiltonian system — as explained in subsection A.2 of the Appendix — suggests that one should, perhaps, be not too surprised if other such solutions exist.

We conducted extensive numerical experiments on (2.18). These calculations gave evidence for the existence of other never–breaking solutions. As it turns out, these solutions are not merely stable, but they appear to be **attractors** for "general" solutions arising from "arbitrary" initial data (in the sense to be described below.) In all the experiments performed we started with 2π–periodic functions of various shapes, and used them as initial conditions for (2.18). The long term behavior of the solutions generated by these initial conditions was then explored. Both the Poincaré sections techniques introduced in Section 4.1 and other visualization methods, to be explained below, were used to investigate the solutions.

4.2.1 Evolution Stages for General Initial Conditions.

The numerical experiments we conducted for (2.18) with the kernel (2.20) demonstrate that, for almost all initial conditions (see Remark 4.2.1 below) the solutions evolve according to the following scenario:

---

[6] Since the period must be a multiple of the time it takes the mode to go around the complex origin once.

1. TRANSIENT STAGE. SHOCKS PRESENT. ENERGY DECAYS.

   Shortly after the evolution begins the wave profiles steepen and **shocks** appear, very much in the same way as what happens for the solutions of the inviscid Burgers equation. These shocks dissipate the energy (2.23) (as shown in Subsection A.3 of the Appendix) and become weaker as time passes. After some period of time[7] the shocks weaken so much that they can be, effectively, ignored.[8] An example of this type of evolution is shown in Figure 4-1.

2. LIMITING STAGE. CONSTANT ENERGY.

   After the shocks disappear from the solution[9] the evolution becomes conservative (see Appendix A). All the experiments we have conducted suggest that no more shocks are formed at this final stage — even though the solution remains highly nontrivial, so that pressure variations are still present. Thus the energy is preserved. We will call solutions obtained by this "transition" mechanism the **limiting solutions** and will focus on analyzing their nature.

In other words, as $t \to \infty$ the shocks vanish and a limiting solution **without shocks** is attained. This **limiting solution has, typically, highly nontrivial structure.**

Remark 4.2.1 *In fact, it appears that the only case when the initial conditions do not lead to the formation of non-trivial, non-breaking (and therefore constant energy), limiting configurations is when the initial conditions are* non–resonant *with the kernel of the integral operator in equation (2.18). If this non-resonance occurs, then the integral term does not contribute to the evolution and the energy of the solutions decays, asymptotically reaching zero in exactly the same way as the solutions to the inviscid Burgers equation. This set is constituted by those initial conditions that do not have any of the Fourier components in K, nor their sub-harmonics (since the nonlinear terms will generate the harmonics of any component in the initial conditions). Thus, it is a rather thin set. As an example, consider the following initial condition*

$$u(x,0) = \sin(mx), \qquad \textit{for } m > 1, \tag{4.8}$$

for the case when (2.20) applies. Then, in the system (4.2)-(4.4), only the harmonics F_n with $n = k \cdot m$ will be excited. The first Fourier modes $F_{\pm 1}$ (necessary for the resonance to occur) therefore never get excited and the solution simply "ignores" the integral term in (2.18).

4.2.2 Structure of the Attracting Solutions.

The numerical experiments show that different initial conditions in general converge to different limiting solutions. These limiting solutions, however, share many common features and can be

---

[7] Usually less than a hundred of iterates of Poincaré map, see Appendix D for details.

[8] In the numerical calculations the shocks become too weak and cannot be detected.

[9] Technically, our code imposes a certain small threshold which determines the weakest detectable shock.

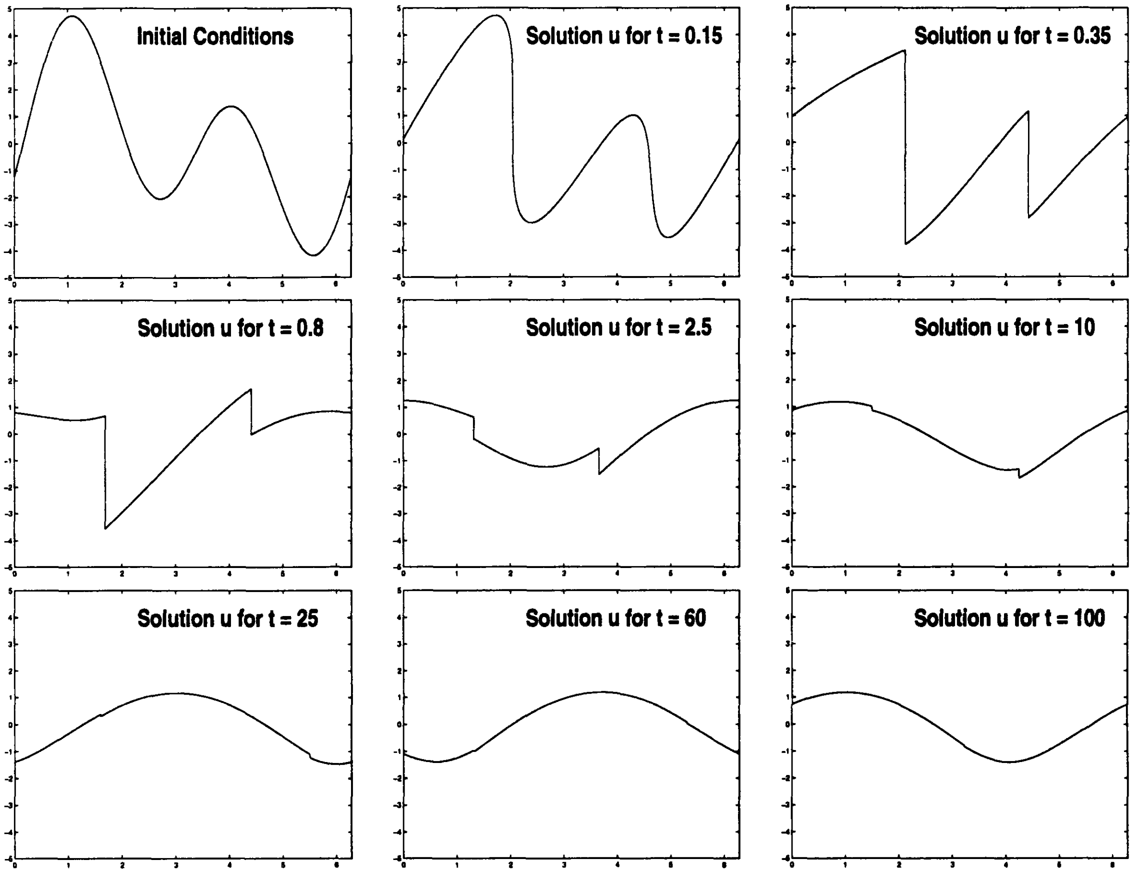

Figure 4-1: Evolution illustrating the transient states, starting from a typical initial condition $u(x,0) = 2\sin x + 3\cos(2x - 2)$. From left to right and top to bottom we have: the initial conditions and the solution $u(x,t)$ at the times $t = 0.15$, 0.35, 0.8, 2.5, 10, 25, 60, 100. The vertical and horizontal scales are $-5 < u < 5$ and $0 < x < 2\pi$, respectively. The shocks first form sometime for $0.15 < t < 0.35$. Initially they grow, as the nonlinearity continues to steepen the solution. But, by $t = 0.8$ they are decaying in strength and by $t = 10$ they are quite weak. The shocks have essentially disappeared by $t = 60$. From then on energy is conserved and no new shocks appear, even though the solution still has a substantial acoustic wave amplitude. *Note that a Poincaré cycle is* $\Delta t \approx 0.05$.

treated as elements of one family.

When the energy (2.23) of the initial conditions is sufficiently large (see Remark 4.2.2), the solutions converge to a maximum amplitude traveling wave ((2.21) with $\delta = 1$)

$$u = s(1) + b(1)\sqrt{1 - \sin(x - s(1)t + \phi_0)}\,, \tag{4.9}$$

for some phase shift ϕ_0, with s and b given by (2.22).

When the energy of the initial conditions is not sufficiently large, we obtain an entirely different class of limiting solutions — which almost look like traveling waves but not quite, as a perturbation of oscillatory nature is superimposed on them. To be more specific, these limiting solutions all have the following typical structure (illustrated in Figures 4-2 and 4-3)

- The gross structure of the solution can be described as being that of a smooth periodic traveling wave, with a single oscillation per wavelength.[10] But the shape of the wave undergoes periodic changes as it moves, described next.
- Each cycle starts with the development of a single corner on the front part of the wave, not too far from the trough. The corner then moves along the wave profile to the back side, where it disappears (at a position roughly symmetrical — relative to the minimum of the wave profile — with the one where it appeared).
- A period of smooth behavior follows the corner "episode", and then the cycle starts again. See Remark 4.2.3 for more details.

Notice that, unlike the case of the traveling waves (described in Section 2.2), which are either smooth or have a corner singularity for all times, these new solutions (a typical representative of which is shown on Figure 4-2) combine both behaviors, with sharp spikes during the time intervals when the corner singularities appear and smooth behavior the rest of the time. It is noteworthy that, even though these solutions are **not smooth**, they never break. Therefore they are exactly of the type we are interested in.

One can clearly see a repetitive pattern (on Figure 4-2) in the behavior of these new limiting solutions. As far as we can tell from our numerical experiments, the shape oscillations in the wave are periodic in time. Because this shape oscillation period is combined with the period arising from the translation of the overall wave shape, generally we see that these solutions will be **quasiperiodic in time** — except, of course, if the two periods are rationally related.[11]

To summarize, the most important outcomes of our experiments are the following

---

[10] Very similar to the traveling waves described in Section 2.2.

[11] Unfortunately, this property is especially difficult to determine numerically. However, we can tell that, if rationally related, the ratio is generally not simple.

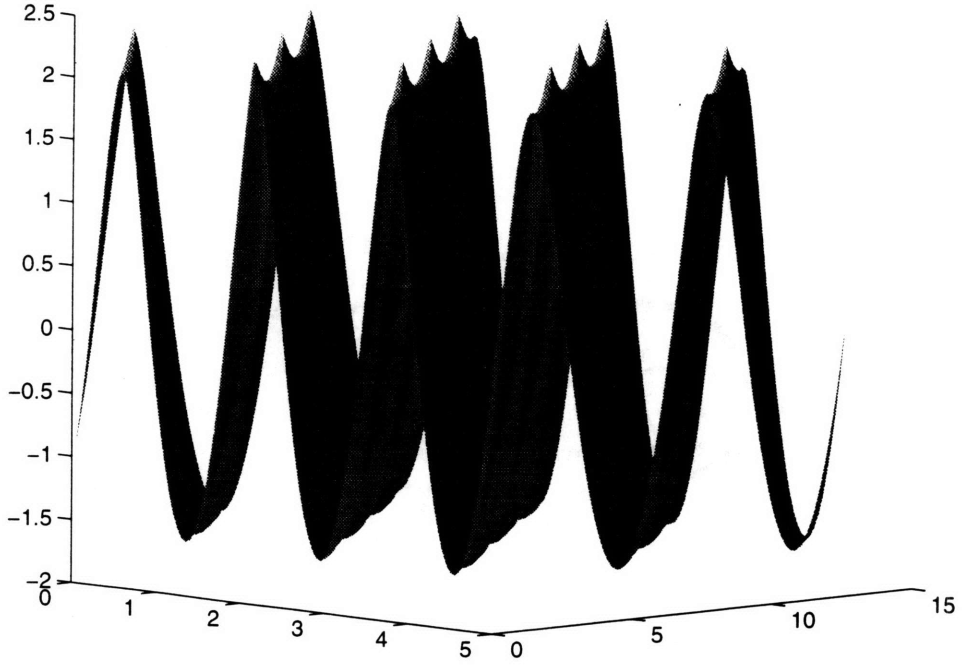

Figure 4-2: Typical attracting solution in physical space-time, plotted in the range $0 < x < 2\pi$ and $0 < t < 15$. Notice the periodic shape changes — the spikes in the profile, produced by the corners moving over the bottom of the wave (we have plotted the negative of the solution to make this more evident).

- Only two different types of limiting solutions appear to exist and be attracting, namely:
  - A maximum amplitude traveling wave (4.9), as shown on Figure 2-1;
  - A family of quasiperiodic solutions, such as the one shown on Figure 4-2.
- The energy (2.23) of the quasiperiodic solutions (which is a constant in time, as they have no shocks) is bounded by the energy of (4.9). It can take any value from this maximum to zero, depending on the initial conditions generating the solutions.
- The smooth traveling waves ((2.21) for $|\delta| < 1$) are neutrally stable and do not attract solutions.

We will elaborate more on the last two points here in what follows. It is remarkable that **all** the attracting solutions have corners.

Remark 4.2.2 *It is difficult to give a precise characterization of which initial conditions lead to which limiting wave. Clearly, the value of the initial energy is a crucial parameter, as the limiting solution cannot have an energy that exceeds this one. However, it is obviously not the only important parameter. The shape of the initial condition determines the strength of its resonance with the kernel* K*, which controls the amount of dispersion the solution will experience. Without resonance and dispersion (as in the case of (4.8) the limiting solution is always trivial (*$u \equiv 0$*). Therefore, the amount*

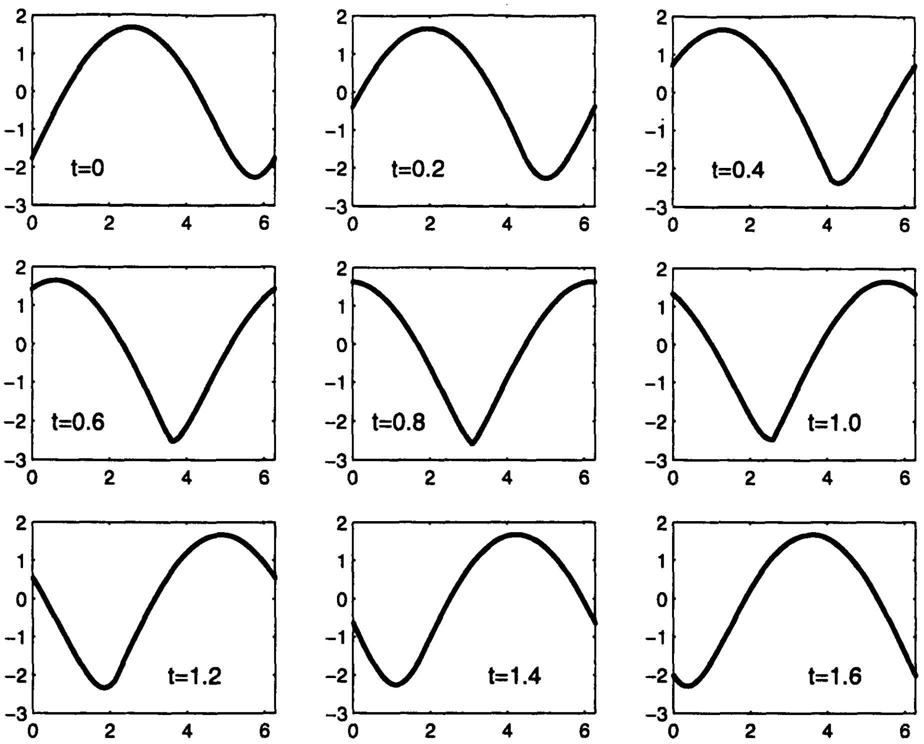

Figure 4-3: Typical evolution of a quasiperiodic attractor, illustrating the formation of a corner on the leading side of the trough of the wave, which then moves accros the bottom to the other side and disappears. Time here advances from left to right and top to bottom. The overall translation of the wave is from right to left, at a speed $s \approx -3.3$. This attractor followed from the initial conditions $u(x, 0) = 2\sin x$ — using a very fine mesh with 2000 points.

of energy left in the limiting solution will also depend (strongly) on the shape of the corresponding initial condition. But, for a given frozen shape, the amplitude (equivalently, the energy) will control the limit — and, if large enough, it will lead to the maximum amplitude traveling wave as the limit. Our prior loose use of "large energy" referring to the initial conditions leading to the formation of (4.9) and "small energy" to denote those leading to a quasiperiodic limit, was in this sense described here.

Remark 4.2.3 *As in the earlier discussion of the shocks vanishing from a solution during the transition phase of the evolution, it is* **difficult to tell numerically whether the corners actually disappear** *during the "smooth" part of the cycle illustrated by Figure 4-3 or just become too small to be detected by the numerical calculations. Thus, the attracting quasiperiodic solutions may not actually be smooth at any time, even though the numerical calculations seem to suggests this happens during some part of the cycle. We think this is, quite likely, the case.*

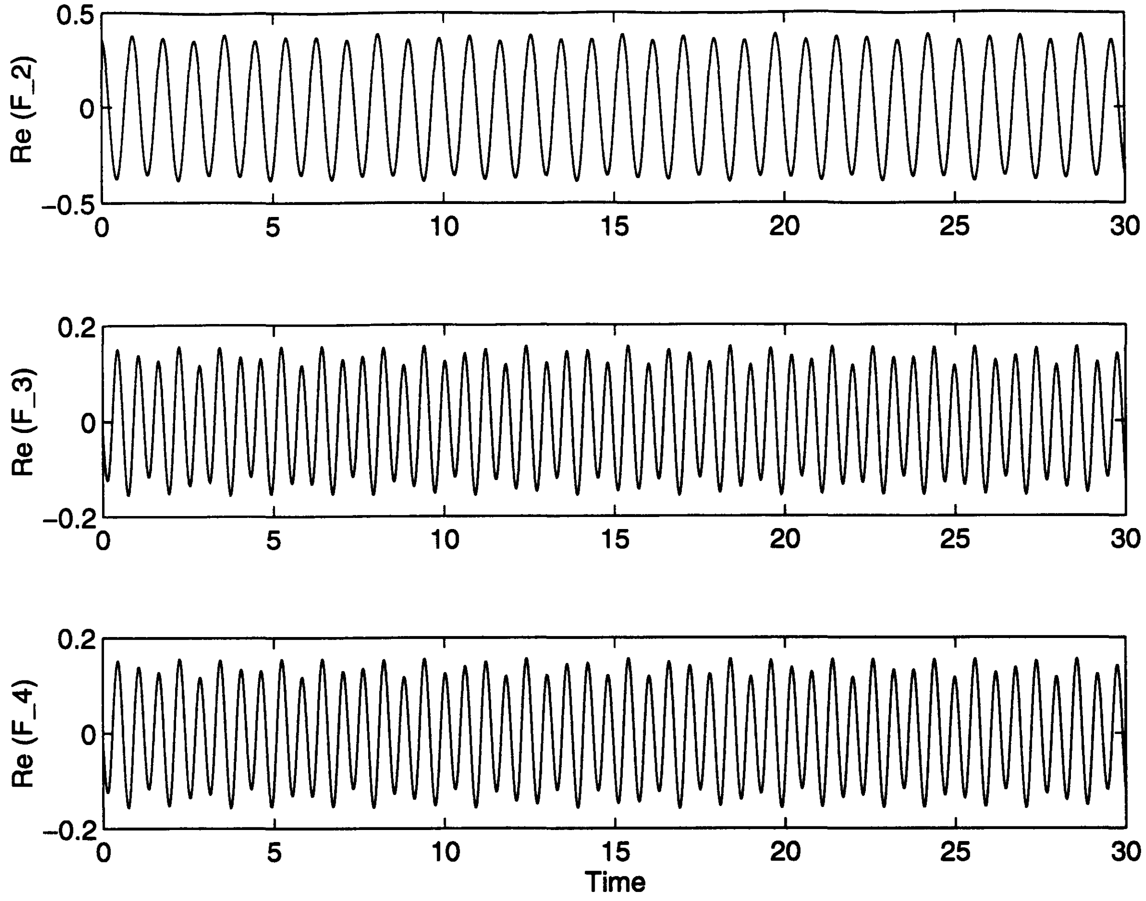

Figure 4-4: Real parts of the first three nonresonant Fourier modes for a typical attracting limiting solution, as functions of time.

4.2.3 Limiting Solutions in Fourier Space.

The periodic appearance of the corners in the general limiting solutions to (2.18) can be easily observed in physical space. Because of the periodicity with which this phenomenon occurs, we concluded that these solutions must be quasiperiodic in time. The phenomenon manifests itself also in Fourier space (and this gives us another way to look at the structure of the limiting solutions). The dependence of the Fourier modes F_k on time, for a typical attracting solution, is shown on Figure 4-4. We see that we can, in essence, describe them as high-frequency oscillations with superimposed low-frequency modulations in amplitude, of a much longer period.[12] Again we conclude that the solutions must be quasiperiodic with two periods. In fact, we conjecture that they can be written as 2π-periodic functions of two phases, as follows:

$$u = U^*(x - \omega_1 t, \omega_2 t)\,. \tag{4.10}$$

---

[12] Where the high-frequency is associated with the overall translational motion of the wave.

where ω_2 is substantially smaller than ω_1.

To say that these limiting solutions are two period quasiperiodic in time, is equivalent to stating that: in phase space the trajectories of their time evolution must lie on two dimensional torus. Of course, the phase space in this case is infinitely dimensional and a "numerical" graph of the solutions in it is quite impossible. On the other hand, we can plot "arbitrary" three dimensional projections of the trajectory. Then, if all of these give rise to two dimensional tori, then we can quite safely conclude that the full trajectory is a two dimensional torus. In fact, **this is exactly what we observe!**

As an illustration of the argument in the prior paragraph, we present here a few plots for an example limiting solution, using Fourier coefficients to parametrize the phase space — as shown in Appendix A, the Fourier coefficients provide a set of canonical coordinates. This solution was obtained by numerical integration of equation (2.18) with the initial condition

$$u(x,0) = 1.86\sin(x)\,. \tag{4.11}$$

We generate 3–D projections by picking arbitrary combinations of three functions of time from the real and imaginary parts of the Fourier coefficients of the solution.

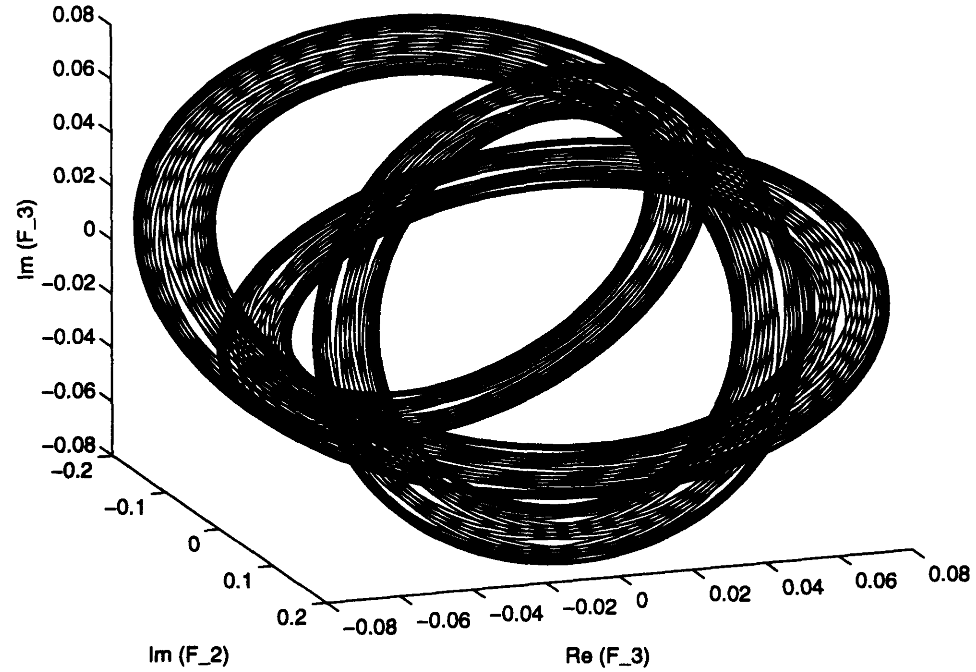

Figure 4-5: Trajectory in Fourier Phase Space corresponding to an attracting limiting solution. Projection on the three dimensional subspace (Im F_2, Re F_3, Im F_3). Notice that the trajectory traces a 2–D torus — the self–crossings are, of course, an artifact of the projection.

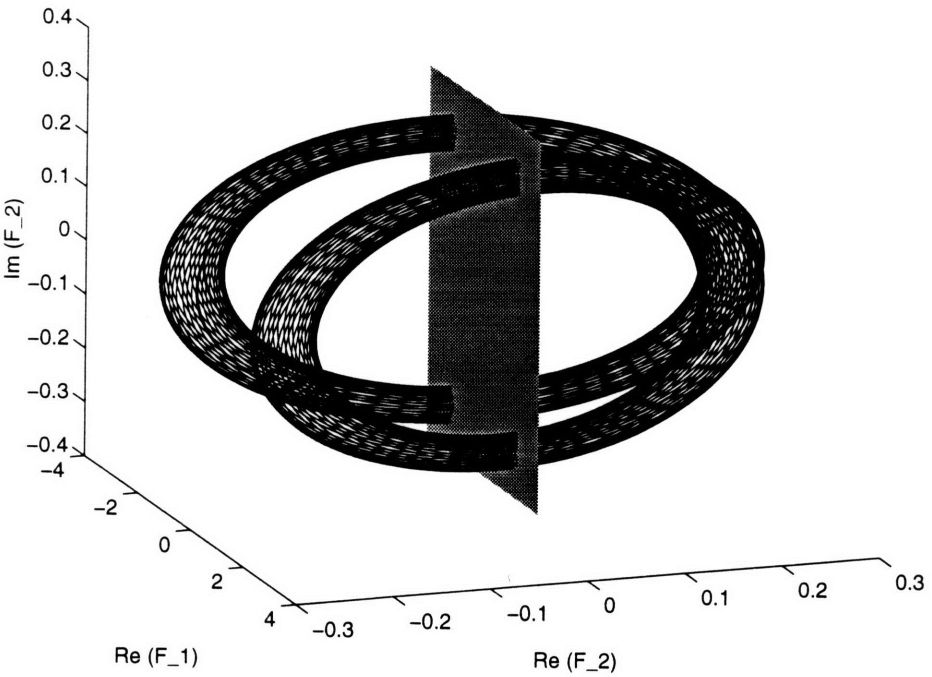

Figure 4-6: Trajectory in Fourier Phase Space corresponding to an attracting limiting solution. Projection on the three dimensional subspace (Re F_1, Re F_2, Im F_2) and the plane Re $F_2 = 0$ cutting the trajectory. The trajectory traces a 2–D torus.

The projections shown in Figure 4-5 and in Figure 4-6 are typical and clearly show two dimensional tori drawn by the trajectory. The actual trajectory, of course, does not intersect itself in phase space. The self–intersections of the tori in these figures are just an artifact of projecting an object immersed in a large dimensional space onto a low dimensional space. Finally, to confirm that the depth perception in these plots is not just an illusion, we show in Figure 4-7 the intersection of a plane (taken from within the three dimensional space in Figure 4-6) with the solution. As expected for the intersection of a torus with a plane, we find closed curves.

We point out that we explored many other three dimensional projections of various trajectories (corresponding to different limiting solutions). It is remarkable that: **in all the cases we found results similar to the ones described above,** with two dimensional tori. This allows us to argue that not only the projections, but the trajectories themselves must lie on two dimensional manifolds (in fact, tori). Indeed, it is extremely unlikely that an object visible as two dimensional on several of its three dimensional projections has dimension larger than two.

Remark 4.2.4 *The cross-sections considered above are almost equivalent to the projections of the Poincaré map introduced at the end of Section 4.1.1. The only difference is that the points on the Poincaré section induced by m-th mode must satisfy the condition Im* $(\frac{d}{dt}F_m) > 0$, *whereas on the cross-sections above both Im* $(\frac{d}{dt}F_m) > 0$ *and Im* $(\frac{d}{dt}F_m) > 0$ *are allowed.*

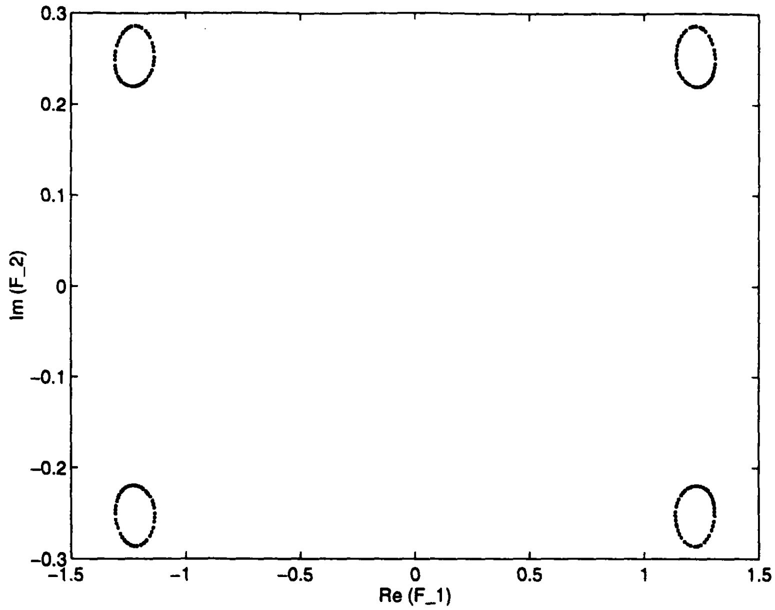

Figure 4-7: Cross-section of the phase space trajectory by the Re $F_2 = 0$ hyperplane and the projection on (Re F_1, Im F_2). This is the intersection of the plane shown in Figure 4-6 and the trajectory.

4.2.4 Poincaré Sections for the Attracting Solutions.

In this section we will give a description of the family of functions arising as attracting limiting solutions of (2.18) with (2.20), obtained via numerical simulation. These solutions appear as a stationary (in terms of energy) time evolution. We represent such functions by trajectories in phase space, parametrized by the Fourier modes $F_k(t)$. The results described above suggest that all the limiting solutions are at most two dimensional, so that the Poincaré sections technique should be applicable to the situation. Since both the phase space and the Poincaré sections are infinite dimensional, we will use the projections technique described in Section 4.1.

Our experiments show that the limiting solutions to (2.18) fill a very low dimensional special region in phase space. We first visualize this region by using the Poincaré map induced by the first Fourier mode $F_1(t)$ and projecting to the complex planes of F_2, F_3 and F_4. That is, we look at the values of F_2, F_3 and F_4 at the points along the trajectories where

$$\text{Im } F_1(t) = 0 \quad \text{and} \quad \text{Im } \frac{d}{dt} F_1(t) > 0 \, . \tag{4.12}$$

As pointed out in Remark 4.2.4, this approach is related to the one we used above in Section 4.2.3, but it will give us the freedom to study the structure of the set of solutions — as opposed to that of each single solution.

In Figures 4-8 through 4-14 we present Poincaré map studies for a few attracting limit solutions obtained as a result of the transition process described in Section 4.2.1. For these experiments we used initial data of fixed shape and varying amplitude, as follows

$$u(x,0) = A \cdot \sin x\,, \tag{4.13}$$

where A is a constant. We choose functions of this form for two main reasons: • it is relatively easy to control the "place" where the limiting solution lands in phase space by slowly varying the parameter A and • these functions exhibit maximum resonance with the kernel (2.20) in (2.18) and therefore optimally excite the dispersive mechanism (see Appendix B) leading to the formation of non-breaking structures. It is also worthwhile mentioning that in all the experiments[13] we conducted, we always observed limiting solutions of **exactly the same** type as the ones produced by (4.13). This leads us to believe that the simple subset of all the possible initial conditions given by (4.13), is sufficient to produce **all** the limiting solutions possible for (2.18).

In the figures, limiting attracting solutions are shown on the second, third and fourth projections of the Poincarè section induced by $F_1(t)$. Each closed contour on the plots, filled by the Poincarè map iterates, corresponds to a **separate solution** with the different value for the energy. Despite the very different patterns (see Remark 4.2.6) by which the Poincaré map iterates fill the curves, the most important features are the same for all of them.

In Figures 4-8 through 4-12 we present several examples of projections of the Poincaré sections for limiting solutions corresponding to different values of the amplitude A in (4.13). In all cases, clearly, the iterates fall on simple closed curves — reinforcing the conclusion that the solutions are quadiperiodic with two periods. We point out that the Poincaré sections induced by the higher modes (as opposed to F_1 here) have the same property and only differ by the larger complexity of the curves produced.

To illustrate the convergence to the limiting attracting solutions, in Figures 4-13 and 4-14 we have included all the points in the Poincareé sections (starting from the initial conditions) — instead of only plotting once the limit attracting solution has been reached. Thus, these Figures include points corresponding to the transient stage with shocks. It can be clearly seen from these plots, that **convergence occurs on a time scale of a few tens of iterates of the Poincaré map**. For a more detailed discussion of the convergence rates see Appendix D.

In Figure 4-15 we present[14] several of the limiting solutions together on the second projection of the Poincaré section induced by $F_1(t)$. The energy of these limiting solutions varies here from zero at the bottom of the picture (corresponding to the trivial solution, that yields just one point in the graph) to its maximum value at the top of the picture (corresponding to the maximum amplitude

---

[13] **With shapes for the initial condition other than the simple one in (4.13).**

[14] **Warning: This is a two-dimensional plot, in spite of the strong suggestion of depth it gives!**

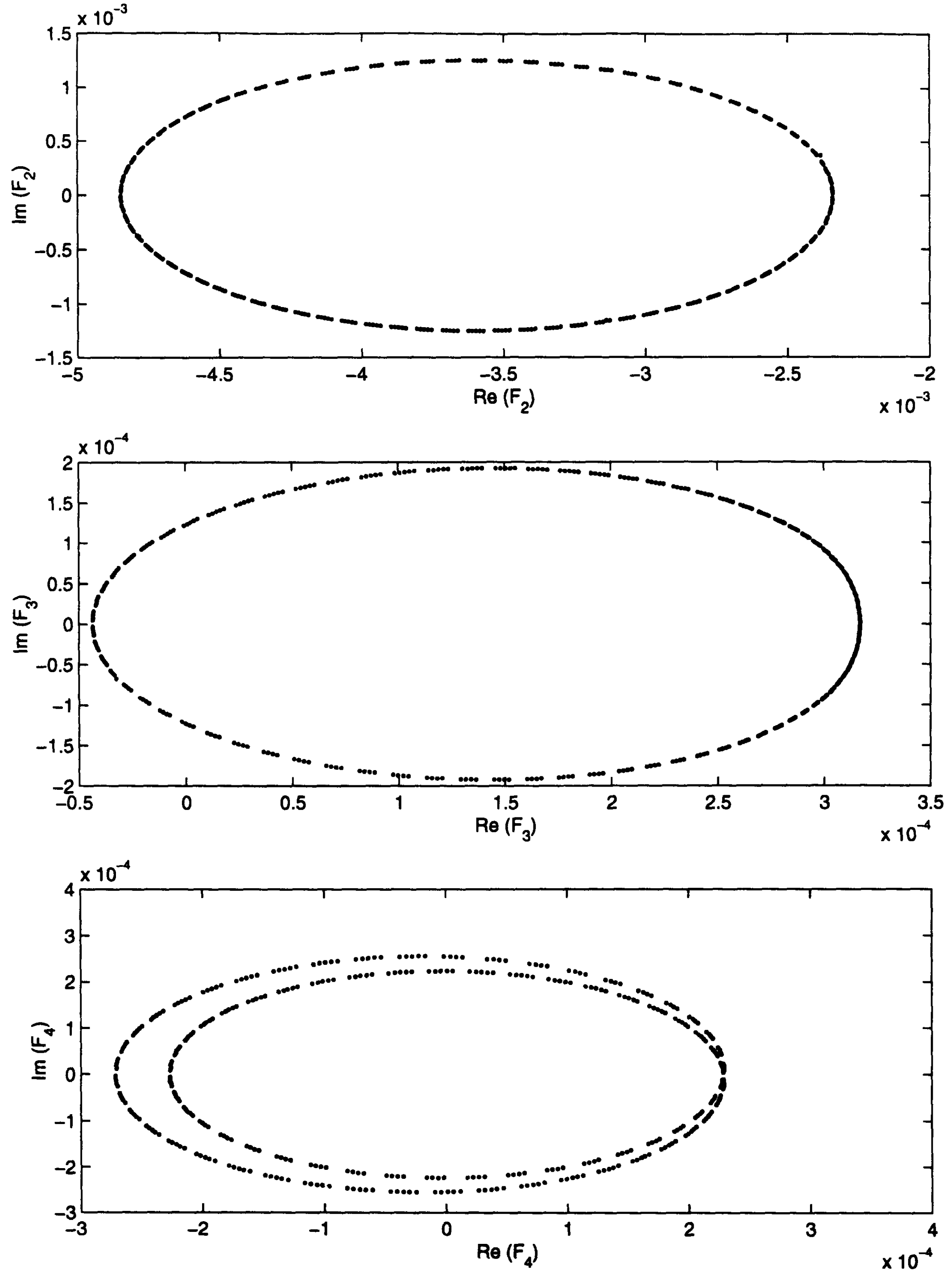

Figure 4-8: Second, third and fourth projections of the Poincaré section induced by $F_1(t)$. Limiting solution for the initial condition: $u(x,0) = 0.3 \sin x$. 400 map iterates plotted.

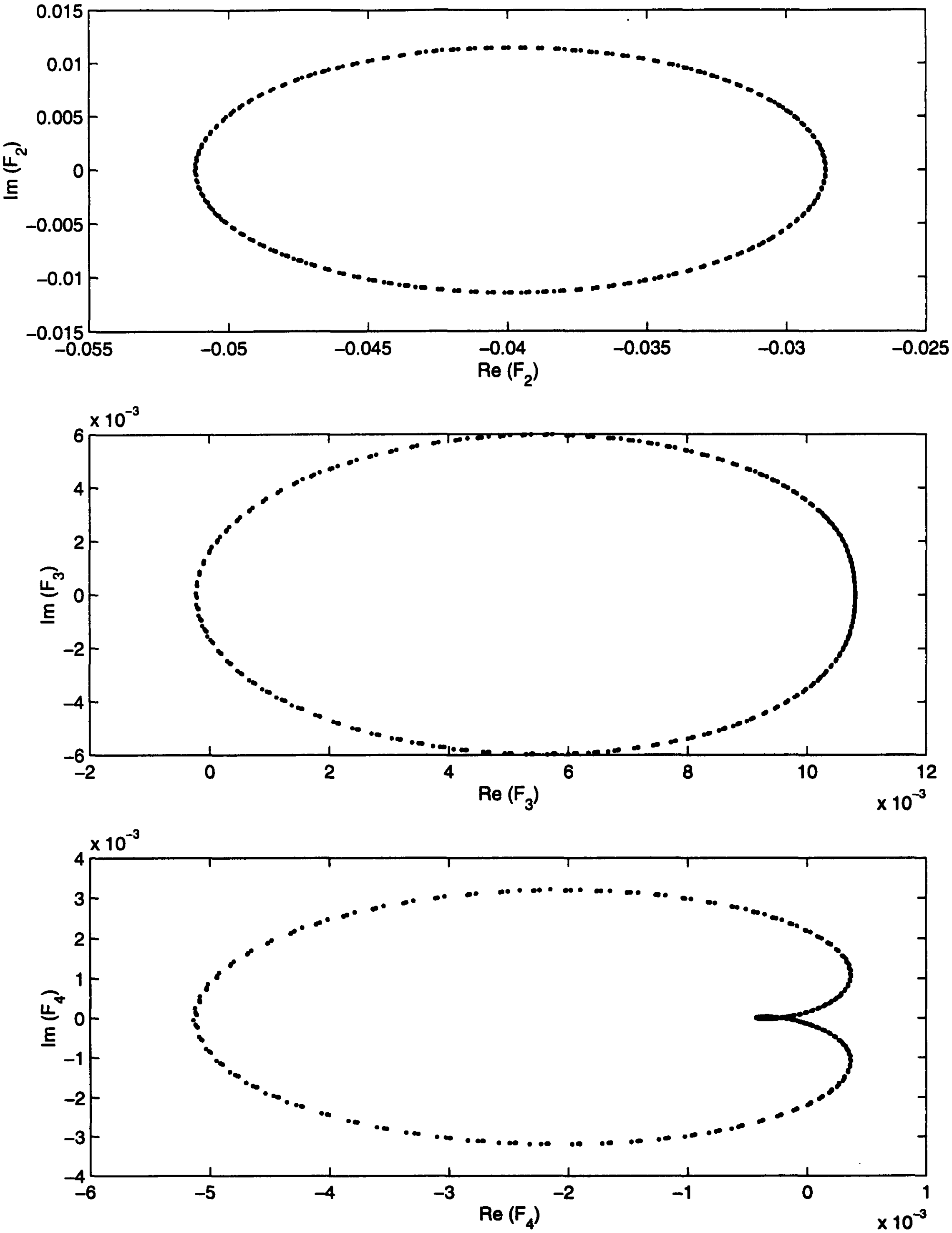

Figure 4-9: Second, third and fourth projections of the Poincaré section induced by $F_1(t)$. Limiting solution for the initial condition: $u(x,0) = 2\sin x$. 400 map iterates plotted.

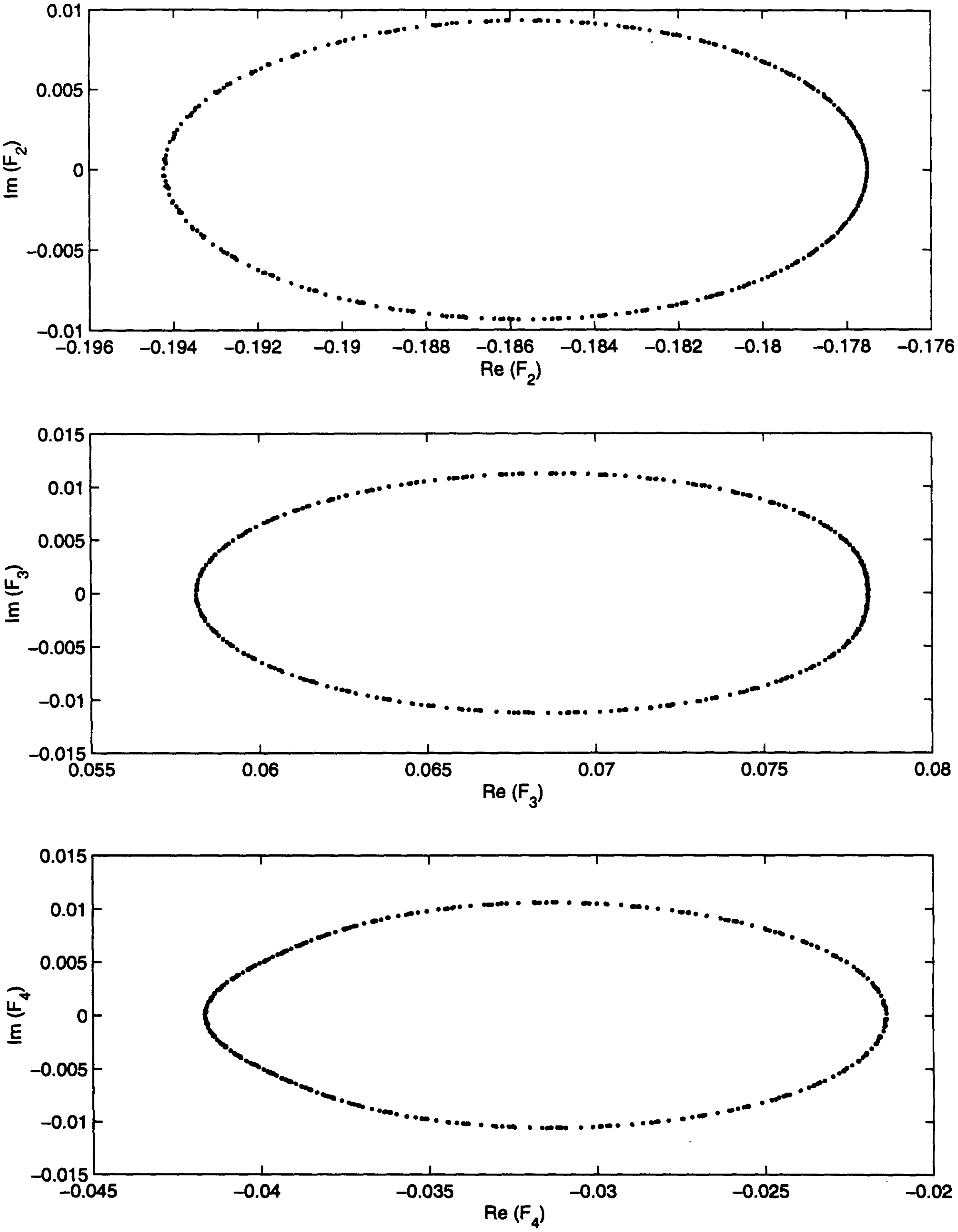

Figure 4-10: Second, third and fourth projections of the Poincaré section induced by $F_1(t)$. Limiting solution for the initial condition: $u(x,0) = 2.25 \sin x$. 400 map iterates plotted.

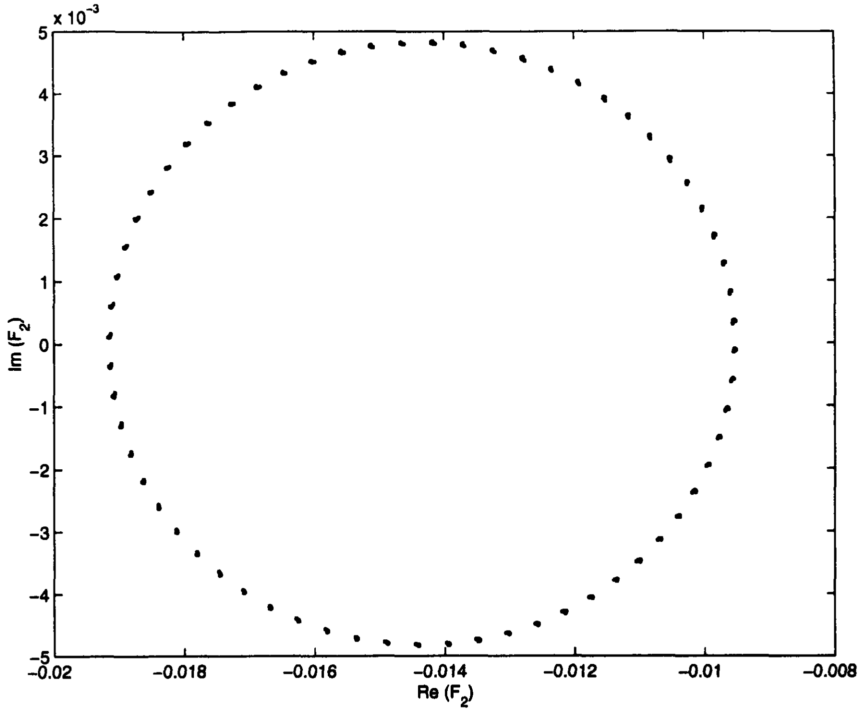

Figure 4-11: Second projection of the Poincaré section induced by $F_1(t)$. Limiting attracting solution for the initial condition: $u(x, 0) = 0.6 \sin x$. 400 map iterates plotted.

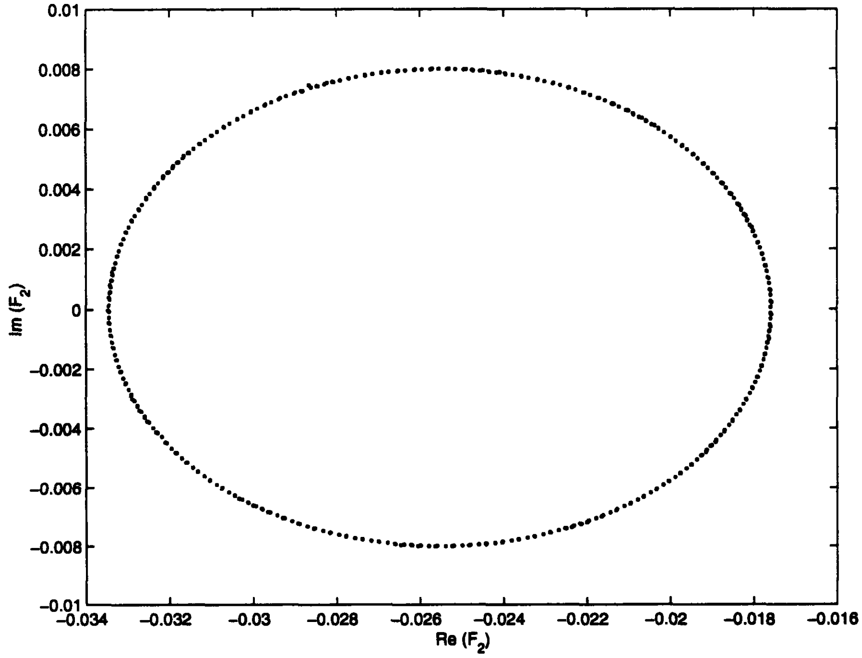

Figure 4-12: Second projection of the Poincaré section induced by $F_1(t)$. Limiting attracting solution for the initial condition: $u(x, 0) = 0.8 \sin x$. 400 map iterates plotted.

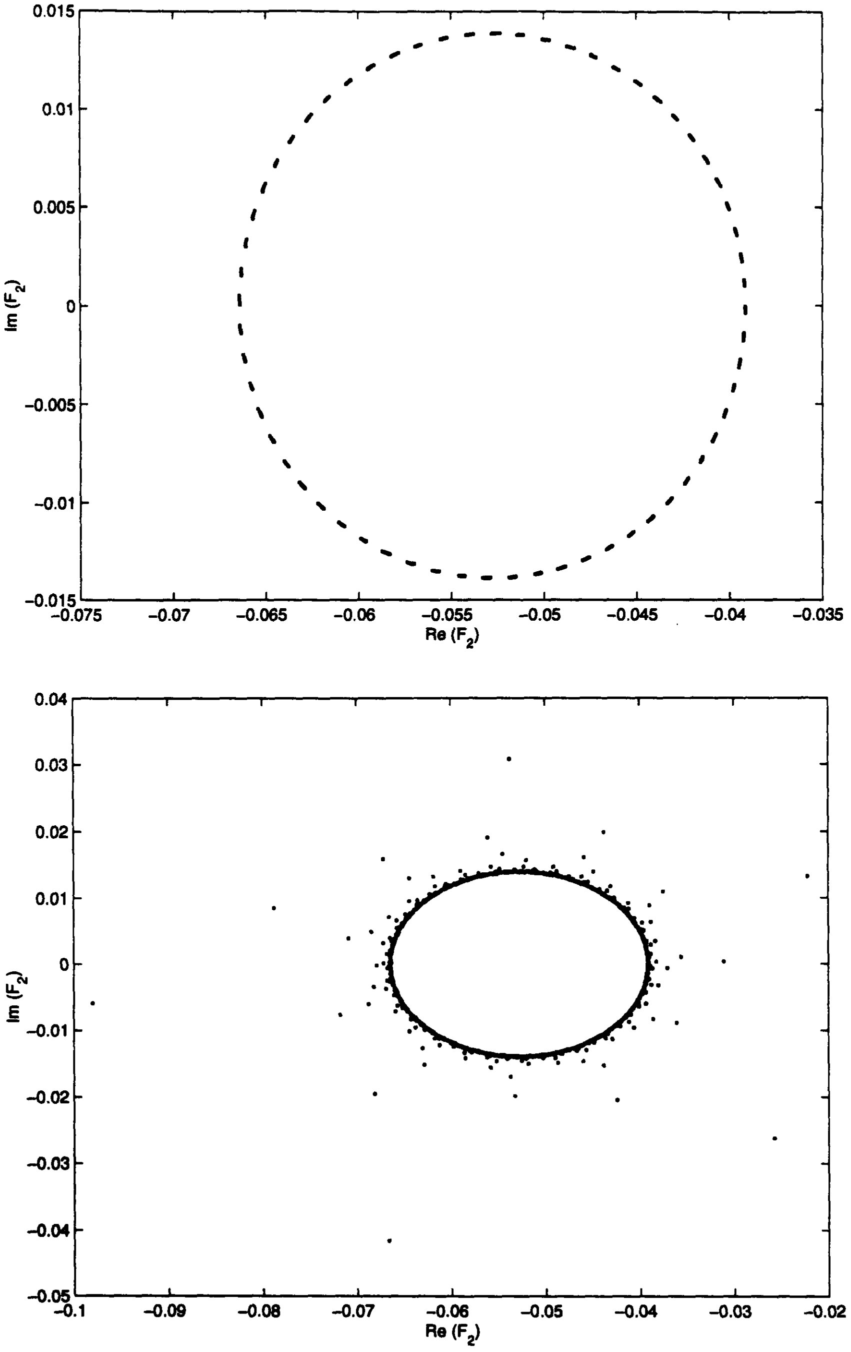

Figure 4-13: Second projection of the Poincaré section induced by $F_1(t)$ for the initial condition: $u(x, 0) = 1.15 \sin x$. The top graph shows 400 map iterates for the limiting solution. The bottom graph shows the first 1000 map iterates, starting from $t = 0$.

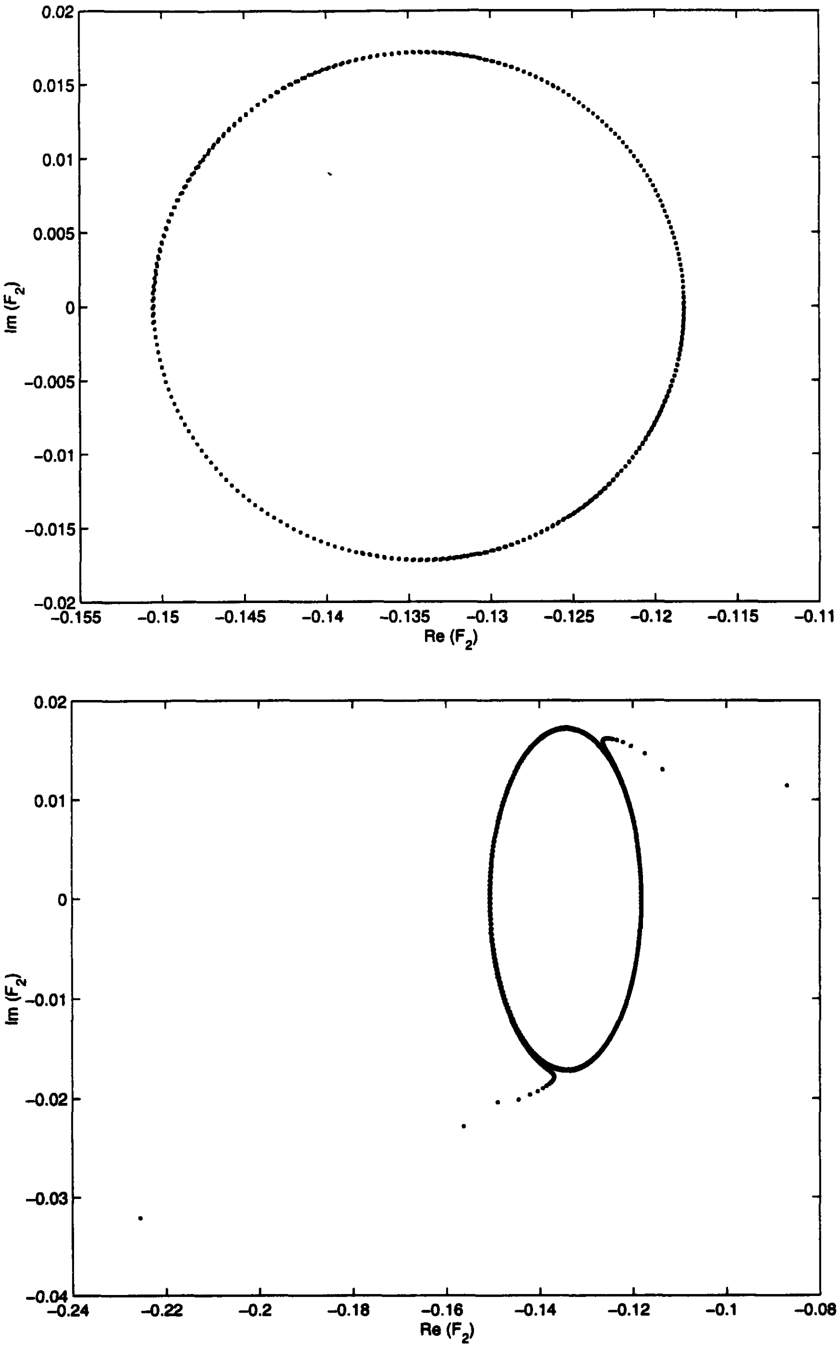

Figure 4-14: Second projection of the Poincaré section induced by $F_1(t)$ for the initial condition: $u(x,0) = 1.86 \sin x$. The top graph shows 400 map iterates for the limiting solution. The bottom graph shows the first 1000 map iterates, starting from $t = 0$.

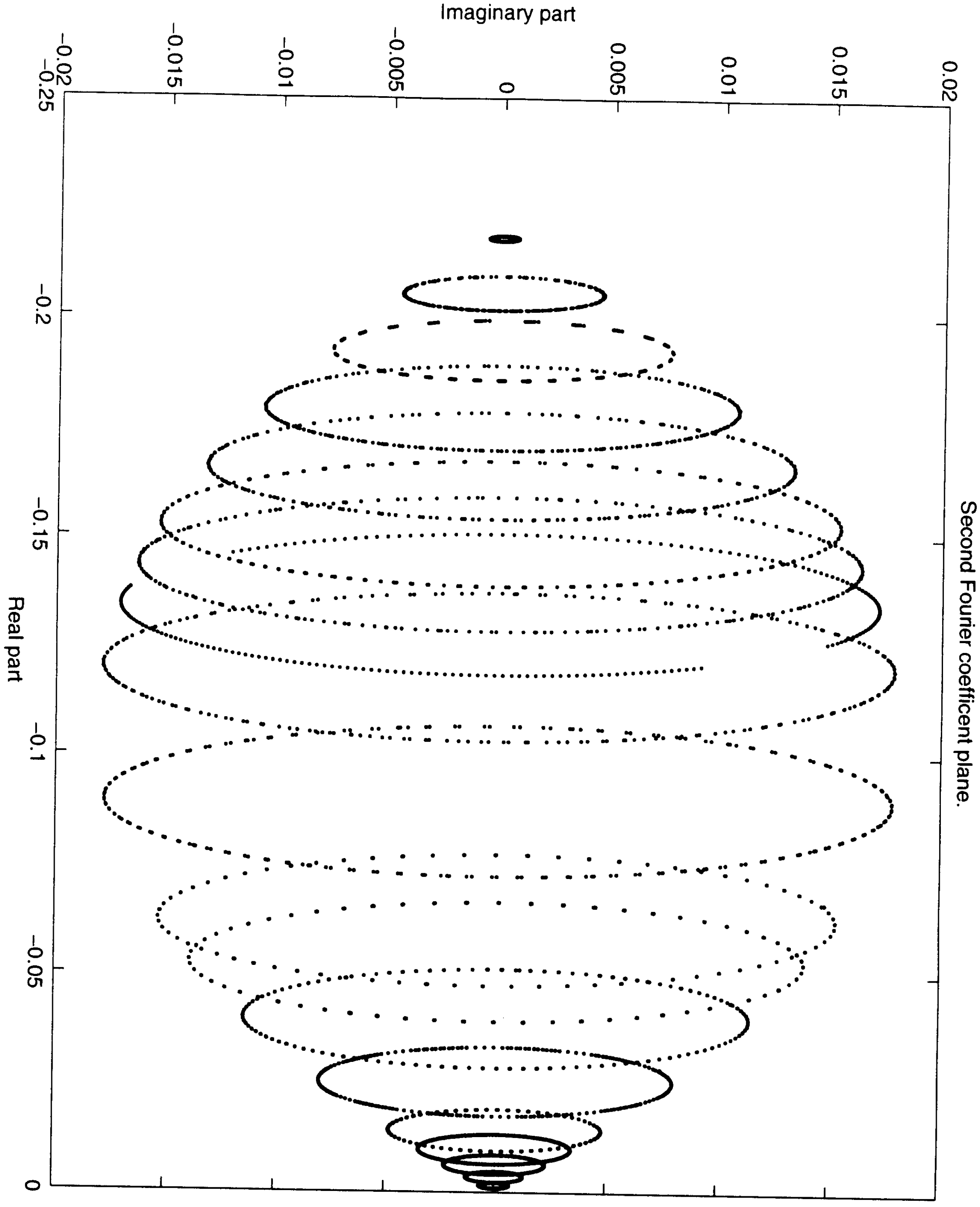

Figure 4-15: Projections on (Re F_2, Im F_2) of the Poincaré Sections generated by F_1 for various attracting limiting solutions as the initial conditions are varied.

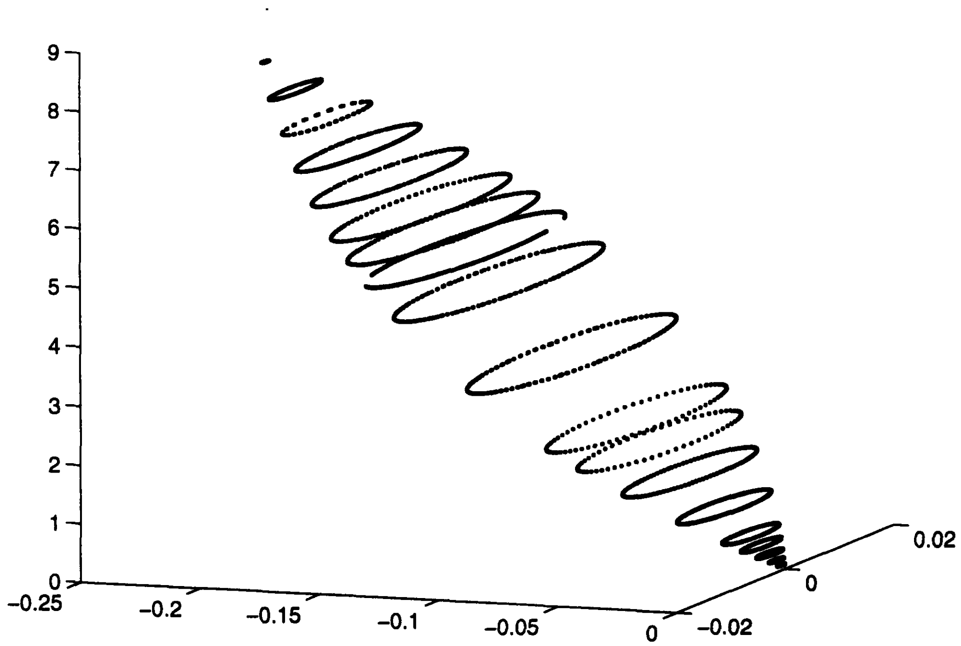

Figure 4-16: Projections on $(-0.25 < \text{Re } F_2 < 0, -0.02 < \text{Im } F_2 < 0.02)$, of the F_1-Poincaré Sections for various limiting solutions, sorted by their energy on the vertical axis.

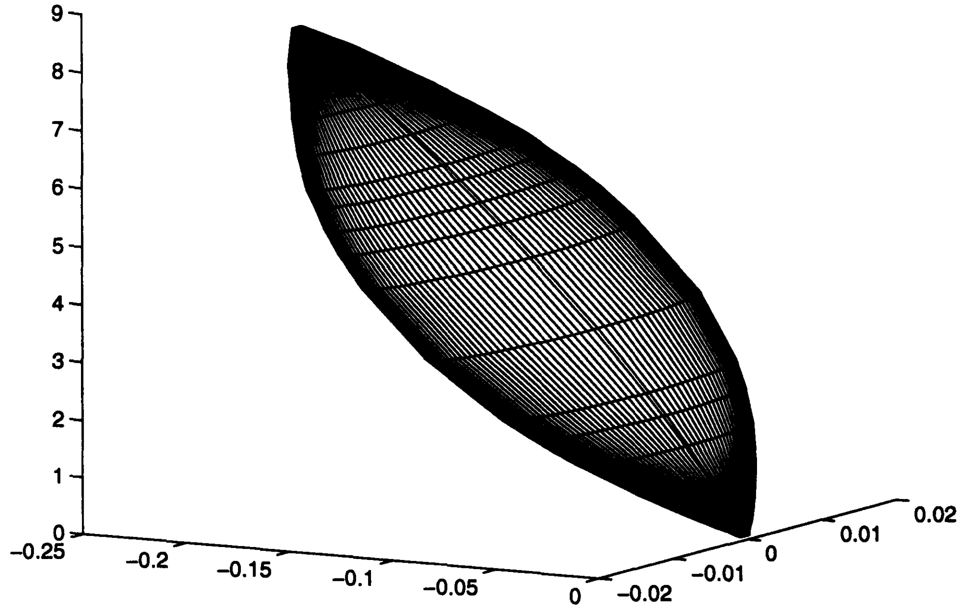

Figure 4-17: Surface of limiting solutions, produced by the projections on (Re F_2, Im F_2) of the F_1-Poincaré Sections for the solutions, sorted by their energy on the vertical axis.

traveling wave, which also yields just one point in the graph — as explained earlier). We thus use the energy as a parameter for this (one-parameter) family of curves. Figure 4-16 shows the same set of limiting solutions as Figure 4-15, but now the solutions are plotted in 3–D, with energy on the vertical axis. Note that the "centers" of the contours are ordered with respect to the energies. Those corresponding to solutions with larger energies are located to the left of those corresponding to solutions with smaller energies. Thus, the leftmost contour (which degenerates into a single point) represents the maximum energy limiting solution (4.9) and the rightmost contour (also collapsing into a point) corresponds to the trivial (zero energy) solution. The hierarchy of limiting solutions fills a peculiar sharp-ended bounded surface in the "projection" three dimensional space given by the second Fourier mode and energy, depicted in Figure 4-17. The two endpoints of this figure are related to the maximum energy solution (4.9) and the minimum energy trivial solution. If we add to this picture the single points that correspond to each of the traveling wave solutions (with all the possible amplitudes), they draw a curve running roughly at the center of the surface in Figure 4-17, and joining the two sharp end points! We will see later that, in fact, the whole interior of this surface can be filled by quasiperiodic in time solutions, with the ones "inside" being smooth and non-attracting (though stable).

Remark 4.2.5 *The trajectories of the limiting solutions we have been considering here have another interesting property. If one chooses the first Fourier mode $F_1(t)$ as a base mode to generate the Poincaré section and considers its second projection, then the Poincaré iterates of each limiting solution fit an ellipse with remarkable accuracy — as illustrated by Figure 4-18. That is, the cross sections of the surface in Figure 4-17 are very close to ellipses. Currently we have no explanation for this phenomenon, but* behavior of this simplicity should have a theoretically accessible explanation!

Remark 4.2.6 *The pattern by which the Poincaré map iterates fill the contours changes significantly from one limiting solution to another. Sometimes the curves get covered nearly homogeneously while for other solutions the points tend to clump and cover only a few discrete "islands", leaving large spots uncovered. This difference is easily explained in terms of the ratio of the two wave frequencies present in the limiting solutions, namely the ratio ω_1/ω_2 in (4.10). When this ratio is close to a simple rational value, the "island" pattern arises; when not, a more homgeneous covering occurs.*

4.2.5 Internal and Surface Solutions.

Up to this point we have seen and described only **two distinct** families of never-breaking solutions to (2.18), namely:

- Traveling waves (2.21), with δ varying from -1 to 1. This is a one–parameter family of solutions (if we ignore the trivial phase ϕ_0 in (2.21), due to translational invariance of the equations)

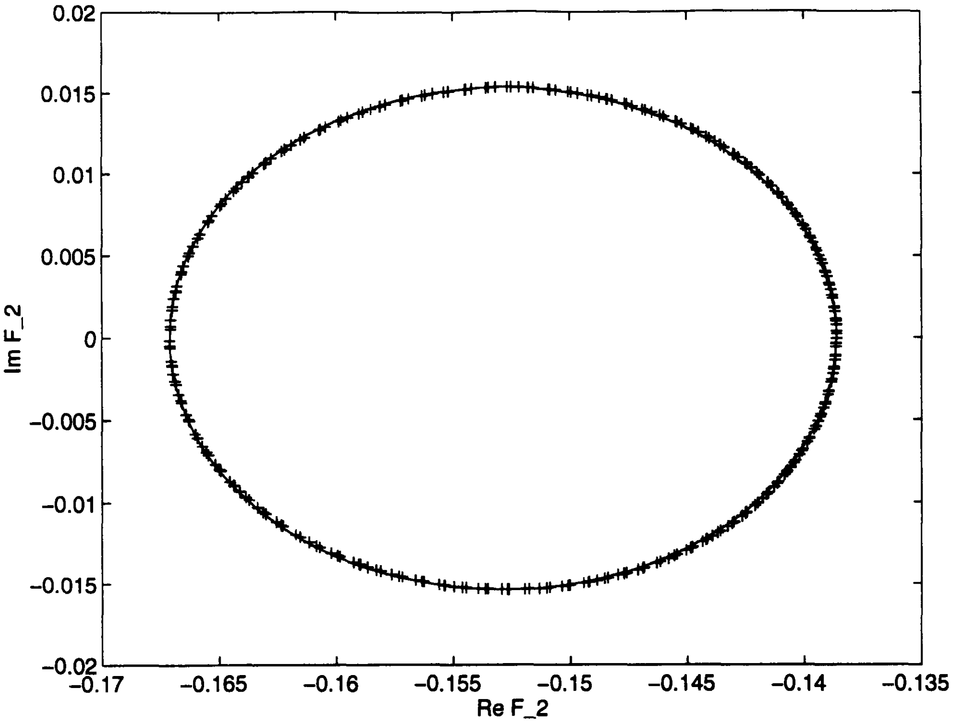

Figure 4-18: Second projection of the Poincaré section induced by F_1 for a limiting solution, fitted by an ellipse. The crosses are the Poincaré map iterates and the smooth line is the ellipse. The fit is remarkably accurate.

- The quasiperiodic limiting solutions with two time periods and sharp spikes due to corner formation, discussed in Sections 4.2.2, 4.2.3 and 4.2.4.

Remark 4.2.7 *It is not clear how many parameters control the quasiperiodic limiting solutions. For a "full blown" two-phase quasiperiodic solution in a nonlinear dispersive system, one would expect two amplitudes and two phase shifts.*[15] *Eliminating the trivial parameter that arises because of the translational invariance of the equations, this would leave three effective parameters.*[16] *But if so, the set of solutions would be "equivalent" to a three dimensional volume, while our numerical experiments (see Figure 4-17) seem to indicate a* surface. *There is thus a parameter "missing". The clear candidate is an amplitude: in the same fashion that, for the traveling waves* only *the maximum amplitude ones are attracting, the fact that here all these quasiperiodic attracting waves have corner singularities, suggests that they are extreme cases of a larger class of solutions. We will show evidence favoring this conclusion in what follows.*

The two sets of solutions listed above share two particular elements: the traveling wave of maximum amplitude with the corner (4.9) and the zero amplitude trivial solution. We know that

---

[15] *Because the space period is fixed to 2π, the wavefrequencies would be determined from the amplitudes.*

[16] *Say, the two amplitudes and the difference between the phase shifts*

other traveling waves (2.21) with $\delta \neq 1$ exist, but are not attracting.[17] However one can check (both numerically and by means of linear stability analysis — see Chapter 5 for details) that these intermediate traveling waves are **neutrally stable**.

As we demonstrated in Section 4.1.2, the traveling waves (2.21) are represented by **single** points on the real axis on each projection plane of a Poincarè section. Hence, they lie at the "axis" of the attracting surface (shown on Figure 4-17, projected on the second mode complex plane). In some loose sense, we can now conjecture that the surface of attracting (limiting) solutions encloses some special volume in phase space, made out of special non–breaking solutions (see Remark 4.2.7 above). The family of traveling waves are then located inside this volume. Of course, this is very vague: the phase space is infinitely dimensional and a surface in it does not "enclose" anything; to make these notions more precise, we will need to find and define this "volume" in a better way — as it turns out, viscosity provides an appropriate tool, which we will explore next in Section 4.3.

Taking, for the moment, as a given the existence of the "volume" postulated in the prior paragraph, we can now divide the non-breaking solutions into two types: **Internal solutions**, which are the ones that are not on the boundary surface and are thus not attracting and **Attracting or Surface solutions** which are the ones we have been dealing with till now. The traveling waves for $|\delta| < 1$ are an example of an internal solution. Finally, we can talk of **External solutions**, which are all the others, that break and form shocks.

For the surface solutions the balance between the steepening, singularity forming, nonlinearity and the dispersive integral term in (2.18) is just critical. So, it is not surprising to find that these solutions present weak (corner) singularities. For the internal solutions, on the other hand, dispersion should dominate — thus we expect these solutions will be smooth.

Remark 4.2.8 *Using these (loose) ideas, we can now "explain" why only the surface solutions should be attracting: as a "general" external solution evolves, it develops shocks and its energy starts decreasing. The solution then begins to approach the set of non-breaking solutions (either this or the energy decreases all the way to zero and the trivial solution*[18] *is approached). It cannot, however, go "inside": as soon as the evolution reaches the "surface", nonlinearity and dispersion balance — thus no shocks are possible — and the energy becomes constant; then the "motion" ceases. That this idea is not as improbable as it seems, will be shown in the next section, where we will use a small amount of viscosity (which provides a way to decrease the energy without need of shocks) to "penetrate" the surface of attractors and construct new, non-breaking,* **internal**, *smooth solutions.*

The traveling waves are isolated from the surface of attractors (and are neutrally stable). In order to have the volume of solutions postulated above, we need to fill the gap between the surface

---

[17] None of these traveling waves ever arose as a limiting solution in our long–time transition experiments described earlier. The attracting set is made out only of quasiperiodic solutions with two time periods.

[18] *Of course, the trivial solution is just one of the attracting solutions.*

(attractors) and the axis (traveling waves) of the set of internal solutions shown in Figure 4-17. We will address this matter in the next Section.

Remark 4.2.9 *The projection of the attracting surface shown in Figure 4-17 is a bit deceiving. In order for solution to be internal,* **all** *the Fourier modes must be located "inside" the surface of attractors. Thus, a function with only a few Fourier modes initially inside the surface*[19] *will almost certainly be an external solution and will generate shocks (that will produce a loss of acoustic energy and an eventual evolution to a lower energy attracting surface solution). The fact is that, in the infinite dimensional space of solutions, the "volume" ocuppied by the non-breaking solutions is a very thin set. Thus the search for internal solutions other than traveling waves can be quite tricky.*

4.3 The influence of Numerical Viscosity.

Virtually all numerical schemes for systems of conservation laws introduce some extra (or "artificial") dissipation into the original equations. The magnitude of this numerical viscosity (for a given scheme) is controlled by the resolution and normally decays with increasing resolution (following the the scheme's order of accuracy). Thus, at least in principle,[20] one can have an arbitrarily small viscosity simply by increasing the number of points in the calculation. In the numerical experiments described so far in this Chapter 4, we used the algorithm described in Chapter 3. By a careful treatment of the singularities (shocks and corners) along with shock tracking, this algorithm achieves high resolution (with a very small amount of dissipation) at a moderate cost.

In this Section we **propose to purposely add numerical viscosity to the calculations**, with the objective of generating new never-breaking solutions of (2.18). The approach is motivated by the argument introduced earlier in Remark 4.2.8: the added viscosity dissipates energy without shocks needed in the solutions. Since the amount of viscosity (thus energy dissipation) depends on the resolution, we can control it rather effectively.[21]

4.3.1 Description of the Experiments.

We conducted a sequence of experiments, in which artificial viscosity was used as a "perturbing" factor for the quasiperiodic attracting solutions of (2.18). Each of these experiments consisted of two separate calculations on grids with different resolutions, performed one after the other and following the **same** solution.

---

[19] Such functions can easily be constructed by, for example, slightly perturbing an attracting solution

[20] In practice, the cost goes up with the resolution!

[21] Our scheme is, basically, second order. Thus, the amount of dissipation should be $O(N^{-2})$, where N is the number of points in the space grid.

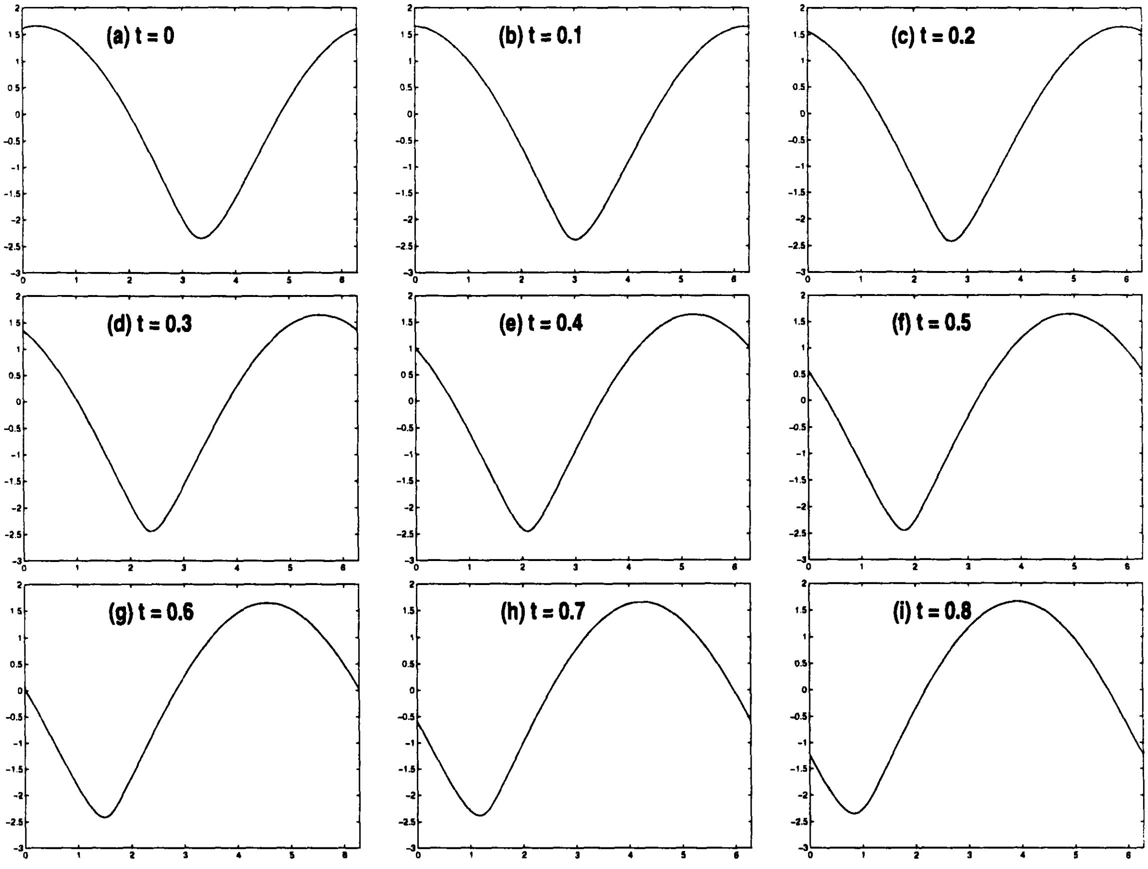

Figure 4-19: Snapshots of a quasiperiodic internal solution in physical space-time — obtained by adiabatic transition. No corners or shocks form, so the solution is smooth. The solution is close but not equal to a traveling wave and shape modulation can clearly be seen. The main period is ≈ 2, corresponding to a wave velocity $s \approx -\pi$. The time origin ($t = 0$) is arbitrary. The vertical and horizontal scales are $-3 < u < 2$ and $0 < x < 2\pi$, respectively.

- In the first computation we used our numerical scheme (described in Chapter 3) on a coarse grid (coarser that those used for the experiments reported earlier in this Chapter). We followed the evolution in this grid until it (basically) reached the limiting attracting solution, and then continued integrating the equation on this same coarse grid for a while longer: until some time t_{switch}.
- At the time $t = t_{switch}$ we turned the numerical viscosity "off" (by a sudden and considerable refinement of the grid) and resumed the calculation on the finer grid.[22]

We conducted, using this approach, a series of experiments. In each we used a fixed set of initial conditions and varied the time t_{switch}.

4.3.2 Generation of New Never Breaking Solutions.

The numerical simulations described above in Section 4.3.1 exhibit the following behavior

Computation on a coarse grid.

- SHOCK TRANSITION STAGE. As in in Section 4.2.1, the solutions first steepen and form shocks that decay. Eventually they settle down to a continuous regime without shocks.
- ADIABATIC TRANSITION. Because of the numerical viscosity, the limiting solutions we obtained at the end of the shock transition stage can no longer hold their energy constant. Therefore they **slowly**[23] drift in phase space towards smaller energies. We call this process **adiabatic transition**, since the energy dissipation rate is so slow that it does not prompt a solution to generate shocks and thus move to the "exterior" (in the sense of the previous Section) of the attracting surface. At the same time, over long enough time intervals, the energy drops considerably. This yields new solutions, since the time evolution is always kept very close to the "exact" one a fully inviscid system would produce.

Computation on a fine grid.

After the viscosity is turned off (at $t = t_{switch}$), the solution continues to evolve in a fashion that **never produces shocks** — so that the energy is a constant — **nor corners**. In other words, a never-breaking smooth solution is generated (thus an internal one, by our prior definition in Section 4.2.5). Furthermore, the **solutions produced by adiabatic transition from the attracting surface are generally not traveling waves** (see Figure 4-19) but in fact **quasiperiodic solutions** of the same type we observed before (except that now the shape oscillations do not involve

---

[22] Of course, the numerical viscosity is never really "off", but we decrease its magnitude considerably. Thus much longer time scales are needed to see its effects.

[23] The grid is "coarse" by the standards of our earlier experiments only: the numerical viscosity is still quite small!

corners). Thus these solutions fill the "gap" (mentioned right after Remark 4.2.8) between the traveling waves and the attracting (surface of) quasiperiodic solutions.[24] In effect, viscosity allows us to introduce into the solutions the extra "missing" parameter that was discussed in Remark 4.2.7: as discussed there, this "missing" parameter is quite likely an "amplitude". Thus, if we can change the energy of a solution without leaving the set of non-breaking solutions, this parameter dependence generally will be involved (except in the rather special cases when the "motion" happens along the surface). The latter is exactly was the adiabatic transition does.

Actually, before we can really conclude that the "whole" volume bounded by the surface in Figure 4-17 has been filled by the solutions just discovered, we must show that we can move "continuously" from the attracting solutions at the surface to the traveling waves (2.21) at the center. This we show next.

4.3.3 Convergence to Pego's Traveling Waves.

The rate of energy dissipation depends entirely on the amount of artificial viscosity introduced by the coarse grid. Still, for a relatively broad resolution range for the coarse grid the general picture remains the same. After a short transition period with shocks and rapid energy drop, a slow "adiabatic" drift in phase space takes over. By changing the moment in time when viscosity is turned off (by the sudden increase in the grid resolution), we can control how far away from the surface of attracting solutions is the resulting solution. At the start of the adiabatic transition, viscous dissipation seems to affect (and damp) principally the "second" mode of oscillation (that is, the one producing the shape modulations in the wave train — illustrated in Figures 4-3 and 4-19 — which is absent for traveling waves). The net effect of this is that, the longer the adiabatic transition lasts, the closer the solution gets to a traveling wave. Thus, adiabatic transitions can be used to "connect" the attracting surface solutions with the traveling waves, via a continuous range of non-breaking quasiperiodic set of solutions. We note that, after the second mode disappears and the solutions become indistinguishable from the traveling waves (see Figures 4-21 and 4-22), the effect of viscosity is to drive the solution along the axis of traveling waves, in the direction of decreasing energy towards the trivial solution.

We present now the results of one series of experiments, where we initiated the calculations with the initial condition $u_(x,0) = 2\sin x$ on a "coarse" grid consisting of 200 points. Then, at various times during the numerical integration ($t = t_{switch}$) we switched to a finer grid (to turn off viscosity) with 2000 points. The behavior of the energy during these calculations is presented in the time-energy plot of Figure 4-20. The course grid calculation yields the line starting with a very

---

[24] Thus, we have found the volume of non-breaking solutions we postulated in Section 4.2.5. That is, the "inside" of the surface depicted in Figure 4-17 — though we stress that we must be careful not to take these concepts too literally, as pointed out in Remark 4.2.9.

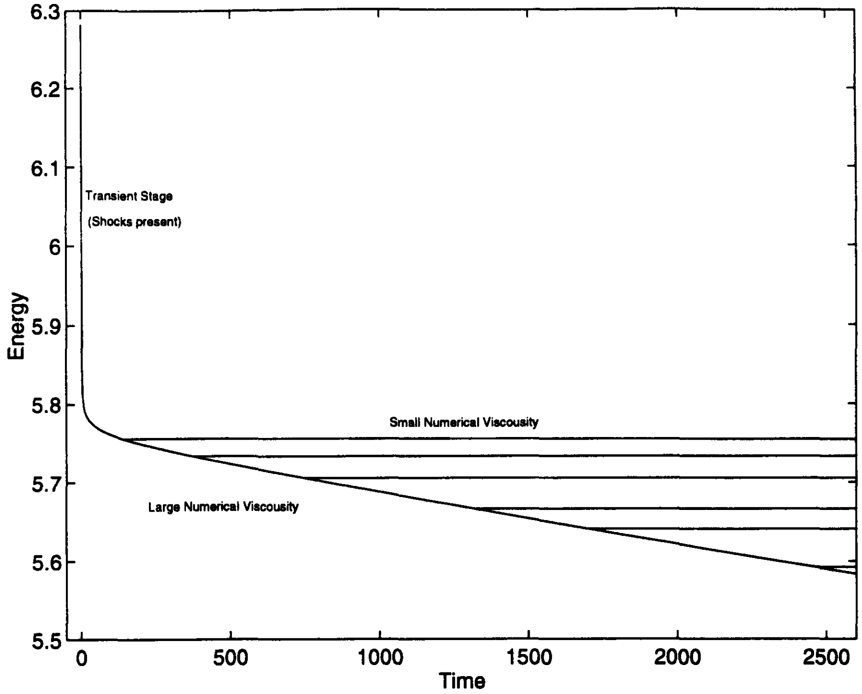

Figure 4-20: Influence of a small amount of artificial viscosity on the limiting solutions. Energy as a function of time for various choices of $t = t_{switch}$. Note the initial steep drop in the energy, during the transient stage with shocks. The initial conditions are $u_(x, 0) = 2 \sin x$. The grids use 200 and 2000 points.

steep negative slope (transient stage with shocks in the solution) followed by a less steep and nearly straight line with negative slope (adiabatic transition stage). The branching and nearly horizontal straight lines correspond to integrations with the finer grid, for various times of branching.

Figure 4-21 shows projections (on F_2) of the Poincaré sections induced by F_1 — plotted versus the energy — for each of the solutions resulting from a branching in the same series of calculations shown in Figure 4-20. Later switching times correspond to lower energies. Two things are obvious from this Figure: **First,** the intermediate solutions are quasiperiodic with two periods — as their sections are closed simple curves. **Second,** convergence to a traveling wave occurs — since the Poincaré sections are shrinking to a point.

Finally, Figure 4-22 compares a "traveling wave" as obtained by the adiabatic transition described above, with an exact traveling wave — as given by equation (2.21). The fit is remarkably good.

Remark 4.3.1 *We also conducted experiments with a pseudo spectral method with various filtering algorithms (in the spirit of [4, 21]). Spectral methods are basically inadequate for the problem we are looking at (largely because of the excessive numerical viscosity inherent to all filtering algorithms). However, the main features of the results in this chapter can be — basically — reproduced, except that one would miss the corners in the attractors. The reason is that such a method behaves, essentially,*

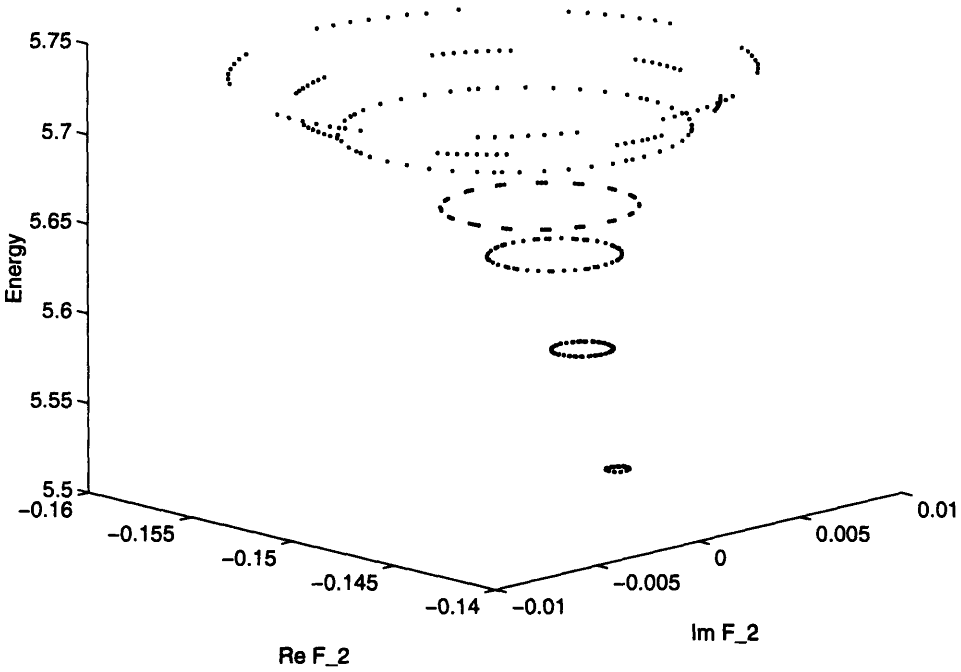

Figure 4-21: Convergence of quasiperiodic solutions (each represented by a closed curve) to a traveling wave (represented by a point) under the influence of numerical viscosity. Second projection (on F_2) of the F_1–Poincaré section plotted against energy. Each curve corresponds to a "branching" point in Figure 4-20.

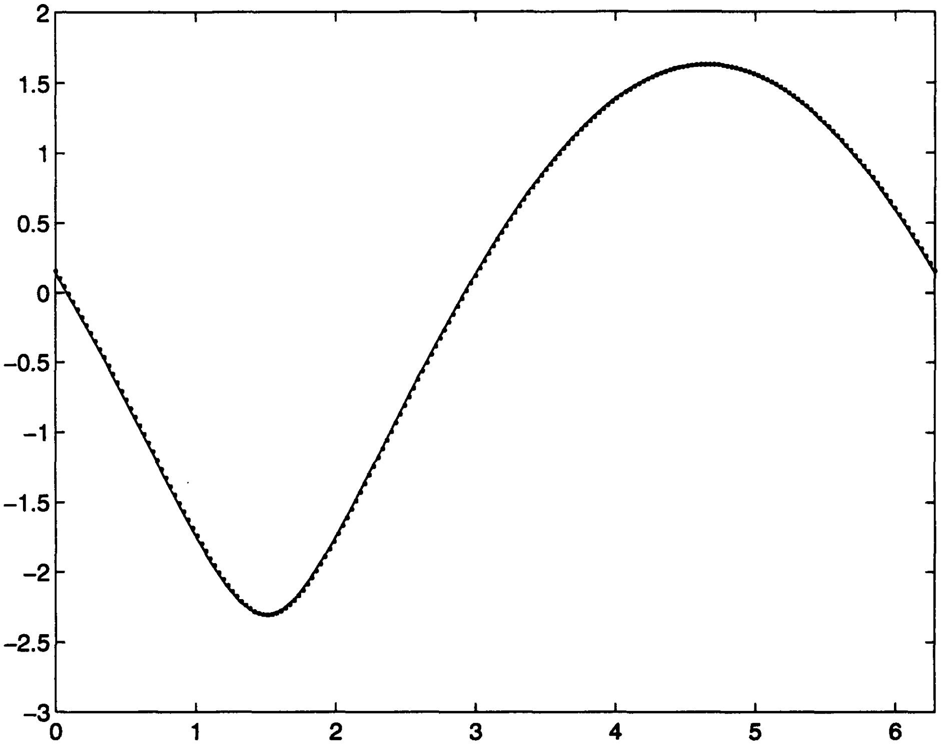

Figure 4-22: Convergence of quasiperiodic solutions to traveling waves in physical space. Here we compare the solution obtained after an adiabatic transition to a traveling wave, with an exact traveling wave. The dotted line is the numerical solution and the solid line is the exact traveling wave.

in the same fashion that our strategy of a coarse grid followed by a fine grid works. As long as the solution has either shocks or corners, filtering will induce appreciable dissipation. However, as the solution moves into the smooth internal solutions range, via adiabatic transition (and the corners are smeared), dissipation by the method decreases precipitously — which is equivalent to our switches to finer grids in this section. Thus, such a method will predict convergency to non-breaking smooth quasiperiodic solutions for large times (missing the corners completely, unless an extremely large number of points is used).

Chapter 5

Two-period Quasiperiodic Perturbations of Traveling Waves. Linear Theory.

5.1 Background.

The purpose of this Chapter is to give reinforcing arguments for the fact that the solutions obtained by adiabatic transition from attracting solutions in Chapter 4, are indeed quasiperiodic with **exactly two** temporal frequencies. Here we develop a linear stability theory for the periodic solutions (that is, the traveling waves[1]) and compare the predictions for perturbations wavefrequencies of this theory with the numerical results. The idea here being that: the shape oscillations observed in the never breaking waves can be associated with the excitation of a mode of vibration for the (neutrally stable) traveling waves. In this sense then, the quasiperiodic solutions would arise as a bifurcation from the traveling waves.

In Chapter 4 we introduced and investigated the quasiperiodic solutions (arising in the limit of long time evolution for arbitrary initial conditions) of the equation

$$\frac{\partial}{\partial t}u(x,t) + \frac{\partial}{\partial x}\left(\frac{1}{2}u^2(x,t)\right) + \int_0^{2\pi} K(x-y)u(y,t)\,dy = 0, \tag{5.1}$$

---

[1] The only periodic solutions we ever observed in our experiments.

with the "single mode" kernel

$$K(x) = \sin(x)\,, \tag{5.2}$$

where 2π-periodic and mean zero solutions were required. These solutions were found to be attracting and (numerically) stable. In addition to them, a large set of other, quasiperiodic and periodic, solutions to equation (5.1) exists (see Sections 2.2 and 4.3). It turns out that a natural set of coordinates (to investigate the periodicity properties of the limiting and the other never-breaking solutions) are the Fourier modes. The results, obtained with the help of projection techniques and Poincaré sections (see Sections 4.1, 4.2.3 and 4.2.4), suggest that the solutions are **quasiperiodic in time with two periods** (and, of course, periodic in space).

In this Chapter we investigate the linear stability of the traveling waves in (2.21) - (2.22), that is

$$u = u(x - st) = s + b\sqrt{1 - \delta\sin(x - st + \phi_0)}\,. \tag{5.3}$$

Since the equations are translational invariant, we can do the analysis in the frame of reference of the traveling wave. In this frame, the unperturbed solution above is time independent; thus the analysis reduces to finding the normal modes of vibration[2] of the linearized equations. Of course, these exactly describe (in the linearized limit) possible shape oscillations for the traveling wave. If only a single one is excited, then the perturbed solution will be periodic in time in the moving coordinate frame of the traveling wave, and quasiperiodic with two periods in the fixed frame of reference. We will compute the periods of these linearized modes of vibration and compare them with the ones observed in the numerically computed quasiperiodic solutions. That is, we will take a quasiperiodic solution (obtained by an adiabatic transition, see Section 4.3) with an almost degenerate shape oscillation mode — so that it is very close to a traveling wave. Then we will compare its shape oscillations with the linearized modes. It will turn out that the oscillations correspond (always) to the lowest linear vibration mode.

This study is motivated by the results described in Section 4.3.3, where we showed that we can continuously move around the set of never breaking solutions (using the technique of adiabatic transition[3]) all the way from the attracting limiting solutions to the traveling waves[4]. This shows, in particular, that we should be able to find two period quasiperiodic solutions arbitrarily close to any traveling wave solution.

---

[2] **Traveling waves turn out to be neutrally stable, so the linearized eigenvalues are all pure imaginary.**

[3] Deforming, adiabatically — i.e., very slowly — the solutions under the influence of artificial viscosity.

[4] Along an **adiabatic path** — that is, the curve in the set of solutions produced by an adiabatic transition — the shape mode of vibration gets suppressed first, so that the solution converges to one of the traveling waves in Section 2.2.

Remark 5.1.1 *We expect that these special linearized solutions, consisting of a traveling wave plus a single mode of vibration, will correspond to a branch of solutions bifurcating from the traveling waves — with bifurcation parameter the amplitude of the shape oscillation, say. The resulting solutions should then be the same as the quasiperiodic in time ones we computed and studied numerically in Chapter 4. The numerical experiments in this chapter seem to support this view, though we do not yet understand why it is only the lowest vibration mode that is excited.*

We are currently studying this bifurcation process in detail, both numerically and analytically, somewhat in the same spirit as the work by Celentano [5] (where he produced time periodic non-breaking solutions for the fully nonlinear regime in Gas Dynamics by a bifurcation strategy from the equilibrium solutions), see also Keller [16]. But this work is not yet advanced enough to be presented in this thesis.

5.2 Linear stability equations.

To facilitate the linear stability analysis for the traveling waves (5.3) it is convenient to switch to a frame moving with speed s, the same as the traveling wave. Thus, we introduce the coordinates

$$x' = x - st \quad \text{and} \quad t' = t\,. \tag{5.4}$$

For convenience we will **drop the primes when referring to these new variables in what follows**, this should not cause any confusion. In this moving frame equation (5.1) takes the following form:

$$u_t - su_x + uu_x + K * u = 0\,, \tag{5.5}$$

where the asterisk is used to denote the integral convolution term. The traveling wave (5.3) becomes then **stationary**

$$u = V_s(x) = s + b\sqrt{1 - \delta\sin(x + \phi_0)}\,, \tag{5.6}$$

with $b = b(s)$ and $\delta = \delta(s)$. In this frame of reference, **quasiperiodic waves with two periods** — of the type our numerical experiments in Chapter 4 showed — become just **periodic**, as only the shape oscillations survive in the moving frame.[5]

---

[5] Actually, for an arbitrary quasiperiodic solution in Chapter 4, the analogy with a traveling wave with a periodic shape oscillation superimposed is not exact. When the shape oscillations are not very small, nonlinear interactions with the "base" traveling wave make this only an approximate picture. But we are considering here very degenerate waves, with the shape oscillations nearly non-existent.

We now consider solutions of (5.5) which are linearized perturbations of (5.6). Namely, let

$$u(x,t) = V_s(x) + w(x,t)\,, \tag{5.7}$$

where w is "infinitesimal." Clearly, $V_s(x)$ solves

$$-sV_s' + V_sV_s' + K * V_s = 0\,. \tag{5.8}$$

Substituting (5.7) into equation (5.5) and linearizing, we get the following equation:

$$w_t - sw_x + wV_s' + V_sw_x + K * w = 0\,, \tag{5.9}$$

where the solution w is required to be 2π-periodic in x with zero mean.

5.2.1 Eigenvalue Problem.

Equation (5.9) is linear homogeneous and can be solved by **separation of variables**. Thus we seek solutions of the form

$$w(x,t) = W(x)e^{i\omega t}\,, \tag{5.10}$$

where ω is a constant (real, it will turn out, so that the traveling waves are neutrally stable). Then the equation reduces to the following eigenvalue problem (for the eigenvalue ω and the eigenfunction W)

$$(V_s(x) - s)W'(x) + V_s'(x)W(x) + K(x) * W(x) = -i\omega W\,. \tag{5.11}$$

Substituting now here the explicit form for V_s in (5.6) and using (5.2), we obtain

$$\left(b\sqrt{1-\delta\sin(x+\phi_0)}\,W(x)\right)' + ((\sin x) * W)(x) = -i\omega W(x)\,, \tag{5.12}$$

where W must be 2π-periodic and have zero mean. Clearly, when $\omega \neq 0$, the zero mean condition is automatic. When $\omega = 0$, one can see that the solutions to this equation (5.12) are $W = F'$ and $W = \partial F/\partial\delta$, where F is defined in (5.15). They correspond to the translational and Galileian invariance of (5.1), respectively. However, only F' satisfies the zero mean condition.

In order to solve this problem, we will use the WKB technique[6] (see [3]) for large values of $|\omega|$. On the other hand, small or moderate values can easily be calculated numerically — using, for

---

[6] **WKB yields exponentially accurate estimates for the eigenvalues. In practice, as we will show, "large" can be as little as 10 or so!**

example, a truncated form of the problem in the Fourier domain (see Section 5.2.3).

5.2.2 WKB Expansion for Large Eigenvalues.

In this Section we consider the case of large values for the frequency in (5.12), $|\omega| \gg 1$. Thus we propose a standard WKB expansion for the solutions, namely

$$W(x) = A(x;\omega)\exp(i\omega S(x)), \tag{5.13}$$

where the function $A(x;\omega)$ must be 2π–periodic in x and is assumed to have a power series expansion in inverse powers of ω — actually, we will not need this last fact for the argument that follows. The phase $S(x)$ must satisfy, for some integer n,

$$S(x+2\pi) = S(x) + \frac{2\pi}{\omega}n. \tag{5.14}$$

To simplify the notation, define now

$$F(x) = b\sqrt{1-\delta\sin(x+\phi_0)} = V_s - s. \tag{5.15}$$

Then, upon the substitution of the WKB form (5.13) into (5.12) we get:

$$((FA)' + i\omega S'FA)\,e^{i\omega S} + \int_0^{2\pi} \sin(x-y)A(y;\omega)e^{i\omega S(y)}\,dy = -i\omega A e^{i\omega S}. \tag{5.16}$$

At this point we observe that, in this last equation (5.16), we can integrate by parts the integral convolution term repeatedly. Because A, its derivatives and the derivatives of S must be periodic — see (5.14) — it is easy to see that, at each level, there will be no boundary contributions. We conclude thus that: **in an expansion of this type, the integral convolution term in (5.12) becomes transcendentally small.** As a result, a **very good (transcendentally so) approximation for the eigenvalues and eigenfunctions can be obtained from the "non-dispersive" version of (5.12)!** Namely, we can use the equation

$$\left(b\sqrt{1-\delta\sin(x+\phi_0)}\,W(x)\right)' = -i\omega W(x), \tag{5.17}$$

to calculate the eigenvalues and eigenfunctions when $|\omega|$ is large. This last equation can be solved exactly and so we get

$$W_n(x) \approx \frac{C}{F(x)}\exp\left(-i\omega_n\int_0^x \frac{dy}{F(y)}\right) \quad \text{and} \quad \omega_n = n\omega^*, \tag{5.18}$$

where C is an arbitrary constant, n is a **large** integer and ω^* is given by the formula

$$\omega^* = 2\pi \left(\int_0^{2\pi} \frac{dx}{F(x)} \right)^{-1} . \tag{5.19}$$

We point out that, in some of our calculations we found this WKB result with $|n| \approx 10$ already within the machine precision of the answer obtained numerically (see Section 5.2.4).

Remark 5.2.1 *Notice that the argument below (5.16) (that leads to the nondispersive approximation (5.17) to the linear stability problem) is not particularly dependent on the choice (5.2) for the kernel in the convolution operator. Generally,* **for any smooth kernel, the nondispersive problem will approximate the traveling wave eigenvalue stability problem for large frequencies with accuracy better than any inverse power of the frequency.** *Of course, other kernels will give rise to* different *formulas for the traveling waves, which will have to be used in (5.15) and (5.17). In fact,* even if the kernel is not smooth, the nondispersive approximation will still hold up to some order *— depending on the degree of non-smoothness. For example, if the kernel consists of series of delta functions*[7] *— just about the worse kind of singularity that can occur, then in the equivalent of (5.16) the integral terms will give $O(1)$ contributions. These will then* affect the shape of the eigenfunctions at leading order, *but* **not the phase** *so that the* WKB eigenvalues will not be affected.

5.2.3 Numerical Approximation for Small Eigenvalues.

WKB theory works well when the eigenvalues are large (where large is not that large). To calculate the smaller eigenvalues, we used a truncated form of (5.12). In Fourier space equation (5.12) can be written as an infinite system of linear algebraic eigenvalue equations:

$$\left.\begin{array}{rlcrcl} k \sum\limits_{m=-\infty}^{\infty} & F_{k-m}A_m & & & = & -\omega A_k \quad \text{for } k \neq \pm 1 , \\ - \sum\limits_{m=-\infty}^{\infty} & F_{-1-m}A_m & + & \pi A_{-1} & = & -\omega A_{-1} , \\ \sum\limits_{m=-\infty}^{\infty} & F_{1-m}A_m & - & \pi A_1 & = & -\omega A_1 , \end{array}\right\} \tag{5.20}$$

where the F_k's and A_k's are the Fourier coefficients of $F(x)$ and $W(x)$, respectively. That is

$$F(x) = \sum_{k=-\infty}^{\infty} F_k e^{ikx} \quad \text{and} \quad W(x) = \sum_{k=-\infty}^{\infty} W_k e^{ikx} .$$

If $|\delta|$ is not too close to 1, $F(x)$ is very smooth and we expect $W(x)$ to be smooth also. Thus, their Fourier coefficients will decay rapidly as $|k| \to \infty$. We expect then that the eigenvalues of the

---

[7] *Corresponding to a piece-wise constant entropy, as the kernel is the derivative of the entropy.*

system (5.20) above will be well approximated by those obtained by truncating the equations to form a finite linear set.[8] Thus, we truncate the system (5.20) above to include only the Fourier coefficients of W in a range $-p \leq k \leq p$, for some ("large") positive integer p. Thus the eigenfunction W will be approximated by

$$W(x) \approx \sum_{k=-p}^{p} A_k e^{ikx} . \tag{5.21}$$

The reduced system can therefore be written as

$$(\mathbf{F}_p + \mathbf{D}_p) \begin{pmatrix} A_{-p} \\ A_{-p+1} \\ \vdots \\ A_{p-1} \\ A_p \end{pmatrix} = -\omega \begin{pmatrix} A_{-p} \\ A_{-p+1} \\ \vdots \\ A_{p-1} \\ A_p \end{pmatrix} , \tag{5.22}$$

where $\mathbf{F}_p$ and $\mathbf{D}_p$ are the $(2p+1) \times (2p+1)$ matrices formed by the Fourier coefficients of $F(x)$ as follows

$$\mathbf{F}_p = \begin{pmatrix} -pF_0 & -pF_{-1} & \cdots & -pF_{-2p} \\ -(p-1)F_1 & -(p-1)F_0 & \cdots & -(p-1)F_{-2p+1} \\ \vdots & \vdots & \ddots & \vdots \\ (p-1)F_{2p-1} & (p-1)F_{2p-2} & \cdots & (p-1)F_{-1} \\ pF_{2p} & pF_{2p-1} & \cdots & pF_0 \end{pmatrix} , \tag{5.23}$$

and

$$(\mathbf{D}_p)_{ij} = \pi(\delta_{i\,-1}\delta_{-1\,j} - \delta_{i\,1}\delta_{1\,j}) , \tag{5.24}$$

where $\delta_{i\,j}$ is the Kronecker delta.

We computed the spectrum of this reduced system for different values of the "cutoff" parameter p and investigated the convergence of the eigenvalues as $p \to \infty$. As an example, we illustrate now the convergence rates with the results of the case when the perturbed traveling wave (5.3) has $\delta = 0.6$. Figure 5-1 shows the spectrum of the reduced system plotted against the size of the truncated system p. It is quite clear that, as soon as the system gets to be large enough for a particular eigenvalue to be "picked", convergence of this eigenvalue happens reasonably fast. In particular, the first few

---

[8] At least for the first few eigenvalues. That is, if we truncate to obtain a system of size N (with N large), then we should expect only the first M eigenvalues — with $1 \ll M \ll N$ to be good approximations.

eigenvalues can be obtained with great accuracy with not too large a p.

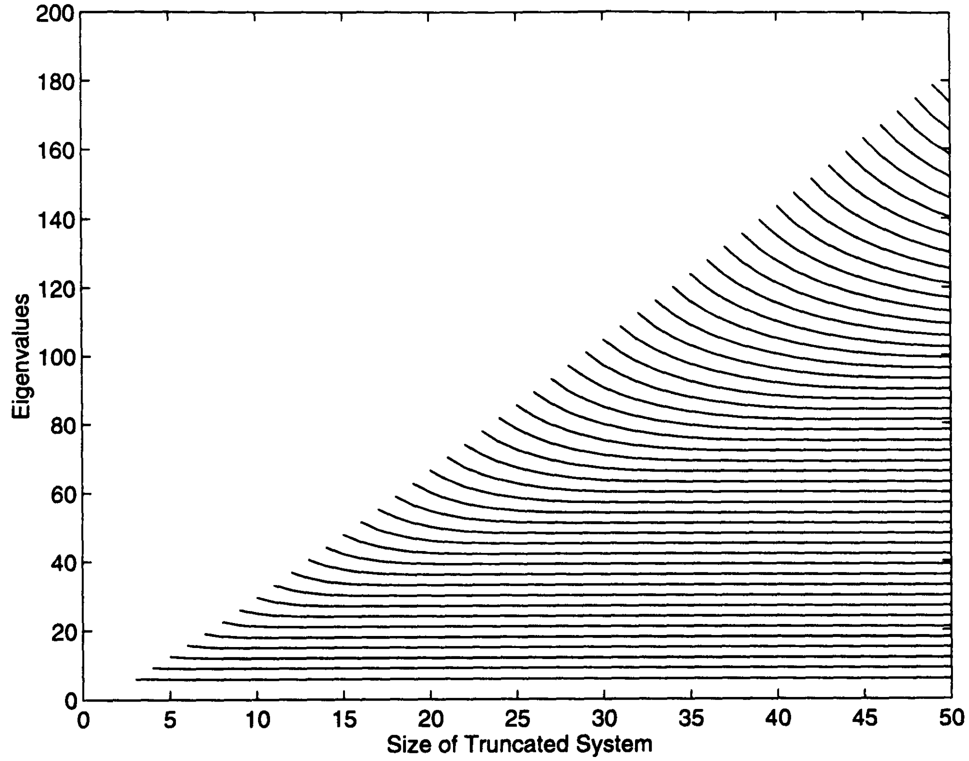

Figure 5-1: Convergence of the eigenvalues computed by truncating the Fourier series, as the size of the truncated system increases. Case of the traveling wave with $\delta = 0.6$.

Remark 5.2.2 *Linear equation*

$$(w_1)_t - s(w_1)_x + w_1 V_s' + V_s(w_1)_x + K * w_1 = 0 \tag{5.25}$$

comprises a Hamiltonian system with the Hamiltonian

$$\mathcal{H}[u] = \int_0^{2\pi} \left((V_s(x) - s)\frac{1}{2}u^2 + u\Pi * u \right) dx. \tag{5.26}$$

Here $*$ represents the convolutions operator and Π is defined as: Π has mean zero and $\Pi'(x) = K(x)$. In the moving frame, each stationary solution $V_s(x)$ is a fixed point *of the system. Since this Hamiltonian system is also* linear, *the set of eigenvalues at each fixed point is restricted to either purely real (saddle-type fixed points in corresponding subspaces) or purely imaginary. The latter come in complex conjugate pairs (centers). No genuinely complex (corresponding to all kinds of* dissipative *modes) eigenvalues are possible, due to the energy conservation, implied by the Hamiltonian struc-*

ture.

In the eigenvalues computations described in Section 5.2.3 we found that all eigenvalues $i\Omega_0$ of (5.12) were purely imaginary, *with the exception of one zero (corresponding obviously to the degenerate mode associated with the zero mean) and a pair of complex conjugate eigenvalues. In this pair, the real part decreases fast with the increase of the size of a system. It brings us to the conclusion, that for the* full *system this pair is also purely imaginary, yielding the overall neutral stability for all traveling waves.*

5.2.4 Spectrum of the Eigenvalue Problem and Physically Realizable Solutions

Figure 5-2 shows the discrepancy between values obtained by numerical calculation for truncated at $p = 100$ system and estimates given by the WKB technique for the same traveling wave $\delta = 0.6$. There is a region of extremely good agreement between the two, where the difference is comparable to the machine precision. As expected, WKB does not work too well for small eigenvalues, who can be very accurately computed by the truncation technique. On the other side, large eigenvalues (where truncating of the Fourier series becomes inefficient) are very well approximated by the WKB values. Therefore, the whole spectrum for perturbations of a traveling wave can be very accurately found by combining the two techniques.

If doubly periodic in time non-breaking solutions do not differ too much from the periodic traveling waves, then their behavior can be thought of as the slight shape modulation on the background of moving with a constant speed wavetrain. The "average" speed of the wavetrain is clearly relevant to the frequency of an "unperturbed" traveling wave. As a first approximation, for small deviations from the stationary solution, the speed of the lowest point in a wavetrain can be used as a measure of first frequency. At the same time, we estimate second frequency by looking at the fluctuations of the lowest point in vertical direction. We present here results of several experiments, in each of which we used integration on a coarse grid to generate artificial viscosity and then integration on a fine grid to monitor the resulting solution.

EXAMPLE 1

Figures 5-3 and 5-4 show horizontal and vertical motion of the lowest point in the wavetrain obtained from initial condition $2\sin x$. This calculation was initiated on the grid consisting of 199 points and then interpolated to the fine grid with 1791 points.

The average speed of the lowest point, according to Figure 5-3 equals to -3.305 which corresponds to $\delta \approx 0.937$. The second frequency of motion can be estimated by the frequency of vertical fluctuations shown on Figure 5-4. It equals to 4.70. The relevant spectrum produced by the linear theory for $\delta = 0.937$ predicts that numerical value is close to the **smallest** eigenvalue in the spectrum

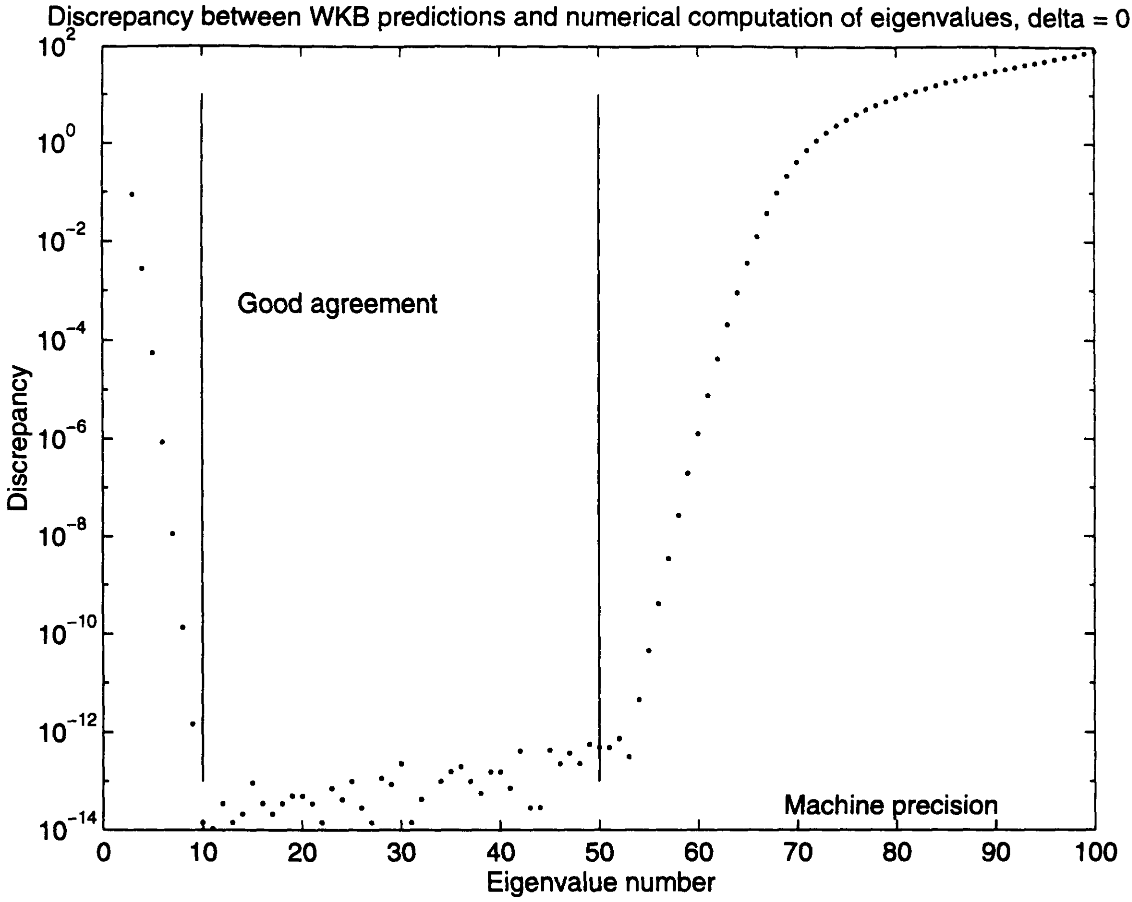
Discrepancy between WKB predictions and numerical computation of eigenvalues, delta = 0.6

Figure 5-2: Agreement between WKB predictions and numerical calculations of the eigenvalues. Region of good agreement is shown.

$\Omega_{0min} = 4.65$.

To illustrate that solution examined in this example is doubly periodic in time, we also present its trajectory on the projection in the phase space on Figure 5-5.

EXAMPLE 2

Figures 5-3 and 5-4 show horizontal and vertical motion of the lowest point in the wavetrain obtained from initial condition $1.4 \sin x$. This calculation was initiated on the grid consisting of 199 points and then interpolated to the fine grid with 1791 points.

The average speed of the lowest point, according to Figure 5-3 equals to -3.231 which corresponds to $\delta \approx 0.795$. The second frequency of motion can be estimated by the frequency of vertical fluctuations shown on Figure 5-4. It equals to 5.58. The relevant spectrum produced by the linear theory for $\delta = 0.795$ predicts that numerical value is close to the **smallest** eigenvalue in the spectrum

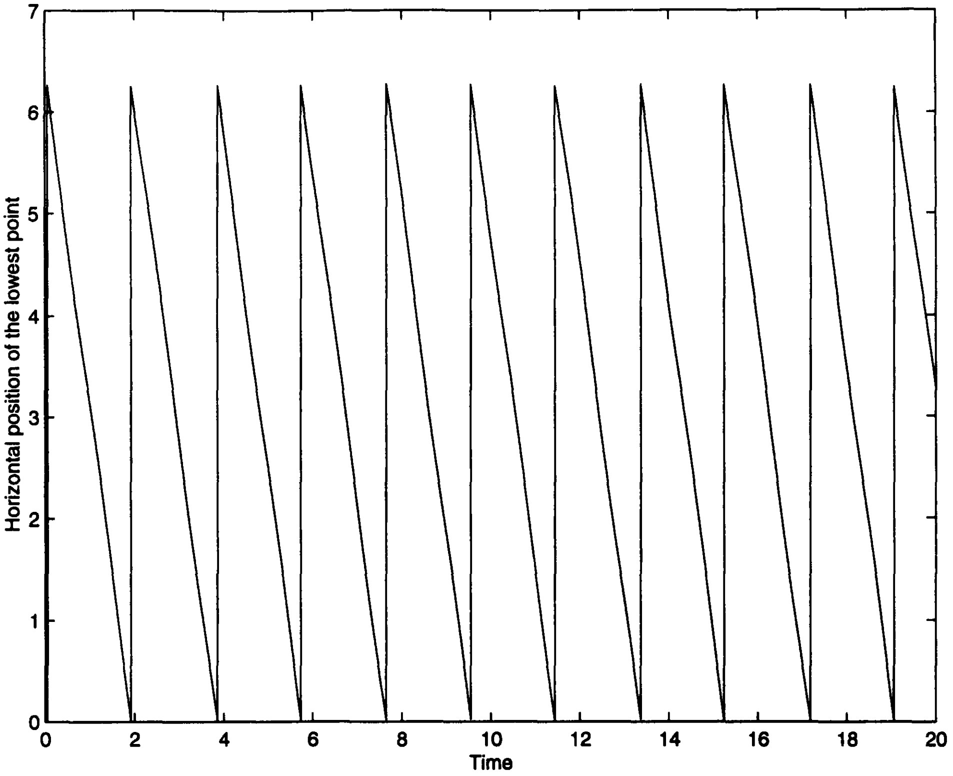

Figure 5-3: Motion of the lowest point in a wavetrain. Horizontal direction. Example 1.

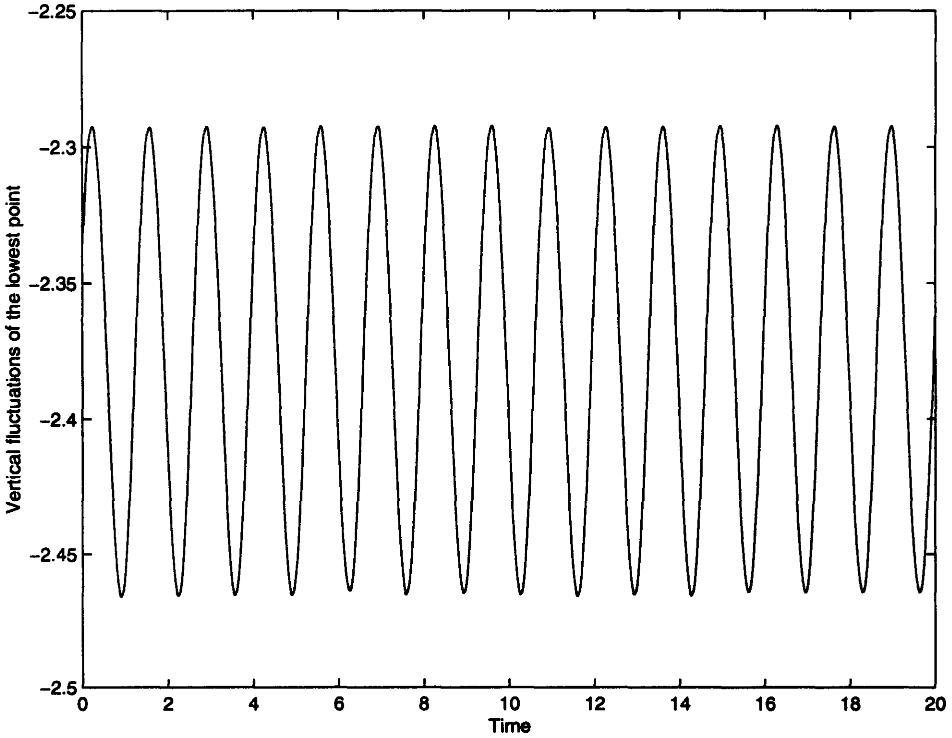

Figure 5-4: Motion of the lowest point in a wavetrain. Vertical direction. Example 1.

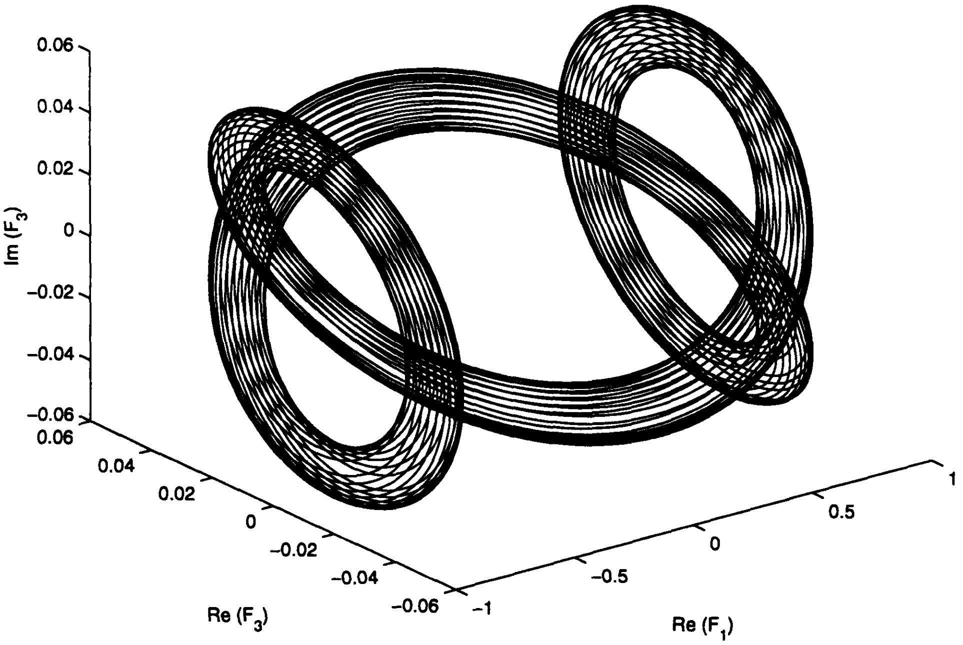

Figure 5-5: Trajectory in Fourier space. Example 1.

$\Omega_{0min} = 5.49$.

Both examples confirm the hypothesis made in Chapter 4 that quasiperiodic solutions have two periods in time. They also suggest that only smallest nontrivial value in the spectrum of the eigenvalue problem associated with linear stability analysis are physically realizable. Each traveling wave (5.3) can be viewed as a fixed point with branches of never breaking solutions bifurcating at different angles. For each frequency s and traveling wave $V_s(x - st)$ in (5.3) it is possible to construct an adiabatic curve of quasiperiodic solutions with two time frequencies branching off from V_s, with one of them equal exactly to s. To illustrate perturbations predicted by the linear theory we compute an eigenfunction corresponding to the smallest eigenvalue for $\delta = 0.6$. Real-valued eigenfunctions satisfying (5.12) are easy to construct due to the symmetries of this equation. If $W(x)$ satisfies equation (5.12) with eigenvalue Ω_0, then its complex conjugate $\overline{W}(x)$ satisfies the same equation with the opposite eigenvalue $-\Omega_0$. Therefore, function

$$w_1(x,t) = \operatorname{Re} T(t) \cdot \operatorname{Re} W(x) - \operatorname{Im} T(t) \cdot \operatorname{Im} W(x) = \cos t \cdot \operatorname{Re} W(x) - \sin t \cdot \operatorname{Im} W(x) \tag{5.27}$$

will be a real-valued solution for (5.12).

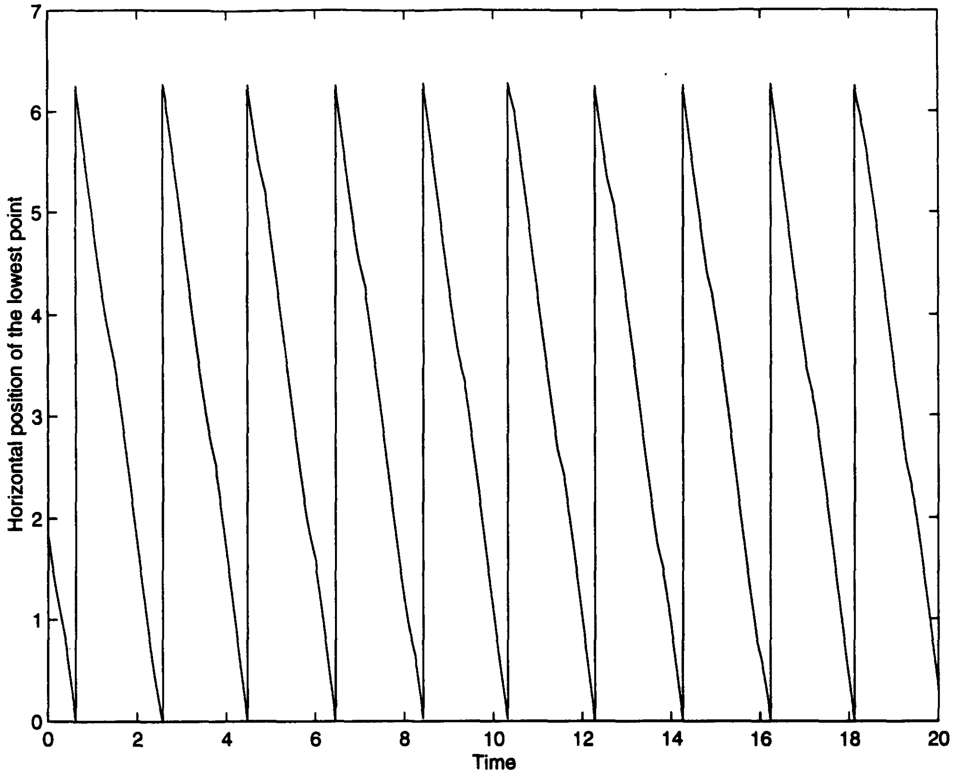

Figure 5-6: Motion of the lowest point in a wavetrain. Horizontal direction. Example 2.

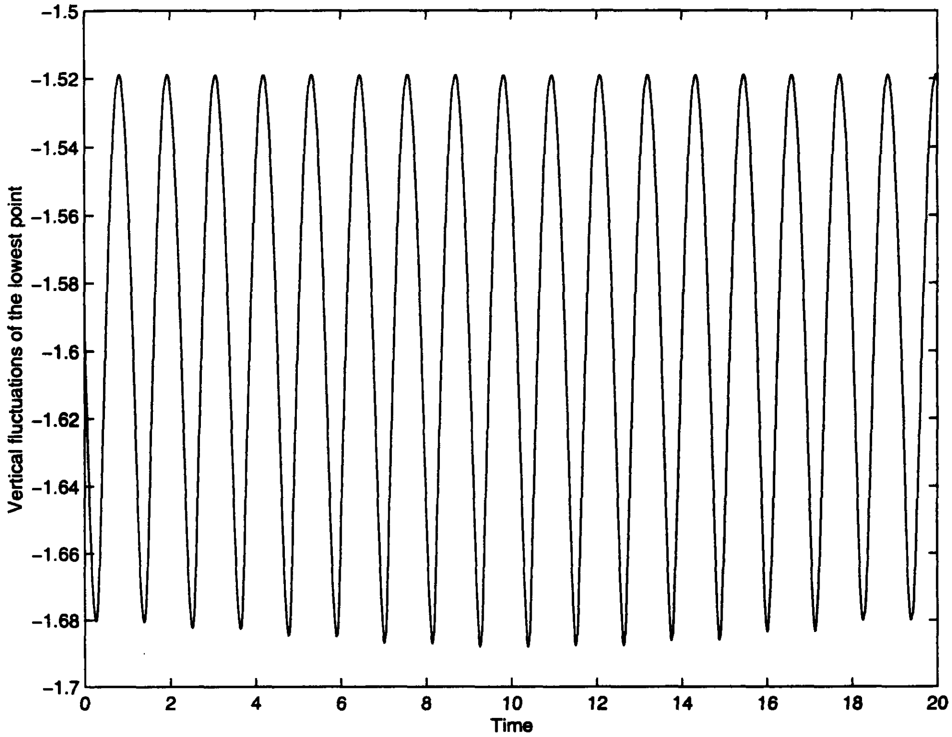

Figure 5-7: Motion of the lowest point in a wavetrain. Vertical direction. Example 2.

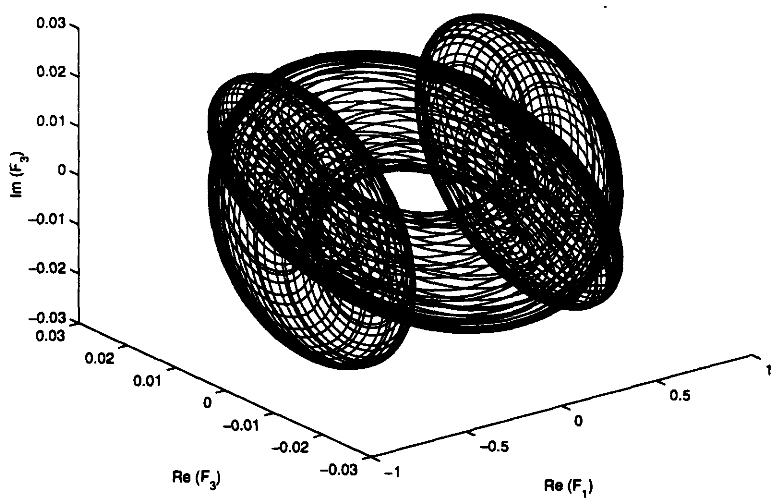

Figure 5-8: Trajectory in Fourier space. Example 2.

Figure 5-9 shows typical real-valued perturbation $w_1(x,t)$ as in (5.27). On Figure 5-10 we present a real-valued perturbation *on top* of the traveling wave in physical space-time.

Figure 5-10 bears a lot of resemblance with internal quasiperiodic solutions obtained by direct numerical simulation and described in Chapter 4.

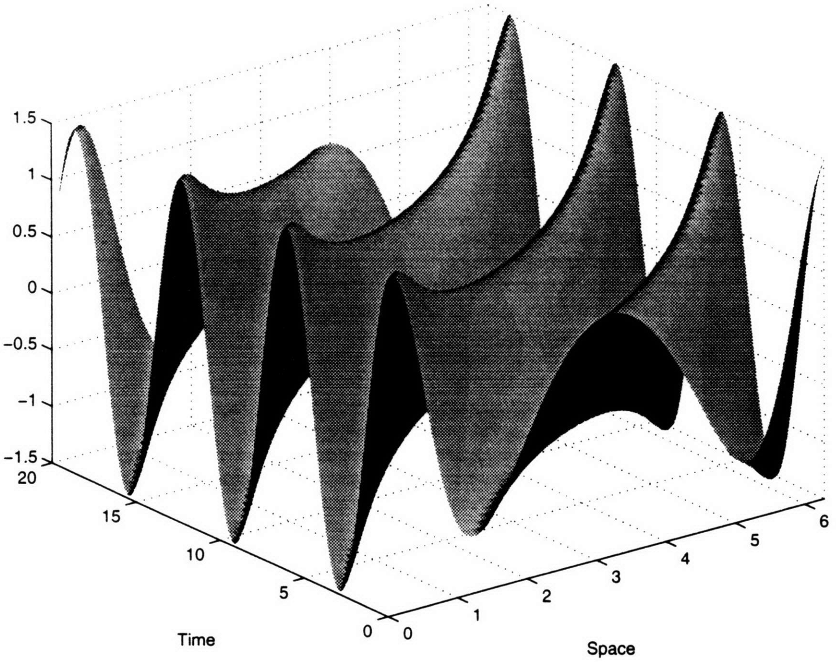

Figure 5-9: Perturbation of the traveling wave with $\delta = 0.6$.

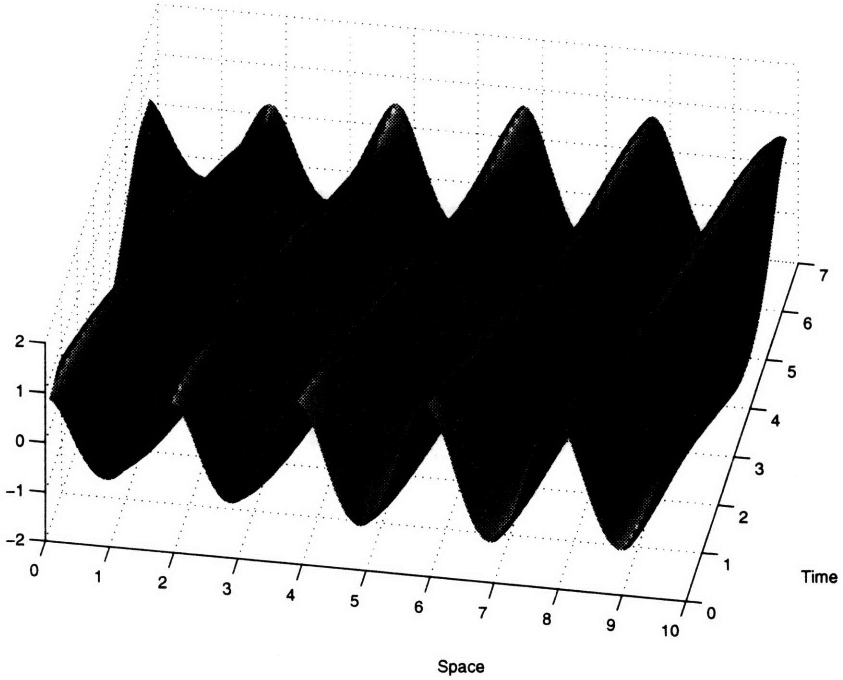

Figure 5-10: Perturbation on top of the traveling wave with $\delta = 0.6$.

Appendix A

Conservation and Hamiltonian Forms.

In this appendix we first exhibit the proper conservation form (for solutions with shocks) of the asymptotic equation (2.18) for nonlinear acoustics used in this thesis. Next we show that the equation can also be written as an infinite dimensional Hamiltonian system, as long as the evolution is smooth (no shocks). The Hamiltonian evolution is "turned off" each time a shock forms, and this gives rise to a curious mixture of dissipative and non dissipative behavior, which should be quite an interesting object of study[1]. Finally we derive a formula for the evolution of the acoustic energy, as it is dissipated by the shocks.

It should be pointed out that the calculations in this appendix have an exact analog for the more general set of asymptotic equations (2.12)–(2.14). In this thesis though, we concentrate on the simpler equation (2.18) that arises in the specific context of in-viscid one dimensional nonlinear acoustics in a tube with closed ends.

A.1 Asymptotic Equations in Conservation Form.

Equation (2.18) appears in the weakly nonlinear regime for the Euler equations (2.1). It is the advective term[2] in the equation that is responsible for the wave profile steepening and the formation of discontinuities (shocks). On the other hand, the linear integral term in the equation has a dispersive nature (as shown in Appendix B), which tends to smooth out any singularities in the solution. Non-breaking solutions with nontrivial acoustic content will occur when these two effects balance.

---

[1] In fact, the same behavior should arise in the context of the full system of Euler equations (2.1).

[2] In the Burgers' "part" of the equation.

In order to deal with solutions with shocks, a conservation form is needed. It is clear that equation (2.18) can be put into such a form:

$$\mathbf{u}_t + \mathbf{F}(\mathbf{u})_x = \mathbf{0}\,, \tag{A.1}$$

where

$$F(u) = \frac{1}{2}u^2 + \int\limits_0^{2\pi} \Pi(x-y)u(y,t)\,dy = \frac{1}{2}u^2 + \Pi * u\,. \tag{A.2}$$

Here $*$ is the convolution operator and Π is defined by: Π has mean zero and $\Pi'(x) = K(x)$. **This is the proper conservation form for shocks**, since it guarantees the conservation of mass, momentum and energy (as the Euler equations (2.1) require.) This follows easily from (2.8)-(2.10), (2.15) and (2.16). A conservation form is also the best suited for numerical calculations involving shocks, a well known fact in the theory of numerical methods for hyperbolic conservation laws (see [17], for example.)

Since the integral term is lower order, it does not contribute at the shocks. It follows that the Rankine–Hugoniot and Entropy conditions are:

$$s = \frac{1}{2}(u_- + u_+) \qquad \text{and} \qquad u_- > s > u_+\,, \tag{A.3}$$

where s is the shock speed, u_+ is the value of u immediately ahead of the shock and u_- is the value immediately behind.

A.2 Hamiltonian Structure.

For continuous solutions $u(x,t)$, equation (2.18) can be written in Hamiltonian form (see [2, 1] for reference on canonical Hamiltonian representations). The Hamiltonian is given by

$$\mathcal{H}[u] = \frac{1}{2}\int\limits_0^{2\pi} \left(\frac{1}{3}u^3 + u\,\Pi * u\right) dx\,, \tag{A.4}$$

where $\Pi(x)$ is as in (A.2). It is easy to see then that equation (2.18) can be written in the generalized (infinite dimensional) Hamiltonian form

$$u_t = -\frac{\partial}{\partial x}\frac{\delta}{\delta u}\mathcal{H}[u]\,, \tag{A.5}$$

where $\frac{\delta}{\delta u}$ denotes the variational derivative (see for example [1, 15]). The Fourier coefficients of u provide a set of canonical coordinates. Namely, if we write

$$u(x,t) = \sum_{1}^{\infty} \sqrt{\frac{n}{4\pi}} \left\{p_n(t)\cos(nx) + q_n(t)\sin(nx)\right\} , \tag{A.6}$$

then the p_n's and q_n's form a canonical conjugate set of variables[3]. Similar expressions were obtained in [10] for KdV equation. Fourier modes turn out to be a convenient set of variables and we used the projection of the solution on the first few of them to analyze the results of numerical simulations.

However, the Hamiltonian behavior is valid only as long as the solution has no shocks. Should the solution lose its continuity, the behavior immediately becomes dissipative, with the rate of energy loss proportional to the shock strength (see the next subsection). This **"semi"–Hamiltonian structure** makes these equations rather peculiar. For example, in none of our numerical calculations did we observe chaotic or ergodic behaviors[4]. Furthermore, only relatively simple solutions with a few dominant modes (see the discussion of the numerical experiments in Section 4.2) survive in the course of time evolution. It is unlikely that this is due to any "simplicity" in the Hamiltonian behavior. Even Complete Integrability would not prevent solutions with many periods (in time) from existing, while we consistently observed just two periods in the limit behavior[5]. We conjecture that it is the dissipative behavior induced by shock formation that is responsible for this simple behavior. It appears that any possible ergodic behavior in the system triggers the dissipation (by leading to the formation of shocks).

A related and interesting property of equation (2.18) is that it appears to have an attracting set to which most solutions converge. This is a typical property of dissipative systems. The attracting set fills in some region in the phase space of (A.5) and is made up of solutions that never develop shocks. The energy range spanned by the attracting (or limiting) solutions is continuous and bounded. In fact, our numerical calculations suggests that this set is a two dimensional surface, topologically equivalent to a sphere!

A.3 Conservation of Energy.

It is interesting to note that the Hamiltonian $\mathcal{H}$ in (A.4) is not the energy in the system[6]. In Appendix C we derive a formula for the total acoustic energy in the flow, equation (C.8), which turns out to be the same (except for a multiplicative factor) as the L_2 norm for the solution of

---

[3] Note that there is no zero mode, since u has vanishing mean.

[4] As normally expected for any Hamiltonian system of dimension greater than 2.

[5] Just in case, we looked for conserved quantities, but were unable to find any more than the obvious ones: the Hamiltonian itself and the Acoustic Energy, discussed in the next subsection. If there are any, it seems unlikely that they would have a simple form.

[6] In fact, we do not know what the physical meaning of $\mathcal{H}$ is.

(2.18), as given by E in equation (2.23) in Section 2.2. In this section we derive a formula for the time evolution of the acoustic energy.

It is clear that equation (2.18) conserves the acoustic energy

$$E(t) = \frac{1}{4\pi} \int_0^{2\pi} u^2(x,t)\, dx\,, \tag{A.7}$$

as long as the solution remains smooth[7]. This follows easily upon multiplying equation (2.18) by $u(x,t)$, which yields (if u has no shocks) the equation

$$\frac{\partial}{\partial t}\left(\frac{1}{2}u^2\right) + \frac{\partial}{\partial x}\left(\frac{1}{3}u^3\right) + u\, K * u = 0\,. \tag{A.8}$$

Since the kernel K is odd, upon integrating this equation over a period in x, the last term gives no contribution. Thus E is conserved.

When shocks occur this last equation must be modified, as the *singular contributions from the first two terms do not cancel.* In fact, using equation (A.3), it is easy to calculate the needed corrections. The equation must be replaced by

$$\frac{\partial}{\partial t}\left(\frac{1}{2}u^2\right) + \frac{\partial}{\partial x}\left(\frac{1}{3}u^3\right) + u\, K * u = -\frac{1}{12} \sum_{shocks} [u]^3_{shock} \delta(x - x_{shock}(t))\,, \tag{A.9}$$

where $[u] = (u_- - u_+) > 0$ denotes the jump at the shock, x_{shock} is the position of the shock and $\delta(\,.\,)$ is Dirac's delta function. It thus follows that the rate of energy change due to shocks is given by

$$\frac{d}{dt}E = -\frac{1}{24\pi} \sum_{shocks} [u]^3_{shock}\,. \tag{A.10}$$

Thus the **acoustic energy is dissipated by the shocks,** as $[u] > 0$ from the Entropy condition in (A.3). This is the same result that applies for Burgers' equation (case $K = 0$.)

---

[7] Therefore non-breaking solutions have constant energy.

Appendix B

Model Dispersive Equation.

Consider the linearization of equation (2.18) for the case of very small values of u. We will show here that the resulting equation is dispersive, thus proving our claim that the linear integral term in (2.18) is of a dispersive nature[1]. However, this dispersive behavior is "weak", in the sense that as the wavelength goes to zero the "dispersiveness" becomes less important. This is the reason that the dispersive term can "balance" the nonlinear term and prevent shock formation only in a limited amplitude range: if the amplitude is large enough, then nonlinearity "wins" and shocks form.

The linearized equation can be written in the form

$$\begin{aligned} \tfrac{\partial}{\partial t} u(x,t) &= -\int_0^{2\pi} K(x-y)\, u(y,t)\, dy \\ &= -\int_0^{2\pi} K(z)\, u(x-z,t)\, dz\,. \end{aligned} \tag{B.1}$$

This equation is not only linear but also translational invariant. Thus it can be solved by separation of variables, with elementary solutions of the form

$$u = Ae^{i(kx-\omega t)}\,.$$

The zero mean and 2π–periodicity requirements restrict the wavenumber to $k = \pm 1, \pm 2, \pm 3 \ldots$ Substituting into the equation it is easy to see that this is a solution provided ω satisfies the *Dispersion Relation*

$$\omega = -i \int_0^{2\pi} K(z)\, e^{-ikz}\, dz = -2\pi i\, \hat{K}(k)\,, \tag{B.2}$$

---

[1] Thus it tends to smooth out singularities in the solution.

where $\hat{K}(k)$ is the k^{th} Fourier coefficient of K. Because K is odd, ω is real. Furthermore, ω is not a linear function of k, for K is a function (not a distribution.) Thus, the equation is dispersive.

Notice that as $|k| \to \infty$ the wavenumber ω vanishes. Thus, for short waves the convolution term does not have a strong effect (this is what we meant at the beginning of this Appendix when we said that the dispersion was "weak"). Basically, this means that the "power" of this dispersion to smooth out the solution does not "grow" as the waves get steeper. Thus it will not always balance the nonlinear term, as would be the case in a "strongly" dispersive equation like (for example) the KdV equation

$$u_t + uu_x - u_{xxx} = 0\,.$$

Here $\omega = k^3$ and the third term becomes dominant for short enough waves, no matter how strong the nonlinearity.

Remark B.0.1 *It is interesting to point out that the "slow time" $\tau = \epsilon t$ introduced in the multiple scales expansion (2.8)–(2.10), has a natural physical interpretation*[2]*. The nondimensionalization of the time t is chosen so that an "acoustic" period*[3]*. is 2π in terms of t. Thus t measures time in terms of acoustic events. On the other hand, entropy variations introduce "weak" dispersion into the system, as shown in this section. This dispersion has a natural set of frequencies (or periods) and τ is nondimensionalized so that these frequencies are $O(1)$ in terms of τ. This is clear from equation (B.2). Thus τ measures time in units of dispersive events.*

Finally, note that equation (B.2) and the definition of τ imply that

$$\mathcal{D}_{per} = O\left(\frac{1}{\mathbf{E_S}}\right)\,, \tag{B.3}$$

where $\mathbf{E_S}$ is the amplitude of the entropy variations present in the solution and $\mathcal{D}_{per}$ is a typical dispersive time-scale.

---

[2] Recall that the time over which equations (2.18) and (B.1) above evolve, is actually τ.

[3] The time it takes sound to travel back and forth across the tube.

Appendix C

Acoustic Energy and Entropy.

In this appendix we derive a (leading order asymptotic) formula for the acoustic energy of the weakly nonlinear waves in Section (2.1) and relate it to the total energy in the flow. Except for a multiplicative constant factor, the acoustic energy is given by equation (2.23) in Section (2.2). We show that changes in the acoustic energy occur only due to shocks, with the increase in the entropy produced by the shocks being directly proportional to the decrease in the acoustic energy.

We note that in this Appendix we go back to the original notation for the independent variables, rather than the usage introduced in equations (2.16)–(2.18) — that is: here x and t have the meaning given to them in the Euler equations (2.1) and the nondimensionalization in (2.6).

The total energy $\mathbf{E_T}$ is conserved by the Euler equations (2.1). In nondimensional variables it is given by the formula

$$\mathbf{E_T} = \int_0^\pi \rho\,(e + \frac{1}{2}v^2)\,dx = \int_0^\pi \mathcal{E}\,dx\,, \tag{C.1}$$

where $e = e(\rho, S)$ and $\mathcal{E}$ is the total energy density per unit length. We chose the nondimensional variables[1] in such a way that, for the equilibrium state $\rho = 1$ and $S = 0$, we have $c = 1$ and $p_S = 1$. It follows then from (2.2)–(2.4) that we also have

$$e_\rho = p_0\,, \quad e_S = T_0\,, \quad e_{\rho\rho} = 1 - 2p_0\,, \quad e_{\rho S} = 1 \;\text{ and }\; e_{SS} = \kappa_0\,, \tag{C.2}$$

where p_0, T_0 and κ_0 are the values at equilibrium of the pressure, temperature and T_S, respectively.

In the weakly nonlinear regime of Section (2.1): v, S and $\delta\rho = (\rho - 1)$ are small, of size $O(\epsilon)$.

---

[1] See Remarks 2.1.2 and 2.1.3 in Section 2.1.

Thus we can expand

$$\begin{aligned} \mathcal{E} = \rho(e + \tfrac{1}{2}v^2) \quad &= \quad e_0 + (p_0 + e_0)\delta\rho + T_0\, S + \\ & \tfrac{1}{2}((\delta\rho)^2 + v^2) + (1 + T_0)\delta\rho\, S + \tfrac{1}{2}\kappa_0 S^2 + O(\epsilon^3)\,, \end{aligned} \tag{C.3}$$

where e_0 is the value at equilibrium of the internal energy e.

Next we will use this expansion in the equation for the total energy $\mathbf{E_T}$ above. Because mass is conserved and we nondimensionalized so that the mean of ρ is 1, it follows that the integral of $\delta\rho$ must vanish. On the other hand, we must be careful with the integral of S. At the leading orders S is a conserved quantity[2], but here we are doing a higher order calculation. Thus we write

$$\mathbf{S_T} = \int_0^\pi \rho S\, dx = \int_0^\pi S\, dx + \int_0^\pi \delta\rho\, S\, dx\,, \tag{C.4}$$

where $\mathbf{S_T}$ is the total entropy. This quantity changes — only when shocks occur — at an $O(\epsilon^3)$ rate. Given our nondimensionalization and the fact we are looking at the evolution over long $O(\epsilon^{-1})$ time spans, it turns out that we can write[3]

$$\mathbf{S_T} = \epsilon^2 \mathcal{S}_\mathbf{T}(\tau)\,, \tag{C.5}$$

where $\tau = \epsilon t$, as in Section 2.1.

Thus — using (C.3)–(C.5) and the fact that $\delta\rho$ has vanishing mean — from (C.1) we obtain

$$\frac{1}{\pi}\mathbf{E_T} = e_0 + \frac{1}{2\pi}\int_0^\pi \left((\delta\rho)^2 + v^2 + 2\,\delta\rho\, S + \kappa_0\, S^2\right)\, dx + \frac{1}{\pi}\epsilon^2\, T_0 \mathcal{S}_\mathbf{T} + O(\epsilon^3)\,. \tag{C.6}$$

Finally, we substitute into this last equation the asymptotic expressions in equations (2.8)–(2.10). We use the identity in (2.15) and the facts that (i) the σ_i's are 2π–periodic and (ii) σ_2 is even, to obtain

$$\begin{aligned} \tfrac{1}{\pi}\mathbf{E_T} \quad &= \quad e_0 + \epsilon^2 \left\{ \tfrac{1}{\pi}\int_0^{2\pi} (\sigma_1(x,\tau))^2\, dx + \tfrac{1}{\pi}T_0 \mathcal{S}_\mathbf{T} + \tfrac{1}{2\pi}(\kappa_0 - 1)\int_0^\pi (\sigma_2(x))^2\, dx \right\} \\ & \quad + O(\epsilon^3)\,, \end{aligned} \tag{C.7}$$

where we have made explicit the fact that σ_2 is time independent.

The first term inside the brackets in (C.7) is the contribution to the total energy by the acoustic

---

[2] A fact that was used in the nondimensionalization — see Remark (2.1.3).

[3] A fact that we finish justifying below.

waves in the gas. That is

$$\mathbf{E_A} = \epsilon^2 \int_0^{2\pi} (\sigma_1(x,\tau))^2\, dx = 4\pi \left(\frac{\epsilon}{\beta_1}\right)^2 E\,, \tag{C.8}$$

where $\mathbf{E_A}$ is the total acoustic energy and E is as[4] in (2.23) of Section 2.2. Furthermore, since the last term inside the brackets in (C.7) is a constant, it follows that

$$\int_0^{2\pi} (\sigma_1(x,\tau))^2\, dx + T_0 \mathcal{S}_{\mathbf{T}} = \textbf{constant.} \tag{C.9}$$

This shows that the acoustic energy changes only when shocks (which are dissipative) occur. The acoustic energy losses are directly proportional to the entropy produced by the shocks.

In Appendix A a direct calculation of the rate of acoustic energy loss by the shocks can be found in equation (A.10). Thus, using (C.8) and (C.9), we obtain the formula

$$\frac{d}{d\tau}\mathcal{S}_{\mathbf{T}} = \frac{1}{6T_0} \sum_{shocks} [u]^3_{shock} \tag{C.10}$$

for the rate of entropy production by the shocks. Here $[u] > 0$ is the jump across each shock, as defined in (A.9).

---

[4] **Here we used (2.16) in Section 2.1 to relate σ_1 and u.**

Appendix D

On Rate of Convergence to Limiting Solutions

In this appendix we illustrate the convergence properties of solutions for equation

$$\frac{\partial}{\partial t}u(x,t) + \frac{\partial}{\partial x}\left(\frac{1}{2}u^2(x,t)\right) + \int\limits_0^{2\pi} K(x-y)u(y,t)\,dy = 0\,, \tag{D.1}$$

to attracting solutions. Energy dissipation rate can serve as a good measure of how far current solution is from its attractor. Figures D-1, D-2 and D-3 illustrate the dissipation rate of acoustic energy (expressed in terms of dimensionless parameters)

$$2\pi E(t) = \int_0^{2*\pi} \frac{u^2(x,t)}{2}\,dx. \tag{D.2}$$

As an example, we used the solution developing from initial condition $u(x,0) = 2\sin(x)$, which can be considered typical. After a very short (invisible on Figure D-1) interval of time, when solution is smooth, a single shock forms, which is reflected by a **sharp drop** in energy on Figure D-1. To set a time scale, we use the period of the corresponding limiting solution, which in our example is roughly equal to 3[1]. Figure D-2 shows that during first 40 periods (roughly 40 iterates of a Poincaré map) energy decays **algebraically**, much the same way as for the in-viscid Burgers equation. This gives a clear indication that main dissipation mechanism on this stage is via **shocks**. After the initial stage with shocks, the convergence rate becomes **exponential** as clearly seen on Figure D-3. Exponential rate of decay is more typical for **viscous** dissipation. Since the model has no natural viscosity, we speculate that at this stage energy dissipates due totally to the numerical viscosity. This yields that

---

[1] As pointed out in Remark B.0.1 of Appendix B time is nondimensionalized in terms of the *amplitude of entropy variations.*

solution essentially converges after roughly 30 – 50 cycles, **with no shocks after that**.

The last part of the graph on Figure D-3 ($t > 800$) can not be deemed credible, since the measurement error becomes of the same order as the energy difference itself.

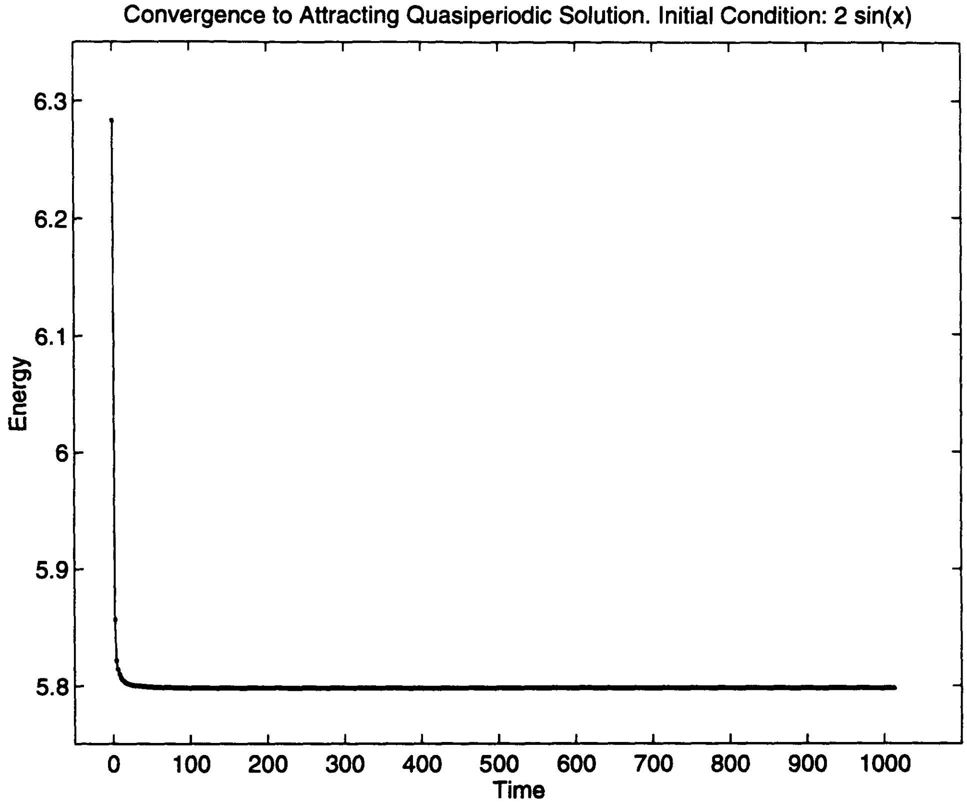

Figure D-1: Dissipation of energy in a typical experiment. Regular axes.

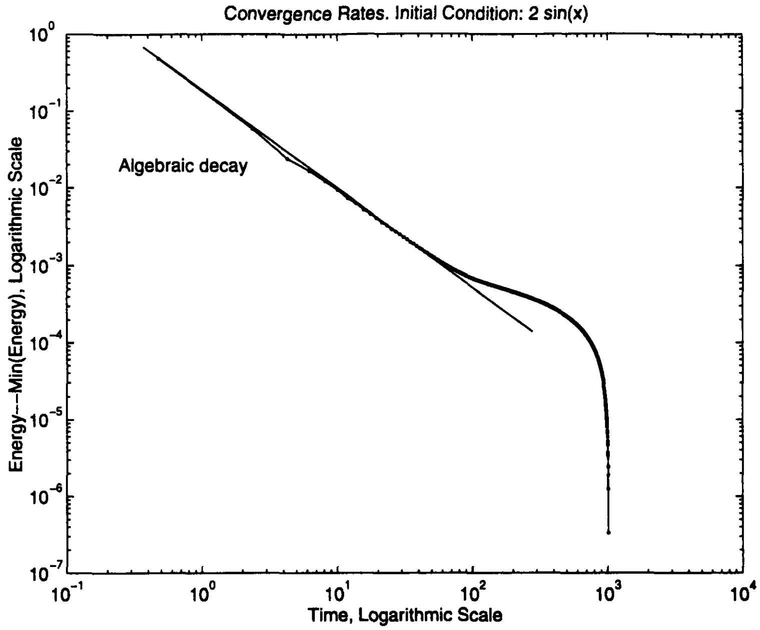

Figure D-2: Dissipation of energy in a typical experiment. Logarithmic axes.

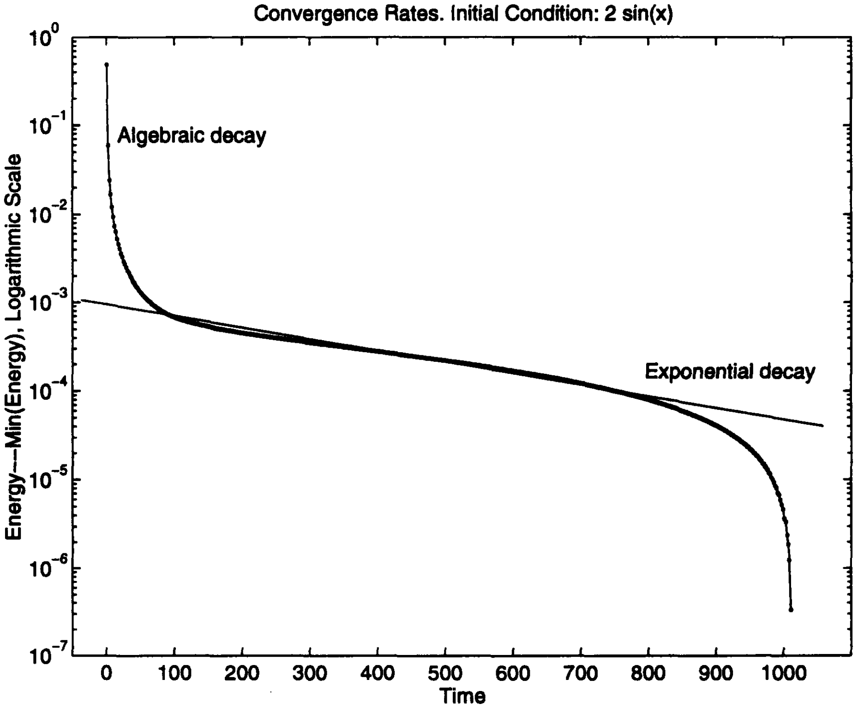

Figure D-3: Dissipation of energy in a typical experiment. Semi-logarithmic axes.

Bibliography

[1] M. Ablowitz and H. Segur. *Solitons and the Inverse Scattering Transform.* SIAM, Philadelphia, 1981.

[2] V. I. Arnold. *Mathematical Methods of Classical Mechanics.* Springer-Verlag, New York, 1978.

[3] C. M. Bender and S. A. Orszag. *Advanced Mathematical Methods for Scientists and Engineers.* McGraw-Hill, 1978.

[4] C. Canuto, M. Y. Hussaini, A. Quarteroni, and T. A. Zang. *Spectral Methods in Fluid Dynamics.* Springer-Verlag, New York, 1988.

[5] C. Celentano. *Finite Amplitude Resonant Acoustic Waves Without Shocks.* PhD dissertation, MIT, Department of Mathematics, January 1995.

[6] P. Colella and P. R. Woodward. The piecewise parabolic method (PPM) for gas-dynamical simulations. *J. Comp. Phys.*, 54:174–201, 1984.

[7] R. Courant and K. O. Friedrichs. *Supersonic Flow and Shock Waves.* Springer Verlag, New York, 1984.

[8] G. Dahlquist and A. Bjorck. *Numerical Methods.* Prentice-Hall, Englewood Cliffs, 1974.

[9] S. Gabov. On Whitham's equation. *Soviet Math. Dokl.*, 19:1225–1229, 1978.

[10] C. S. Gardner. Korteweg-de Vries equation and generalizations. IV. The Korteweg-de Vries equation as a Hamiltonian system. *J. Math. Phys.*, 12:1548–1551, 1971.

[11] S. K. Godunov. A difference scheme for numerical computation of discontinuous solutions of equations of fluid dynamics. *Mat. Sb.*, 47:271–306, 1959.

[12] J. Guckenheimer and P. Holmes. *Nonlinear Oscillations, Dynamical Systems, and Bifurcations of Vector Fields.* Springer Verlag, New York, 1983.

[13] A. Harten and J. M. Hyman. Self-adjusting grid methods for one-dimensional hyperbolic conservation laws. *J. Comp. Phys.*, 50:235–269, 1983.

[14] A. Harten and S. Osher. Uniformly high-order accurate nonoscillatory schemes. I. *SIAM J. Numer. Anal.*, 24:279–309, 1987.

[15] A. Hasegawa and Y. Kodama. *Solitons in Optical Communications.* Clarendon Press, Oxford, 1995.

[16] H. B. Keller. *Numerical Methods for Two-Point Boundary-Value Problems.* Dover Publications, Inc., New York, 1992.

[17] R. LeVeque. *Numerical methods for hyperbolic conservation laws.* Birkhäuser, Basel–Boston–Berlin, 1992.

[18] A. Majda and R. Rosales. Resonantly interacting weakly nonlinear hyperbolic waves. I. A single space variable. *Stud. Appl. Math.*, 71:149–179, 1984.

[19] A. Majda, R. Rosales, and M. Schonbeck. A canonical system of integrodifferential equations arising in resonant nonlinear acoustics. *Stud. Appl. Math.*, 79:205–262, 1988.

[20] R. L. Pego. Some explicit resonating waves in weakly nonlinear Gas Dynamics. *Stud. Appl. Math.*, 79:263–270, 1988.

[21] W. H. Press, S. A. Teukolsky, W. T. Vetterling, and B. P. Flannery. *Numerical Recipes in Fortran, The Art of Scientific Computing.* Cambridge University Press, Cambridge, second edition, 1992.

[22] R. D. Richtmyer and K. W. Morton. *Difference Methods for Initial-value Problems.* Wiley-Interscience, 1967.

[23] G. Strang. On the construction and comparison of difference schemes. *SIAM J. Numer. Anal.*, 5:506, 1968.

[24] B. van Leer. Towards the ultimate conservative difference scheme IV. A new approach to numerical convection. *J. Comput. Phys.*, 23:276–299, 1977.

[25] B. van Leer. Towards the ultimate conservative difference scheme V. A second order sequel to godunov's method. *J. Comput. Phys.*, 32:101–136, 1979.

[26] D. Vaynblat. *The Strongly Attracting Character of Large Amplitude Nonlinear Resonant Acoustic Waves Without Shocks. A Numerical Study.* PhD dissertation, MIT, Department of Mathematics, August 1996.

[27] G. B. Whitham. *Linear and Nonlinear Waves.* Wiley, New York, 1974.